PEOPLE’S DEMOCRATIC REPUBLIC OF ALGERIA

MINISTRY OF HIGHER EDUCATION AND SCIENTIFIC RESEARCH

UNIVERSITY OF SAAD DAHLEB BLIDA **1**

INSTITUTE OF AERONAUTICS AND SPACE STUDIES

Department of Aeronautical Construction

END OF STUDIES' PROJECT

In view of obtaining the MASTER Diploma in Aeronautics

Option: Aircraft propulsion

AEROHEATING OPTIMISATION OF HYPERSONIC FLOW AROUND LIFTING BODIES DURING ATMOSPHERIC REENTRY WITH RADIATION EFFECT.

Made by :

ZEKRI Feriel

Led by :

Advisor ; ALLOUCHE Rachid

Co Advisor :RENANE Rachid

2023/2024

Acknowledgments

First and foremost, I would like to express my deepest gratitude to God, who has watched over me and guided me throughout these past five years. Without His blessings and grace, I would not be where I am today. His love have been my constant companions, and I am eternally grateful for His unwavering support.

I would also like to thank my family, whose love and encouragement have been invaluable. Their belief in me has been a source of motivation and strength. My parents, in particular, have been my rock, providing me with the support and guidance needed to persevere.

My deepest thanks go to my advisors, ALLOUCHE Rachid and Renane Rachid, for their guidance, patience, and insightful feedback throughout the research process. Their expertise and encouragement have been instrumental in the completion of this thesis.

Special thanks to my colleague and friend Remmal Asma , whose technical help and support have made this journey more enjoyable and less daunting. Her willingness to share her knowledge and experiences has been invaluable.

I would also like to thank my Friends Amine , Nejla , Raghda and Wafa , whose love and encouragement have been invaluable. Their belief in me has been a source of motivation and strength.

Dedication

This thesis is dedicated to my beloved parents, whose unwavering dedication and sacrifices have secured our education and success.

To my beloved mother, your endless love, patience, and encouragement have been the bedrock of my journey. Your faith in me has been a constant source of strength and motivation.

To my beloved father, your hard work and determination to provide for our future have been truly inspiring. Your support and guidance have been instrumental in my achievements.

I also dedicate this work to every person who has not had the chance to study. May this achievement inspire hope and possibility, and may it be a reminder that education is a fundamental right that should be accessible to all.

Table of contents

List of Figures

List of tables :

Nomenclature

β:	: apex angle
c_0	: local sound velocity
C_VD	: Vibration-dissociation coupling..
C_VDV	: Vibration-dissociation-vibration coupling.
C_p	: Mass heat at constant pressure (J.kg-1.K-1).
C_v	: Mass heat at constant volume (J.kg-1.K-1).
C_ps	: Constant pressure mass heat of the species (J.kg-1.K-1).
C_vs:	: Mass heat at constant volume of the species s(" " J.kg-1.K-1).
C_(v,s(rot):)	: Mass heat at constant volume of rotation of the species
C_(v,s(tr))	: Mass heat with constant volume of translation of (J.kg-1.K-1).
C_(v,s(v):)	: Mass heat at constant volume of vibration of .(J.kg-1.K-1)
D_a	: characteristic non-dimensional number of Damkölher
K	: Number of events the pmf q
l_0	: chord
L	: is a characteristic length of the obstacle
M	: Mach number
Mα	: the molar weight of the species α, respectively
θ^vib	: vibrational characteristic temperature
R_eL	: the Reynolds number
ρ	: is the density of the fluid
μ	: is its dynamic viscosity
τ_{vib}	: the relaxation time of the vibrational mode
τ_{ec}	: time required for a flow particle to move in the shock layer
τ_{ch}	: characteristic time for chemistry to occur

u_0 : the local flow velocit

γ: : sweep angle

E : total energy

e : wing thickness.

$\mathrm{Q} \sim \mathrm{Dir}(\alpha)$: random pmf Q coming from a Dirichlet distribution with parameter α.

q_{net} : : The net heat flux

q radiative transfers : The heat flux radiative net

$q$convec-diffus : The sum of the convective heat fluxes

$q_{\mathrm{convection}}$: The process of convection

$q_{\mathrm{diffusion}}$: : The process of diffusion

$\mathrm{R_a}$: the universal gas constant

$\mathrm{T^{tr}}$: translation temperature

$\mathrm{T^{(vib)}}$: the vibrational temperature

Abstract

This work focuses on simulating two-dimensional hypersonic, viscous, and turbulent airflow in a chemically non-equilibrium state. The simulation is based on the Navier-Stokes Equations using ANSYS Fluent 22. We specifically examine Lobb's sphere and Cone flare configurations. To ensure accurate results, we take into account the vibrational relaxation and dissociation of the air mixture at high temperatures, as well as radiation phenomena. Our main interest lies in simulating the flow behind the shock in the relaxation area, where intense thermochemical non-equilibrium phenomena occur. The Park chemical-kinetic model includes five species (N2, O2, NO, N, O) and a kinetic mechanism with five reactions. The results obtained are consistent with the scientific literature.

Keywords: Hypersonic flow, shock wave, dissociation, Euler equations, Navier-Stokes equations, Aeroheating , radiation.

Résume :

Ce travail se concentre sur la simulation de l'écoulement d'air hypersonique, visqueux et turbulent en état de non-équilibre chimique en deux dimensions. La simulation est basée sur les équations de Navier-Stokes en utilisant ANSYS Fluent 22. Nous examinons spécifiquement les configurations de la sphère de Lobb et du cône à jupe. Pour garantir des résultats précis, nous prenons en compte la relaxation vibrationnelle et la dissociation du mélange d'air à haute température, ainsi que les phénomènes de radiation. Notre principal intérêt réside dans la simulation de l'écoulement derrière le choc dans la zone de relaxation, où se produisent des phénomènes intenses de non-équilibre thermochimique. Le modèle chimico-cinétique de Park comprend cinq espèces (N2, O2, NO, N, O) et un mécanisme cinétique avec cinq réactions. Les résultats obtenus sont conformes à la littérature scientifique.

Mots-clés : Écoulement hypersonique, onde de choc, dissociation, équations d'Euler, équations de Navier-Stokes, chauffage aérothermique, radiation.

ملخّص

ويركز هذا العمل على محاكاة ثنائي الأبعاد الفائقة الفوقية، واللزجة، وتدفق الهواء المضطرب في حالة غير توازنية كيميائياً. وتستند المحاكاة إلى معادلات Navier-Stokes باستخدام ANSYS fluent 22. نحن على وجه التحديد نفحص مجال (لوب) و تشكيلات إنارة (كون) ولضمان تحقيق نتائج دقيقة، نأخذ في الاعتبار الاسترخاء الاهتزازي وانفصام الخليط الجوي في درجات الحرارة العالية، فضلا عن الظواهر الاشعاعية. ويكمن اهتمامنا الرئيسي في محاكاة التدفق وراء الصدمة في منطقة الاسترخاء، حيث تحدث ظواهر غير توازنية حرارية كيميائية شديدة. ويشمل النموذج الكيميائي - الحركي للمتنزه خمسة أنواع (N2, O2, NO, N, O) وآلية حركية ذات خمسة تفاعلات. وتتسق النتائج التي تم الحصول عليها مع المؤلفات العلمية.

الكلمات الرئيسية: معادلات الإيولر، الإنفصال، الموجة الصدمة، التدفق الشخصي، Navier-Stokes، التسخين الجوي، الإشعاع.

Introduction :

In recent years, significant effort has been dedicated to improving the understanding and modeling of thermochemical nonequilibrium processes in high-temperature shock layers. These shock layers form in front of vehicles traveling at hypersonic speeds through Earth and other planetary atmospheres.

As the vehicle decelerates due to atmospheric drag, the vehicle's kinetic energy is transferred to the gas. Initially, this occurs through an increase in translational temperature. The translational energy of the gas particles is then redistributed among other modes of energy accommodation, such as vibration, electronic excitation, dissociation, and ionization, through collisions. If the gas is sufficiently dense, collisions occur frequently enough for energy accommodation to quickly reach an equilibrium distribution among these modes. This equilibrium distribution can be characterized by two thermodynamic variables: temperature and pressure. In these equilibrium conditions, a relatively simple equation of state is used to relate pressure, temperature, and density. However, as the gas density decreases, the time between collisions increases, and the assumption of nearly instantaneous energy accommodation can no longer be made. In such cases, the state of the gas is not solely determined by local conditions, but is instead a result of processes occurring throughout its flow [1].

Nonequilibrium processes influence the design of a hypersonic entry vehicle in three ways. Aerodynamics are affected because surface pressure distributions in compressing or expanding flows are a function of the gas's heat capacity. Furthermore, the thickness of the laminar boundary layer, which influences the effectiveness of control surfaces, is dependent on gas chemistry. Examples of these aerodynamic effects are discussed in References [2] and [3].

Lastly, if the gas temperature is sufficiently high, radiant energy transfer becomes an important mechanism for both cooling the shock layer (photons escaping the shock layer) and heating the vehicle surface. Proper modeling of nonequilibrium radiation is particularly important in the design of a lunar aerobrake because the total heat load is near the limit of a reusable thermal protection system [1].

These benchmarks serve to de ne the convective and radiative heating levels using a baseline thermochemical kinetic model. They focus on stagnation point heating only, and do not encompass issues relating to integrated heat load or base heating. They are intended to complement conditions frequently used in the validation process for which experimental data are available but which are not necessarily representativeof most likely ight conditions. As kinetic models evolve, they can be tested at these benchmark conditions to assess their impact on vehicle aerothermodynamics.

This work is devided on four chapters, In the first chapter, we present a study on the phenomena of thermochemical non-equilibrium in the shock layer and the reduction of aerodynamic heating during atmospheric reentry. We also discuss the current state of the art in this field.
In the second chapter, we propose a mathematical and physical flow model for the reactive gas mixture in thermochemical non-equilibrium, considering the general case.

In the third chapter, we investigate the feasibility of using Ansys Fluent, a numerical computational code for fluid dynamics, to simulate this type of flow under reentry conditions, taking into account radiation effects.
The last chapter provides an overall presentation of our study results. Finally, we draw a general conclusion based on our findings.

Chapter 1

Atmospheric reentry characteristics and state of art

Chapter 1 :Atmospheric reentry characteristics and state of art

1.1 Atmospheric Reentry Characteristics:

The aging of the Space Shuttle prompted significant research on possible designs for its replacement through the years. For a long time it was believed that the replacement for this reusable vehicle would be a spacecraft more advanced, more efficient and of course, more reusable. One of the paradigms that received a lot of attention in the past years was air-breathing reusable vehicles. Such vehicles would take off from a runway and accelerate to orbital velocities using a series of different engines. The technology necessary for these spacecraft is still being developed and an operational vehicle is still many years away . [5]

Returning from space, astronauts face a similar challenge. Earth's atmosphere presents to them a dense, fluid medium, which, at orbital velocities, is not all that different from a lake's surface.

They must plan to hit the atmosphere at the precise angle and speed for a safe landing. If they hit too steeply or too fast, they risk making a big "splash," which would mean a fiery end.

If their impact is too shallow, they may literally skip off the atmosphere and back into the cold of space. This subtle dance between fire and ice is the science of atmospheric re-entry.

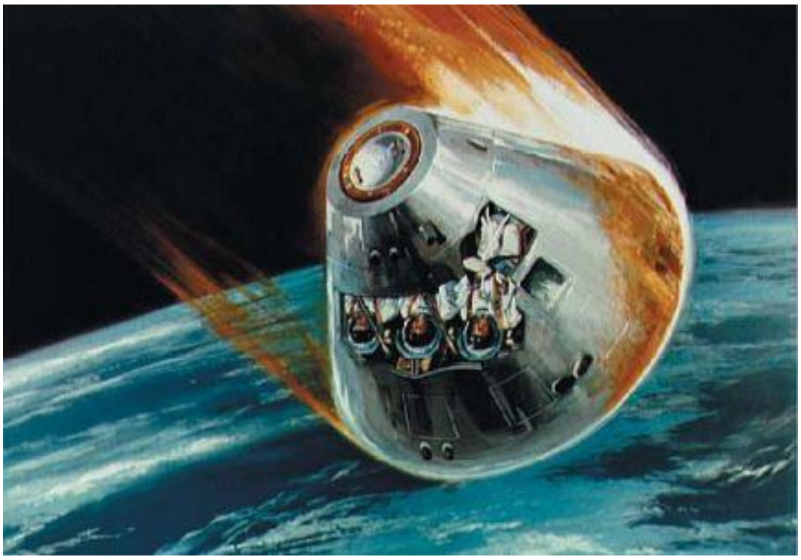

Figure 1.1 : Apollo Capsule Re-entry. This artist's concept of the Apollo re-entry shows that air friction causes the capsule to glow red hot. The astronauts inside stay cool, thanks to the protective heat shield (Courtesy of NASA/Johnson Space Center)

Reentry has been achieved with speeds ranging from 7.8 km/s for low Earth orbit to around 12.5 km/s for the Stardust probe. [9] Crewed space vehicles must be slowed to subsonic speeds before parachutes or air brakes may be deployed. Such vehicles have high kinetic energies, and atmospheric dissipation is the only way of expending this, as it is highly impractical to use retrorockets for the entire reentry procedure.

While NASA's Earth entry interface is at 400,000 feet (122 km), the main heating during controlled entry takes place at altitudes of 65 to 35 kilometres (213,000 to 115,000 ft), peaking at 58 kilometres (190,000 ft). [10]

Adding to that objects entering an atmosphere experience atmospheric drag, which puts mechanical stress on the object, and aerodynamic heating—caused mostly by compression of the air in front of the object.

In the context of the Earth's atmosphere, the plasma formed is the site of complex chemistry involving a large number of atomic, molecular, radical, and ionized species (N_2, O_2, NO, N, O, N_2^+, O_2^+, etc.) in their ground electronic state or in a multitude of excited states [4].. The presence of this highly energetic plasma around the spacecraft causes significant heating of the vehicle's surface, with the heat flux typically being several hundred kW/m^2.

1.2 Flow characteristics :

1.2.1 Velocity Regimes during Atmospheric Reentry:

Atmospheric reentry involves a transition from space velocities to atmospheric velocities. There are three primary velocity regimes that vehicles experience during this phase: suborbital, orbital, and hypersonic. Each regime has its unique characteristics, and they can be described by their respective velocity ranges.

1.2.2 Dynamic behaviour :

Suborbital Regime :

Velocity Range: The suborbital regime covers velocities below orbital speed, typically ranging from 0 to 7.8 km/s (0 to Mach 23.6 at sea level). Which characterised by the following equation :

$$KE=\frac{1}{2}mv^2 \tag{1.1}$$

where:

- *KE* is the kinetic energy,
- *m* is the mass of the object,
- *v* is the velocity.

In the suborbital regime, vehicles are moving at high speeds but are not yet in orbit. This regime is associated with space tourism, suborbital spaceflights, and the initial stages of spacecraft reentry.

Orbital Regime:

The orbital regime encompasses velocities required to achieve and maintain stable orbits around Earth. This typically starts at approximately 7.8 km/s (Mach 23.6 at sea level) and extends to orbital velocities, which are roughly 28,000 km/h (about 7.8 km/s) for low Earth orbit (LEO). Which characterised by the following equation :

$$Vorb=\sqrt{\frac{GM}{R}} \tag{1.2}$$

- Vorb is the orbital velocity,
- G is the gravitational constant,
- M is the mass of Earth,
- R is the radius of the orbit.

Hypersonic Regime:

The hypersonic regime starts above orbital velocity (around 7.8 km/s) and extends to speeds greater than Mach 5 (approximately 1.7 km/s or 6,120 km/h) in the lower thermosphere Which characterised by the following equation :

$$M = \frac{v}{a} \tag{1.3}$$

where:

- M is the Mach number,
- v is the velocity,
- a is the speed of sound.

In the hypersonic regime, vehicles experience high-speed flight through the upper atmosphere, often characterized by intense aeroheating due to compression and heating of the air ahead of the vehicle. Hypersonic vehicles and reentry capsules enter this regime during the descent phase.

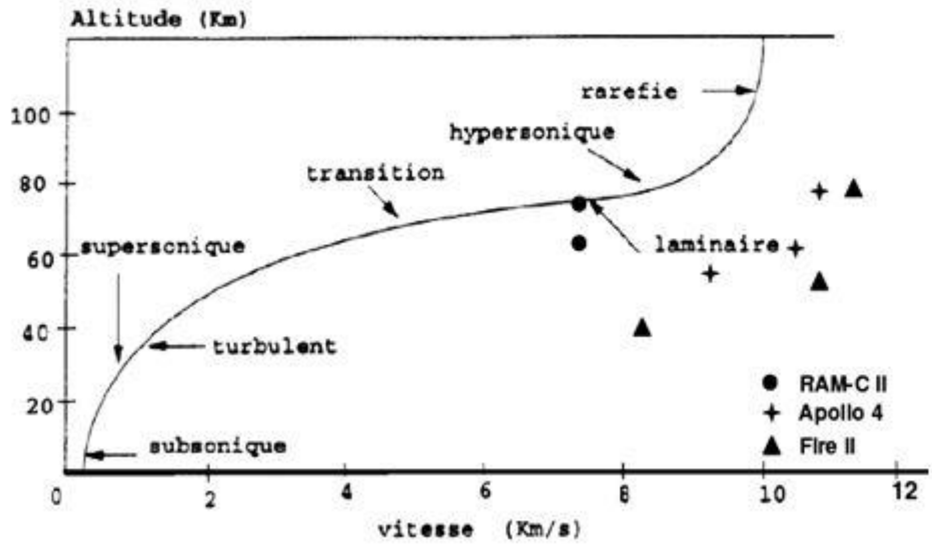

Figure1.2 Flow regime as a function of altitude and speed for typical conditions of lunar reentry [5

1.2.3 Dynamic Behavior and Reynolds Number (Re):

The value of the Reynolds number (Re) classifies fluid flows into different regimes, each with its distinct dynamic behavior. These regimes are often used to describe the behavior of flows around objects, including aircraft, ships, and vehicles during atmospheric reentry.

There are Three major regimes exist: [6]

$$Re = \frac{\rho v L}{\mu} \tag{1.4}$$

1. Laminar Flow (Re < 2000):

2. Transition Flow (2000 < Re < 4000):

3. Turbulent Flow (Re > 4000):

- Turbulent flow is common in high-speed and high Reynolds number scenarios. It can lead to increased heat transfer, drag, and mixing, which are important considerations in atmospheric reentry.

let's elaborate on the concept of flow regimes and how they are described using the Knudsen number (Kn) in the context of atmospheric reentry for hypersonic vehicles.

1.2.4 Flow Regimes and the Knudsen Number (Kn) :

Flow regimes refer to the different states or behaviors that a gas or fluid can exhibit under varying conditions, particularly when it comes to hypersonic vehicles during atmospheric reentry. The density of the Earth's atmosphere varies significantly with altitude, and this variation leads to diverse flow regimes along the vehicle's flight trajectory. These flow regimes can be characterized using the Knudsen number (Kn), which provides insights into the relative importance of molecular collisions to continuum behavior.

The Knudsen Number (Kn):

The Knudsen number (Kn) is a dimensionless parameter used to quantify the degree of non-equilibrium in a gas flow. It is defined as the ratio of the mean free path of gas molecules to a characteristic length: [6]

$$kn = \frac{\lambda}{L} \tag{1.5}$$

The mean free path λ is the average distance a gas molecule travels between collisions with other molecules. When λ is much smaller than \(L \), the flow is in the continuum regime, where fluid properties can be described using the Navier-Stokes equations. When λ becomes comparable to or larger than λ, the flow enters the rarefied regime, where molecular interactions play a significant role.

1.2.5 Flow Regimes and Altitude Variations:

As a hypersonic vehicle travels through the Earth's atmosphere during reentry, its altitude changes, leading to variations in atmospheric density. Consequently, the Knudsen number changes along the vehicle's trajectory. Here's how different flow regimes correspond to different Knudsen number ranges:

1. Continuum Regime (Kn << 1):

- In the continuum regime, the Knudsen number is much smaller than 1 Kn <1
- This regime is characterized by a dense gas where fluid dynamics and the Navier-Stokes equations can be applied. Molecular collisions dominate, and the flow behaves like a continuous fluid.

- It is typically encountered at lower altitudes during reentry when the atmospheric density is high.

2. Transitional Regime (0.1 < Kn < 10):

- The transitional regime occurs when the Knudsen number is between 0.1 and 10 (0.1 < Kn < 10).
- In this regime, both molecular collisions and continuum behavior are significant. The flow may exhibit characteristics of both rarefied and continuum flow.
- Transition models are often used to simulate this regime, and it is relevant during the transition from rarefied to continuum flow.

3.Rarefied Regime (Kn >> 1):

- The rarefied regime occurs when the Knudsen number is much larger than 1 .
- In this regime, molecular collisions are infrequent, and the flow behaves as a collection of individual gas molecules. The Boltzmann equation and kinetic theory are used to model the flow.
- It is significant at higher altitudes during reentry when the atmospheric density is low.

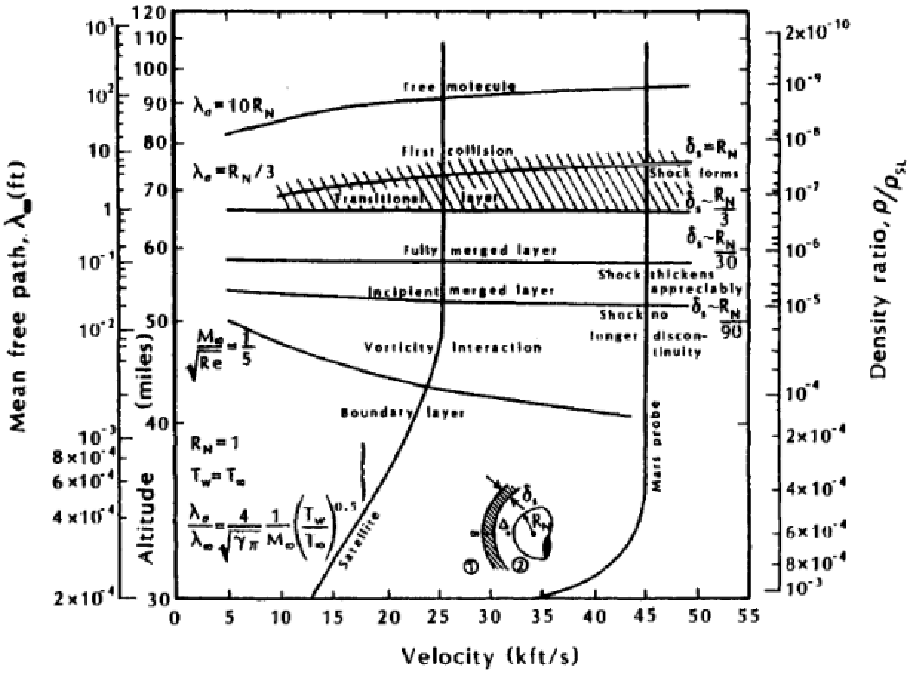

Figure 1.3: Presentation of the different flow regimes encountered depending on the altitude[7]

1.2.4 Hypersonic Regime Dynamics at High Temperatures:

The dynamics of gases at high temperatures in the continuous hypersonic regime play a pivotal role in the challenging and thrilling field of aerospace engineering, particularly during atmospheric reentry. To appreciate this phenomenon, it's essential to delve into the intricate interplay of factors that come into play.

- Hypersonic flight is characterized by speeds exceeding five times the speed of sound (Mach 5 or higher). These tremendous velocities expose the vehicle to extreme conditions, including very high temperatures .At such speeds, the compression of air ahead of the vehicle generates intense aerodynamic heating, resulting in temperatures that can soar well beyond 2,000 degrees Celsius (3,600 degrees Fahrenheit).
- The continuous hypersonic regime, often called the continuum regime, is the domain where the behavior of the gas closely resembles that of a traditional fluid. In this regime, fluid dynamics theories, such as the Navier-Stokes equations, can be applied. However, high temperatures introduce complexities. Gas molecules gain significant kinetic energy,

leading to increased collision rates and changes in chemical reactions. As a result, the gas deviates from ideal behavior.

- Non-equilibrium effects become pronounced at high temperatures in hypersonic flight. This means that the gas is not in a state of thermodynamic equilibrium, and chemical reactions play a more prominent role..As the gas molecules collide, they can dissociate, ionize, and recombine. These non-equilibrium reactions release energy and contribute to the intense heating experienced by the vehicle.

1.2.4.1 Normal shocks :

The shock wave is thought to represent a surface of discontinuity perpendicular to the flow, dividing an upstream region 1 from a downstream region 2 in the configuration we're looking at. This shock wave is stationary. As a result, by applying balance equations to these discontinuities, we’ll be able to relate the properties of the flow upstream and downstream of the shock wave, and hence the values that characterize these two zones.

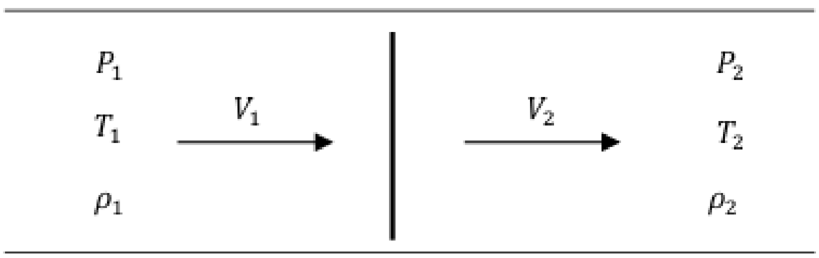

Figure 1.4 A normal shock wave configuration for the balance sheet. [8]

$$\dot{m}v_2 - \dot{m}v_2 = p_1A_1 - p_2A_2 \tag{1.6}$$

We assume that the flow rate remains constant and that the only source of variation in moment pressure forces. Because (A1 = A2) and (2.5) are used, we can conclude:

$$p_1 + \rho_1 v_1^2 = p_2 + \rho_2 v_2^2 \tag{1.7}$$

The energy balance is simply written in the absence of effort and heat input:

$$h_1 + \frac{u_1^2}{2} = h_2 + \frac{u_2^2}{2} \tag{1.8}$$

introducing the state equation to these equations, we obtain four equations, allowing, fr e knowledge of the state (1), to calculate the four unknowns, p_2, ρ_2, v_2, h_2 which character he state (2). Mass balance: [8]

$$\rho_1 v_1 = \rho_2 v_2 \tag{1.9}$$

- **Momentum balance:**

$$p_1 + \rho_1 v_1^2 = p_2 + \rho_2 v_2^2 \tag{1.10}$$

- **Energy balance:**

$$h_1 + \frac{u_1^2}{2} = h_2 + \frac{u_2^2}{2} \tag{1.11}$$

- **Equation of state (several possible shapes):**

$$\rho = \rho(s, p) \tag{1.12}$$

1.2.4.2 Normal shock wave for a perfect gas:

We know that the equation of state of the gas is fairly simple in this situation, example, in the form:

$$p = \rho r T \tag{1.13}$$

Because the shock is infinitely thin perpendicular to the flow, the section remains constant (A1=A2). One acquires momentum as a result of this.

The equations for the balances are then simplified to obtain:
Mass balance:

$$\rho_1 v_1 = \rho_2 v_2 \tag{1.14}$$

Momentum balance sheet:

$$p_1 + \rho_1 v_1^2 = p_2 + \rho_2 v_2^2 \tag{1.15}$$

Energy balance:

$$C_pT_1 + \frac{v_1^2}{2} = C_pT_2 + \frac{v_2^2}{2} \quad (1.16)$$

Energy balance:

To achieve simple ratios, we will now try to display the upstream and downstream Mach numbers. As a result, we have for the energy equation:

$$C_pT_1 + \frac{v_1^2}{2} = C_pT_1\left(1 + \frac{v_1^2}{2C_pT_1}\right) = C_pT_1\left(1 + \frac{\gamma - 1}{2}M_1^2\right) \quad (1.18)$$

Since $c_1{}^2 = \gamma r T$ The energy balance equation is as follows: $C_p = \frac{\gamma r}{\gamma - 1}$

$$\frac{T_2}{T_1} = \frac{1 + \frac{\gamma - 1}{2}M_1^2}{1 + \frac{\gamma - 1}{2}M_2^2} \quad (1.19)$$

The equation for momentum balance can now be transformed using:

$$p_1 + \rho_1 v_1^2 = p_1\left(1 + \frac{\rho_1 v_1^2}{p_1}\right) = p(1 + \gamma M_1^2) \quad (1.20)$$

Using $c_1^2 = \frac{\gamma \mathrm{P}}{\rho}$ So here's the second relation we're looking for:

$$\frac{p_2}{p_1} = \frac{1 + \gamma M_1^2}{1 + \gamma M_2^2} \quad (1.21)$$

The evolution of the ratio can be quickly deduced using the equation of state of ideal gases: ρ_2/ρ_1

The upstream and downstream Mach numbers must now be connected. The mass balance is employed in this process:

$$\frac{\rho_2}{\rho_1} = \frac{v_1}{v_2} = \frac{M_1 c_1}{M_2 c_2} \quad (1.22)$$

The first and third members of this equality can be transformed by employing:

$$\rho = \frac{p}{rT}\ c = (\gamma \mathrm{rT})^{\frac{1}{2}} \tag{1.23}$$

To get:

$$\frac{p_2}{p_1} = \frac{M_1}{M_2}\left(\frac{T_2}{T_1}\right)^{1/2} \tag{1.24}$$

Changes in Mach numbers have previously been linked to pressure and temperature ratios. We may establish the following relationship between the upstream and downstream Mach numbers by simple substitution:

$$M_2^2 = \frac{2 + (\gamma - 1)M_1^2}{2M^2} \tag{1.25}$$

The equation 1.25, when combined with the formulas previously discovered for the pressure, temperature, and density ratios, now gives the value of these ratios as a function of the number of upstream Mach numbers (for example). As a result, we have:

$$\frac{T_2}{T_1} = \left(\frac{2\gamma}{\gamma + 1}M_1^2 - \frac{\gamma - 1}{\gamma + 1}\right)\left(\frac{\gamma - 1}{\gamma + 1} + \frac{2}{(\gamma + 1)M_1^2}\right) \tag{1.26}$$

Similarly, we discover:

$$\frac{p_2}{p_1} = \frac{2\gamma}{\gamma + 1}M_1^2 - \frac{\gamma - 1}{\gamma + 1} \tag{1.27}$$

Finally, using the state equation:

$$\frac{\rho_2}{\rho_1} = \frac{\rho_2}{P_1}\frac{T_1}{T_2} = \frac{2 + (\gamma - 1)M_1^2}{1 + (\gamma - 1)M_1^2} \tag{1.28}$$

Like $\rho_1 v_1 = \rho_2 v_2$ Finally, using the state equation:

$$\frac{v_1}{v_2} = \frac{2 + (\gamma - 1)M_1^2}{1 + (\gamma - 1)M_1^2} \tag{1.29}$$

1.2.4.3 Shock wave in hypersonic flow:

The formulae for pressure, density, and temperature following the shock wave reach a mathematical limit when the Mach number of the upstream flow grows progressively hypersonic. [9]

Oblique shock wave equations:

$$\frac{\rho_2}{\rho_1} \approx \frac{\gamma + 1}{\gamma - 1} \tag{1.30}$$

The hypersonic limit for the density ratio is 6 for a perfect atmospheric gas approximation using = 1.4. Hypersonic post-shock dissociation of O2 and N2 into O and N, on the other hand, lowers, permitting larger density ratios in nature. The temperature ratio of hypersonic is:

$$\frac{T_2}{T_1} = \frac{2\gamma(\gamma - 1)}{(\gamma + 1)^2} M_1^2 \sin^2 \beta \tag{1.31}$$

Normal shock wave equations

$$\frac{T_2}{T_1} = \left(\frac{2\gamma}{\gamma + 1} M_1^2\right) \tag{1.32}$$

$$\frac{V_2}{V_1} = \frac{\gamma + 1}{\gamma - 1} \tag{1.33}$$

However, the state equation h = cpT, which was proposed to complete this system, is insufficient to capture the effects of genuine gases arriving at high temperatures. This equation of state is a simplified version of the relations, which is derived from the assumption cp = constant: [9]

$$h(T) = h(T_0) + \int_{T_0}^{T} c_{p(\tau)d\tau} \tag{1.34}$$

It is impossible to view cp as a constant at high temperatures due to the gradual stimulation of interior levels of molecules. It is no longer possible to solve the Rankine-Huguenot equations analytically when a realistic equation of state is taken into consideration, which becomes a nonlinear function of temperature.

1.2.4.2 Oblique Shocks:

Oblique shocks occur when a shock wave is inclined at an angle to the incoming flow. Understanding the dynamics of oblique shocks is crucial for predicting and controlling the aerodynamic forces experienced by objects traveling at hypersonic speeds.

1.2.4.3 Oblique shock wave geometry and analysis :

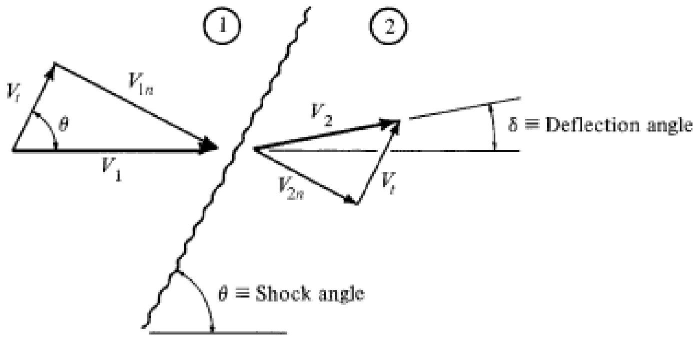

Figure 1.5 : Oblique shock wave geometry [6]

The state equation of gas is simply expressed as following :

- **Continuity :**

$$\rho_1 Vn_1 = \rho_2 Vn_2 \tag{1.35}$$

lines forming part of the control surface are exact duplicates of each other, we may write ;

- **Momentum in t-direction :**

$$(\rho_1 Vn_1)Vt_1 = (\rho_2 Vn_2)Vt_2 \tag{1.36}$$

$$Vt_2 = Vt_1 = Vt \tag{1.37}$$

- **Momentum in n-direction :**

$$P1 - P2 = \rho_2 {Vn_2}^2 - \rho_1 {Vn_1}^2 \tag{1.38}$$

- **Energy :**

$$Cp(T1 - T2) = \frac{{V_2}^2 - {V_1}^2}{2} \tag{1.39}$$

1.2.4.4 Oblique shocks relations :

$$M_{n1} \equiv \frac{u_1}{a_1} = V1\, sin \frac{\beta}{a_1} = M_1\, sin\, \beta \tag{1.40}$$

$$M_{n2} \equiv \frac{u_2}{a_2} = V1\, sin \frac{(\beta - \theta)}{a_2} = M_2 \sin(\beta - \theta) \tag{1.41}$$

This allows us to create the well-known equations that correspond to all of the changes that occur across a shock wave. These are the relations :

$$\frac{\rho 2}{\rho 1} = \frac{(\gamma + 1){M_{n1}}^2}{2 + (\gamma - 1){M_{n1}}^2} \tag{1.42}$$

$$\frac{P2}{P1} = 1 + \frac{2k}{k + 1}\left({M_{n1}}^2 - 1\right) \tag{1.43}$$

$$\frac{u2}{u1} = \frac{2 + (\gamma - 1){M_{n1}}^2}{(\gamma + 1){M_{n1}}^2} \tag{1.44}$$

$${M_{n2}}^2 = \frac{{M_{n1}}^2 + 2/(\gamma - 1)}{(\frac{2k}{(\gamma + 1)}){M_{n1}}^2 - 1} \tag{1.45}$$

If we replace the $Mn1$ equation in the normal shock relation we get the flowing oblique shock equations :

Oblique shock wave equations ;

$$\frac{T2}{T1} = \left(\frac{2\gamma}{\gamma + 1}M_1^2 \sin^2\ \beta - \frac{\gamma - 1}{\gamma + 1}\right)\left(\frac{\gamma - 1}{\gamma + 1} + \frac{2}{(\gamma + 1)M_1^2 \sin^2\ \beta}\right) \tag{1.46}$$

$$\frac{P2}{P1} = \frac{2\gamma}{\gamma + 1}M_1^2 \sin^2 \beta - \frac{\gamma - 1}{\gamma + 1} \tag{1.47}$$

$$\frac{\rho 2}{\rho 1} = \frac{(\gamma + 1)M_1^2 \sin^2\ \beta}{2 + (\gamma - 1)M_1^2 \sin^2\ \beta} \tag{1.48}$$

$$\frac{P2}{P1} \approx \frac{2\gamma}{\gamma + 1}M_1^2 \sin^2 \beta \tag{1.49}$$

As a result of these equations, we can deduce that the fluctuation of thermodynamic parameters caused by oblique shock is dependent on two variables: the Mach number upstream of the shock wave M_1 and the shock angle.

$$\mathrm{M}_{\mathrm{n2}}^2 = \frac{1 + \frac{\gamma - 1}{2}\mathrm{M}_{\mathrm{n1}}^2}{\gamma \mathrm{M}_{\mathrm{n1}}^2 - \frac{\gamma - 1}{2}} \tag{1.50}$$

$$M_2 = \frac{M_{\mathrm{n2}}}{\sin\,(\beta - \theta)} \tag{1.51}$$

The $\boldsymbol{\theta-\beta-}$M relation:

The wave angle β is still required for these relations. a relationships can be found from the geometry [6] :

$$\frac{\tan(\beta-\theta)}{\tan\beta}=\frac{u_2}{u_1}=\frac{\rho_1}{\rho_2}=\frac{(\gamma+1)M_1^2\sin^2\beta}{2+(\gamma-1)M_1^2\sin^2\beta} \tag{1.52}$$

The last relation we'll employ is the one that calculates the entropy change across the shock wave. To accomplish this, we write:

$$\frac{S_2-S_1}{C_v}=\ln\left(\frac{1}{\gamma+1}\right)^{\gamma+1}(2\gamma M_1^2\sin^2\beta-\gamma+1)\left(\frac{2}{M_1^2\sin^2\beta}+\gamma-1\right)^{\gamma} \tag{1.53}$$

1.2.4.5 The Rankine-Hugoniot Equations :

Let us eliminate all velocity terms from the basic equations and arrive at a relation in terms of pressure and densities.

$$\frac{P2}{P1}=\frac{\frac{k+1}{k-1}\frac{\rho_1}{\rho_2}-1}{\frac{k+1}{k-1}-\frac{\rho_1}{\rho_2}} \tag{1.54}$$

$$\frac{\rho_1}{\rho_2}=\frac{\frac{k+1}{k-1}\frac{P2}{P1}+1}{\frac{k+1}{k-1}+\frac{P2}{P1}} \tag{1.55}$$

The Rankine-Hugoniot relations, depicted in the figure, indicate that the density ratio across a shock depends solely on the pressure ratio, influenced by the initial Mach number and shock angle. These relations apply to both normal and oblique shocks of any angle. This consistency arises because coordinate transformations converting normal shocks to oblique shocks do not alter the pressure and density change relations. According to the perfect gas laws, there is a unique relationship between the temperature ratio and pressure ratio, as well as between the temperature ratio and density ratio, across shocks of any obliquity.

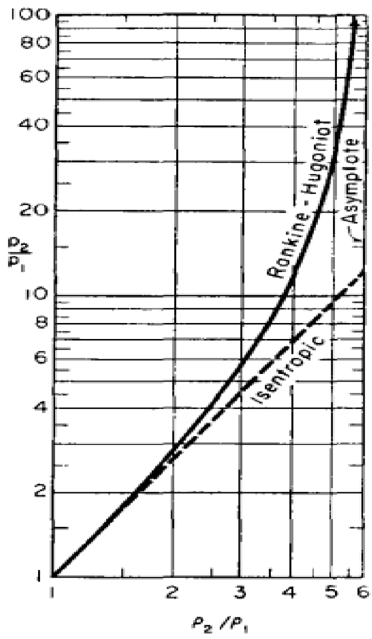

Fig 1.6 : Rankine-Hugoniot relation compared with isentropic law, for k=1,4

[34]

1.2.4.6 Detached Shocks :

The various graphical representations of Fig. 1.6 and 1.8 show that for a specified initial Mach number, Mi, there is a maximum value of the turning angle, 5max, for which an oblique shock solution exists. Conversely, for a specified turning angle, 5, there is a minimum initial Mach Number, Mi, min, for which an oblique shock solution exists. [34]

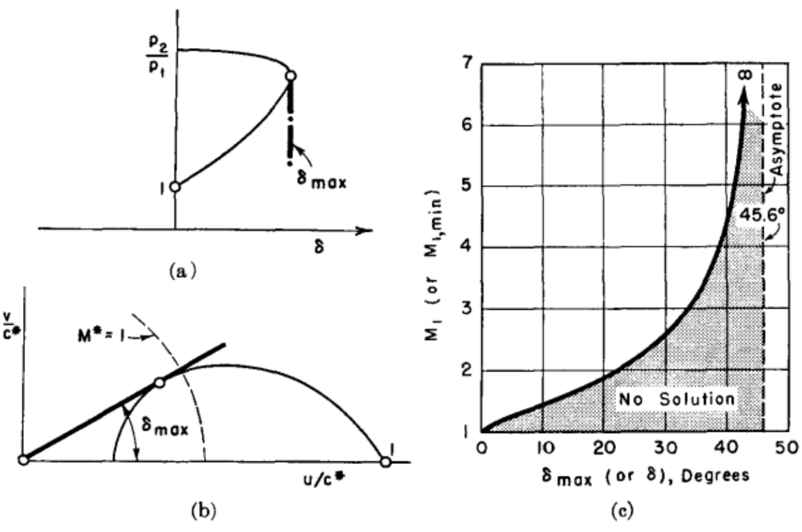

Fig. 1.7. Maximum turning angle for a given initial Mach Number.

(a) Pressure-deflection shock polar.
(b) Hodograph shock polar.
(c) Chart for k = 1.4.

When the shock is detached , it is invariably curved if the body of Fig. 1.8 represents the leading edge of the wing of a supersonic aircraft, we can see intuitively that the curved shock which begins at A.

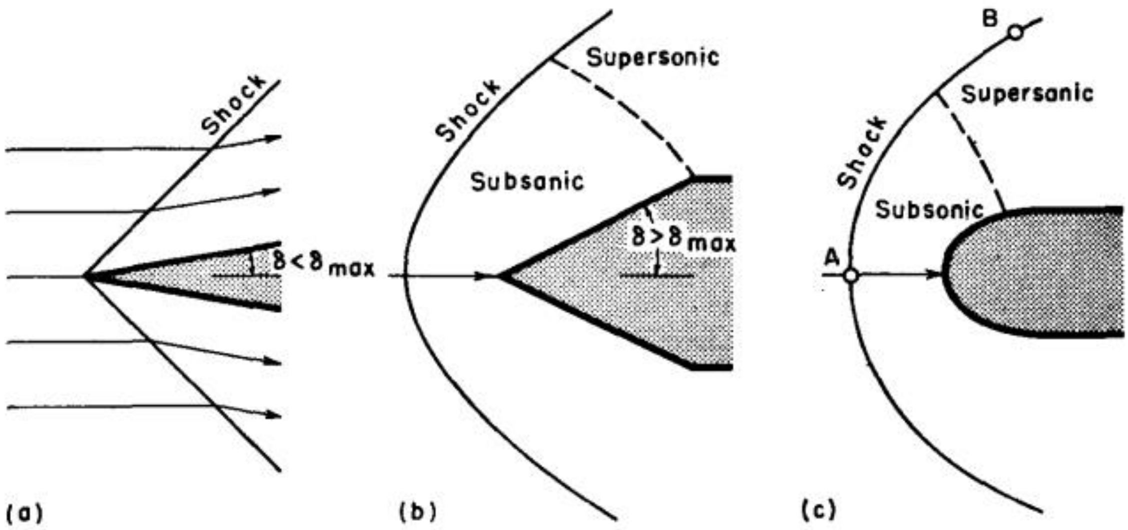

Fig 1.8 : detached and attached shocks [34]

(a) Attached shock on wedge of a small angle
(b) Detached shock on wedge of large angle
(c) Detached shock in front of blunt body

1.2.4.7 Physicochemical phenomena in the shock layer:

The hypersonic flow regime is characterized by the increasing importance of physical phenomena as the Mach number rises. One such phenomenon is the presence of strong shock waves near the body's surface in external flows, resulting in high temperature and density jumps over the shock wave. The small flow region between the bow shock and the surface is called the shock layer. As Mach numbers increase, the shock angle decreases, reducing the shock layer's size. The boundary layer thickness on hypersonic vehicles can be large relative to the shock layer, potentially merging with the bow shock. This strong interaction, known as hypersonic viscous interaction, requires a fully viscous modeling approach [2].

As the free stream Mach number increases from supersonic values, the temperature behind the bow shock wave becomes high enough to excite molecular internal energy modes and cause dissociation of diatomic gas molecules. At higher Mach numbers, ionization of species occurs, and the gas may emit or absorb radiation. These high-temperature effects cause deviations from perfect gas properties. Rarefaction phenomena, such as velocity and temperature slip at the body wall, are also significant in hypersonic flows. At low temperatures (800 K), gases can be modeled as calorically perfect with constant specific heats. Above 800 K, vibrational excitation causes specific heats to vary with temperature, making the gas thermally perfect.

Chemical reactions occur at even higher temperatures, turning air into a chemically reacting mixture of thermally perfect gases. For an equilibrium chemically reacting gas, properties depend on both temperature and pressure. At 1 atm pressure, dissociation begins around 2000 K, with molecular oxygen fully dissociating at 4000 K and nitrogen at 9000 K. Above 9000 K, ionization forms a partially ionized plasma. These high-temperature effects initiate through molecular collisions, with characteristic times for equilibrium processes. Hypersonic flows can experience chemical and thermal nonequilibrium due to high velocities and low densities, where equilibrium states lag local conditions. During space vehicle reentry, these phenomena challenge gas dynamic modeling, with vehicles encountering a wide range of Mach, Knudsen, and Reynolds numbers, transitioning through subsonic to hypersonic, continuum to free molecular, and laminar to turbulent regimes, with varying Damköhler numbers influencing flow behaviors.

1.3 Modelling the heat flow to the wall:

1.3.1 Convection at the Stagnation Point :

For high-speed re-entry conditions, the Stanton number at the stagnation point can be estimated using approximations developed in the late 1950s by Lees and Allen, and Eggers. These approximations are based on empirical and theoretical analyses of hypersonic flow heat transfer processes. the Stanton number can be calculated as follows: [35]:

$$St_{HIGH\ SPEED} = \frac{h}{\rho_\infty\ cp\ v_\infty} \tag{1.83}$$

where:

- H : convection coefficient $w/(m2k)$
- cp: specific heat at constant pressure in $j/(Kg.\ k)$
- $V\infty$: speed of the upstream infinite flow in meters

$$\mathrm{Re} = \frac{\rho u R}{\mu} \tag{1.84}$$

Once the Stanton number is known, the heat flux at the stagnation point can be estimated using the relationship:

$$q = \rho c_p u(T_\infty - T_w)\ St \tag{1.84}$$

Wall Temperature (T_w) :

Rearranging the heat flux equation, the wall temperature can be solved as:

$$T_w = T_\infty - \frac{q}{\rho c_p u St} \tag{1.86}$$

Chapter 2

Mathematic Modelisation

2.1 introduction :

Basic nonlinear equations, such as the Navier-Stokes equations, are essential for theoretical research in aeroheating optimization of hypersonic flow around lifting bodies during atmospheric reentry with radiation effects. Numerical methods are crucial for studying these equations, especially in the highly complex flow regime encountered during reentry. The intense turbulence generated by the high-speed flow and shock waves ensures effective heat transfer and aerodynamic performance. Thus, understanding turbulent flow properties and managing turbulence in computational fluid dynamics (CFD) is critical for optimizing aeroheating and ensuring the thermal protection of the reentry vehicle.

2.2 Governing equations :

2.2.1 Species conservation:

For species in a mixture, the mass conservation equation is dictated by:

$$\underbrace{\frac{\partial \rho_\alpha}{\partial t}}_{1} + \underbrace{\frac{\partial}{\partial x}\left(\rho_\alpha u - (-q^D_{\alpha x})\right)}_{2} + \underbrace{\frac{\partial}{\partial y}\left(\rho_\alpha u - \left(-q^D_{\alpha y}\right)\right)}_{3} = \underbrace{\dot{\mathbf{w}}_\alpha}_{4} \tag{2.1}$$

In the above equation, [10]

- The term (1) represents the rate of change of mass of species α per unit volume in a cell centered at point (x, y) • In term (2)
- The second term : $\rho_a u$ qui représente la composante-x du flux de masse de convection des especes α à travers les parois cellulaires et q^D_α, qui représente la composante-x du flux de diffusion des espèces α à travers parois cellulaires.
- $\rho_a u$ represents the x- component of flux of mass of species α, convected across cell walls
- Term (3) has the same meaning as term (2) but in the y- direction •
- Term (4) represents the mass production rate of species α due to chemical reactions.
-

  $\sum_{a=1}^{N_s} \bar{w}_a$ is zero, since mass is conserved in chemical changes.

Cette équation définit le taux de production de l'espèce chimique α dû aux réactions chimiques dans l'écoulement. Lorsqu'un fluide est en mouvement, il se déplace à une vitesse moyenne $\vec{\mathrm{v}}$. Pour un mélange d'espéces différentes, chaque espéce α a elle-même sa propre vitesse moyenne $\widehat{\mathrm{v}_{\mathrm{a}}}$.

2.3.2 Globale continuity equation :

Summing the Ns individual species mass conservation equations yield the total mass conservation for the mixture as a whole. The global continuity equation looks like this [10].

$$\frac{\frac{d\rho}{g}}{1} + \frac{\frac{b}{\alpha x}(\rho u)}{2} + \frac{\frac{d}{sy}(\rho u)}{3} = 0 \tag{2.5}$$

In the above equation, [10]

- Term (1) is the rate of change of mass of the mixture per unit volume in a cell centered at (x, y).
- Terms (2) and (3) are x and y components of the mass flux.

2.3.4 Conservation of Vibrational Energy

The equation of conservation of vibrational energy is given by: [12]:

$$\underbrace{\frac{\partial}{\partial t}\left(\rho_m e_m^{vib}\right)}_{1} + \underbrace{\frac{\partial}{\partial x}\left(\rho_m e_m^{vib} u - q_{mx}^{vib}\right)}_{2} + \underbrace{\frac{\partial}{\partial y}\left(\rho_m e_m^{vib} v - q_{my}^{vib}\right)}_{3} = \underbrace{\Omega_m}_{4} \tag{2.6}$$

In the above equation,

- The term (1) denotes the rate of change of vibrational energy of the molecule m. per unit volume in a cell centered at (x, y)
- In term (2), $\rho_n e_n^{pib} w$ is the x component of the vibrational energy flux that passes through cell walls

- The term q_{mx}^{vib} consists of two parts:
  - ✓ The conduction of vibrational energy across cell walls caused by vibrational temperature gradients in the x direction is the first part.

- ✓ The diffusion of vibrational energy across cell walls due to molecule concentration gradients in the x direction is the second term.

- Term (3) is the same as term (2), but in the y direction
- Term (4) represents the source term resulting of various energy exchange processes and is expressed as :

$$a_m = \Omega_{VD} + \Omega_{VT} + \Omega_{VV} \tag{2.7}$$

Where :

- $\Omega_{VD}$is the vibrational energy lost or gained due to molecular depletion (dissociation) or production (recombination) in the cell.
- $\Omega_{VT}T$ is the energy exchange between vibrational and translational modes due to collisions within the cell .
  Ω_{vy} is the energy exchange between vibrational modes of molecule with different m molecules.

Total energy conservation:

- Total energy conservation (internal + kinetic) is regulated by

$$\underbrace{\frac{\partial(\rho E)}{\partial t}}_{1} + \underbrace{\frac{\partial}{\partial x}(\rho E + p)u - \left(u\tau_{xx} + v\tau_{\gamma x} + qt_x\right)}_{2} + \underbrace{\frac{\partial}{\partial y}\left((\rho E + p)v - \left(u\tau_{xx} + v\tau_{\gamma x} + q_\gamma t\right)\right)}_{3} \tag{2.8}$$

- In the above equation: [10]

- The term (1) in a cell cantered is the rate of change in total energy per unit of volume (x, y).

- In the term (2):
  o $(\rho \mathrm{E} + \mathrm{p})$ is the component of the total enthalpy flow convicted through the cell walls
  o $u\tau_{xx} + v\tau_{\gamma x}$ is the work carried out by shear forces

- qt consists of two parts:
  ✓The first is the conduction of thermic energy through the walls of cells due to temperature gradients in the x direction.
  ✓The diffusion of enthalpy through cell walls is the second term
- Term (3) has the same meaning as term (2), but in the other direction.

2.3 Thermochemical modelling:

2.3.1. Mixture properties:

Summing all of the partial densities and partial pressures of all species yields the mixture density and mixture pressure:

$$\rho = \sum \rho\alpha \tag{2.9}$$

$$P = \rho R_u T^{(Tr)} \sum X_\alpha / M_\alpha \tag{2.10}$$

where

- $X_\alpha = \rho_\alpha / \rho$ is the mass fraction
- M_α is the molar weight of the species α
- R_u is the universal gas constant
- T^{tr} is the translation temperature.

Translational and rotational modes are given the same temperature.
$T_{N2}^{vib}, T_{O2}^{vib}, T_{No}^{vib}$. For the vibrational modes of the molecular components, separate temperatures is introduced. When considering flows in thermal equilibrium, numerical simulations assign a same temperature to all modes. The translational pressure is the only factor that affects the pressure.

The sum of kinetic and interior energies is defined as the total energy E per unit mass:

$$E = \frac{1}{2}(u^2 + v^2) + \sum X_a e_a \tag{2.11}$$

Where

- e_α is the total specific energy per unit mass of the species α,
- u and v are the velocity components x, y indirections, respectively.

2.3.2 Chemical kinetic model:

The chemical source names are formed from reactions that take place between the gas's constituents. A mass transfer mechanism occurs between species as reactions occur. The term wα on the right-hand side of the species conservation equation represents this. Eq. 2.1.

The formulas for these mass transfer rates are determined in this section. Several separate elementary chemical reactions between species in the gas can take place at the same time. Consider the rth chemical reaction of Nr elementary reactions between Ns chemically reacting species:

$$\sum v'_{\alpha,r} X_\alpha = \sum v''_{\alpha,r} X_\alpha \qquad (2.12)$$

Where

- $v'_{\alpha,r}$ and $v''_{\alpha,r}$ represent the stoichiometric mole numbers of reactants and products of reaction r, respectively.
- X_a is the molar concentration of the species α.

The forward and backward reaction rates are calculated as follows:

Eorward:

$$\frac{d[X_\alpha]_r^f}{dt} = \left(v'_{\alpha,s} - v'_{\alpha,r}\right)\left[k_{f,r}\prod_{\alpha=1}^{N_s}\,[X_\alpha]^{v_{s,r}}\right] \qquad (2.13)$$

Backward:

$$\frac{d[X_a]_s^b}{dt} = \left(v^*_{\alpha,5} - v'_{\alpha,5}\right)\left[k_{b,r}\prod_{a=1}^{N_a}\,[X_a]^{v_{s,}}\right] \qquad (2.14)$$

Where

- $K_{f,r}$ and K_{hr} are the forward and backward reaction rate coefficients of reaction r, which are both affected by the temperature of the reaction.

- The net rate for the above general reaction r can be written as

$$\frac{d[X_a]}{dt} = \frac{d[X_a]_r^f}{dt} -= \left(v_{\alpha,r}^* - v_{\alpha,r}\right)\left[k_{f,r}\prod_{a=1}^{N_s}\ [X_a]^{k_s} - k_{b,r}\prod_{a=1}^{N_s}\ [X_a]^{v_\alpha}\right] \quad (2.15)$$

The equation above is a general form of the law of mass action, which assures that total mass is preserved during a chemical reaction.

The mass rate of species production per unit volume is calculated as follows:

$$w_\alpha = \frac{d}{dt}(\rho_\alpha) = M_a \sum_{r=1}^{N_e} \frac{d}{dt}[X_a]_r \qquad (2.16)$$

When the necessary equations for the forward and backward rate coefficients are provided for a collection of Nr reactions, a chemical kinetic model is defined. Experimentally measured forward reaction rates are common. Many reactions have empirical relationships that can be connected in the form of :

$$K_{f,r} = C_{f,r} T_{f,r}^{n_{f,r}} e^{\frac{-E_{f,}}{kT_{i,}}} \qquad (2.17)$$

Where

- $E_{f,r}$ is the activation energy

- $C_{t,r}$ is a constant.

Experimental data is used to determine the parameters $C_{f,x}, n_{f,r}$, and the activation energy $E_{f,x}$ for various reactions. The backward reaction rate coefficients are presented under the normal assumptions.

$$k_{b,r} = \frac{k_{f,r}\left(T_{b,r}\right)}{k_{\mathrm{sap,r}}\left(T_{b,r}\right)} \qquad (2.18)$$

Where

- $k_{\mathrm{eq},,}$ is the equilibrium constant for the r$^{\mathrm{th}}$ reaction. The activation energy of the forward reaction and the partition functions of the reactants and products can be used to calculate the equilibrium constant. The activation energy of the forward reaction and the partition functions of the reactants and products can be used to calculate the equilibrium constant.

- In the present work, a five component air model consisting of species $\mathrm{N_2, O_2, NO, N}$ and O is considered. The most important chemical reactions between these species are:

$$
\begin{aligned}
&\mathrm{N_2 + M \rightleftharpoons 2\,N + M}\\
&\mathrm{O_2 + M \rightleftharpoons 2O + M}\\
&\mathrm{NO + M \rightleftharpoons N + O + M}\\
&\mathrm{NO + O \rightleftharpoons N + O_2}\\
&\mathrm{N_2 + O \rightleftharpoons NO + N}
\end{aligned}
$$

• M is the catalyst particle that acts as a collision partner in the reaction.[10]

The first three reactions are dissociation events, whereas the last two are bimolecular exchange reactions. The two most essential events for the generation of nitric oxide NO in air are the exchange reactions. It should be noticed that the sum of the mass transfer rates is identically zero and that elemental conservation holds, as necessary, when determining the chemical source term.

2.3.3 Vibration-dissociation coupling:

Chemical changes in molecules, such as dissociation and recombination, are influenced by their internal chemical states of motion. Only molecules with a total energy level above a certain threshold can initiate a chemical transformation. At high temperatures, the durations of chemical and vibrational relaxation are comparable, leading to reciprocal interaction. The vibrational temperature of a shock wave is lower than the translational-rotational temperature. Due to the molecules having less vibrational energy than at equilibrium, the non-equilibrium molecular dissociation rate is lower than the equilibrium dissociation rate. Therefore, the dissociation rate must be adjusted in the presence of vibrational nonequilibrium. [10]

Additionally, vibrationally excited molecules are more likely to dissociate, which drains vibrational energy and slows down vibrational relaxation. Understanding and quantifying this interaction is crucial for accurately predicting nonequilibrium dissociation rates. The accurate prediction of nonequilibrium dissociation rates is essential because they heavily influence macroscopic flow properties such as heating rates and shock wave forms. Even small changes in shock wave shape and resulting pressure field differences can lead to significant variations in anticipated aerodynamic forces.

2.5 Turbulence modelisation:

2.5.1 Introduction:

In the literature, three main methods to modelling turbulent flows are provided. Statistical Navier Stokes equations modelling, direct simulation, and large-scale simulation are examples of these. [11] The modelling and simulation of turbulence are fundamentally different.

2.5.4 Statistical modelling (RANS):

RANS (Reynolds Averaged Navier Stokes), is used to describe the mean movement of turbulent flow [11].The mixing-length model, two-level models, the Algebraic Stress Model (ASM), and the second-order Reynolds Stress Model are among the models that have been created (RSM). It's a model that produces good results while requiring minimal resources.

Averaged equations:

Direct simulation of the instantaneous Navier-Stokes's equations is still limited to low Reynolds number flows and simple geometric designs. When we're looking for realistic flows, an alternative is to be just interested in average quantities and hence to acquire the system of equations that these quantities verify. To do so, practice the Reynolds decomposition on the problem's unknowns and apply the set average operator to the instantaneous equations. Averaged equations are the new equations obtained.[12] The solution of the general equations of viscous fluid motion, which include the continuity and Navier-Stokes's equations, is required for many flows of technical significance. As a result, continuity equation can be written as:

$$\frac{\partial u_i}{\partial x_j} = 0 \tag{2.19}$$

And the momentum equation :

$$\frac{\partial u_i}{\partial t} + u_j \frac{\partial u_j}{\partial x_j} = -\frac{1}{\rho}\frac{\partial p}{\partial x_j} + v\frac{\partial^2 u_i}{\partial x_j\,\partial x_j} \tag{2.20}$$

- The equations of mean motion

  n the case where the flow is turbulent, decomposing the instantaneous variables (such as relocity components and pressure) into a mean value and a fluctuating value is desirable.

$$u_{(x,t)} = U_{(x,t)} + u'_{(x,t)} \tag{2.21}$$

$$p_{(x,x)} = p_{(x,y)} + P'_{(x,t)} \tag{2.22}$$

When measuring flow quantities, we are more interested in mean values than fluctuating ralues. Instead of that, solving numerically the Navier-Stokes's equation would necessitate an xtremely fine grid to resolve all turbulent scales, as well as a fine time resolution.

Ne get the following result for the mean field by introducing the Reynolds decomposition into he continuity equation and obtaining the ensemble mean :

$$\frac{\partial \mathrm{U_i}}{\partial \mathrm{x_i}} = 0 \tag{2.23}$$

Ne get the velocity fluctuations by subtracting this equation from the equation of instantaneous notion continuity:

$$\frac{\partial u_i}{\partial x_i} = 0 \tag{2.24}$$

As a result, we can see that both the mean and fluctuation quantities confirm the continuity equation.

The following are the three components of the average velocity:

$$\frac{\partial U_i}{\partial t} + U_j \frac{\partial U_i}{\partial x_j} + u_j \frac{\partial u_i}{\partial x_j} = -\frac{1}{\rho \frac{\partial P}{\partial x_i}} + v \frac{\partial^2 U_i}{\partial x_j \, \partial x_j} \tag{2.25}$$

The incompressibility criterion for fluctuations implies that:

$$\overline{u_J \frac{\partial u_\iota}{\partial x_J}} = \overline{\frac{\partial u_\iota}{\partial x_J}} \tag{2.26}$$

The Reynolds tensor is therefore defined as follows:

$$R_{ij} = -\rho \overline{u_\iota \tilde{u}_J} \tag{2.27}$$

Finally, the averaged equations are written as:

$$\frac{\partial U_i}{\partial t} + U_j \frac{\partial U_i}{\partial x_j} = -\frac{1}{\rho}\frac{\partial P}{\partial x_i} + \frac{1}{\rho}\frac{\partial}{\partial x_j}\left(\overline{\tau_{\iota J}} + R_{ij}\right) \tag{2.28}$$

Where,

$$\overline{\tau_{1J}} = \mu\left(\frac{\partial u_i}{\partial x_j} + \frac{\partial u_j}{\partial x_l}\right) \tag{2.29}$$

As a result, the equations of the mean field of velocity differ from the equations of continuity and momentum in this form, because a new term related to the effect of the fluctuating field

shows in these equations. This term is known as the Reynolds stress and it expressed as:[12]

$$R_{ij} = -\rho \begin{bmatrix} \overline{u'u'} & \overline{u'v'} & \overline{u'\omega'} \\ \overline{u'v'} & \overline{v'v'} & \overline{v'\omega'} \\ \overline{u'\omega'} & \overline{v'\omega'} & \overline{\omega'\omega'} \end{bmatrix} \tag{2.30}$$

As a result, this tensor generates six more unknowns. Thus, close the RANS equations by modelling the Reynolds stress term R_{ij} as a function of the mean flow, removing any reference to the fluctuating part of the velocity. This is the issue of closure.

The problem of closure:
We have four unknown functions U_1, U_2, U_3, and P, as well as four equations, the continuity equation and the three NAVIER-STOKES equations, with the Reynolds equations substituting the NAVIER-STOKES equations, for a turbulent issue, we have the 6 unknown functions of the Reynolds tensor $u_i u_j$, therefore we have 10

unknown functions but only 4 equations in the general case. The system, is not closed. To solve this problem, you'll need to find a sufficient number of additional equations.

This is the central problem of turbulence, problem of closure. For this, many researchers have invested in the field and several contributions of resolution models have been proposed. Among these models we can cite:

Classification of turbulence models:

There are two types of models in general:

- First-order models (turbulent viscosity models), which involve modeling Reynolds stresses directly using a turbulent viscosity.
- Second-order models: The Reynolds stresses are directly estimated.[13]

There are numerous types of turbulence models for first-order models dependent on the number of equations of fluctuating motion added to the conservation equations:

2.5.4.3 Two-equation model:

The turbulent kinetic energy k and its dissipation ε are described by two transport equations[13]. The Reynolds stress tensor is calculated using an assumption that links the Reynolds stress tensor to velocity gradients and eddy viscosity.

2.5.4.4 k-omega k- $\boldsymbol{\omega}$ model

The K-omega ($k - \omega$) model is a two-equation model, meaning it adds two additional transport equations to explain the flow's turbulent features. This model also solves two more PDEs: [14]

The conventional k equation is solved, but it is employed as a length determining equation. From its definition $\omega \propto \frac{\varepsilon}{k}$., this quantity is commonly referred to as specific dissipation.

2.5.4.4.1 The transport equations for the standard model $k - \omega$:

The following transport equations yield the turbulent kinetic energy (k) and the specific rate of dissipation (ω).

$$\frac{\partial(\rho k)}{\partial t}+\frac{\partial(\rho k U_j)}{\partial x_j}=P-\beta^*\rho\omega k+\frac{\partial}{\partial x_j}\left[\left(\mu+\sigma_k\frac{\rho k}{\omega}\right)\frac{\partial K}{\partial x_j}\right]$$

$$\frac{\partial(\rho k)}{\partial t}+\frac{\partial(\rho k U_j)}{\partial x_j}=P-\beta^*\rho\omega k+\frac{\partial}{\partial x_j}\left[\left(\mu+\sigma_{\&}\frac{\rho k}{\omega}\right)\frac{\partial K}{\partial x_j}\right]$$

Following that, the turbulent viscosity is determined as follows: [14]

$$\mu_t=\rho\frac{k}{\omega}$$

2.5.4.4.2 The constants and auxiliary functions for the model $k-\omega$

The various closure coefficients of the $\mathrm{k}-\omega$ model is given as

Table 2.2 The various closure coefficients of the $\mathrm{k}-\varepsilon$ model [14]

σ_k	σ_ω	β^*	γ	C_{Lim}	β_0
0.6	0.5	0.09	$13/25$	$7/8$	0.0708

2.5.5 Wall function:

Some mature turbulence models, are only valid in fully formed turbulence and do not function well in the vicinity of the wall. The employment of so-called wall functions, which can model the near wall region. The first cell center must be positioned in the log-law zone to assure the accuracy of the outcome. Wall functions are empirical equations used to fulfill the physics of the flow in the near wall region. Rather than specifying boundary conditions at the wall, wall functions are utilized to bridge the inner region between the wall and the turbulence fully formed region in order to provide near wall boundary conditions for the momentum and turbulence transfer equations.

[15] It should be noted that when employing the wall functions approach, the boundary layer does not need to be resolved, resulting in a significant reduction in mesh size and computing domain. Approximations of "log - layer," are wall functions. The “law of the wall” describes the velocity profile.

$$u(y)=u\tau\kappa(\ln y+C) \qquad (2.36)$$

Where :

- κ is von Karman constant
- The constant C is affected by the roughness of the wall as well as the friction velocity.

Wall law:

The wall y+ is a non-dimensional number that determines whether the influences in the wall-adjacent cells are laminar or turbulent, and hence indicates which part of the turbulent boundary layer they resolve.

In a turbulent boundary layer,

the subdivisions of the near-wall area can be summarized as follows [16]:

- $y+ < 5$: viscous sublayer region (velocity profiles are considered to be laminar, and viscous stress dominates wall shear): [15]
- $5 < y+ < 30$: buffer region (both viscous and turbulent shear dominates)
- $30 < y+ < 300$: Fully turbulent portion or log-law region (corresponds to the region where turbulent shear predominates).

2.6 Calculation of Radiative Transfer in a Hypersonic Flow :

2.6.1 Radiative Transfer in a Hypersonic Flow :

In the realm of hypersonic flows, understanding and accurately predicting radiative transfer phenomena are paramount for various aerospace applications. This section of the thesis delves into the intricate calculations involved in assessing radiative transfer within hypersonic flows. Radiative transfer plays a significant role in shaping the thermal and chemical environment of hypersonic vehicles during atmospheric entry, affecting both their aerodynamic performance and thermal protection system design. The primary focus lies in developing methodologies to calculate radiative properties within hypersonic flows, encompassing the formulation of pertinent equations and the utilization of computational models to solve them. Through this investigation, we aim to deepen our comprehension of radiative heat transfer mechanisms and enhance our capability to engineer robust solutions for hypersonic flight regimes.

2.6.2 Radiation equilibrium laws :

2.6.2.1 The Planck function :

In the case where the gaseous medium is in thermal equilibrium, there exists at every point an equilibrium radiation. The intensity of this radiation is independent of direction and depends only on wavelength and temperature. The expression for this intensity is given by the Planck function:

$$I_\lambda^0(T) = \frac{2hc^2}{\lambda^5}\left[\mathrm{Exp}\left(\frac{hc}{k_b\lambda T}\right) - 1\right]^{-1} \qquad (2.37)$$

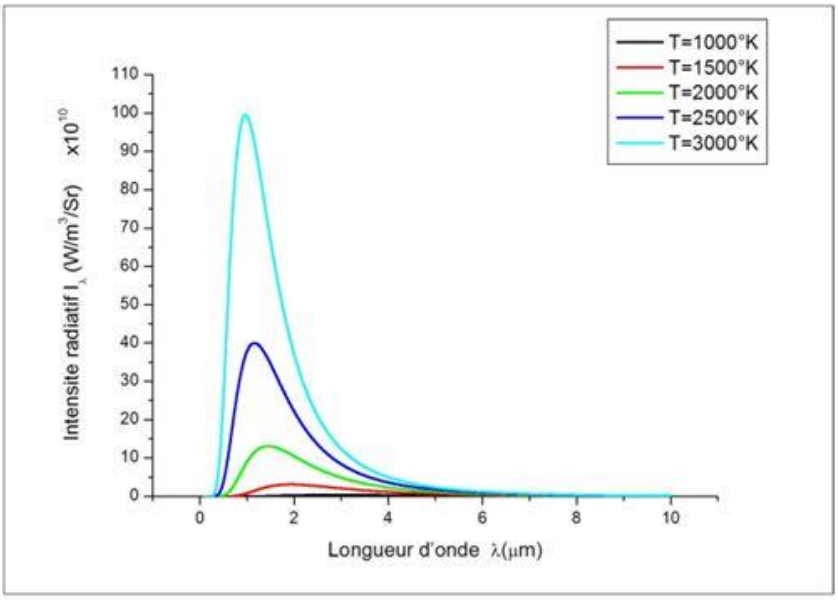

Figure 2.2 : Variation of the Planck function in fonction of wave length avec temperature effect[17]

$I_\lambda^0(T)$ is expressed as $(W^{-3}\mathrm{sr}^{-1})$

2.6.2.2 The Wien's Law :

When we graphically represent the evolution of the Planck function as a function of wavelength for different temperatures (Figure 2.2), we observe that this intensity has a maximum value for a wavelength max corresponding to the temperature. This relationship is described by Wien's displacement law: [17]

λmax T = 2.898 × 10^-3 [m*K]

2.6.2.3 The Stefan-Boltzmann Law :

The Stefan's Law expresses the relationship between the total radiated power, temperature, and the surface area of the medium. It is obtained by integrating the Planck function over the entire wavelength domain:

$$\int_0^{\infty} I_\lambda^0(T)d\lambda = \frac{\sigma_S T^4}{\pi} \tag{2.38}$$

Where σ_s is the stefan constant :

$$\sigma_S = \frac{2\pi^5 {k_b}^4}{15C^2h^3} \tag{2.39}$$

And $\sigma_S T^4$ represents the energy radiated per second per unit area at temperature T. This law, which relates total intensity (total emitted energy) to temperature, clearly demonstrates the significance of radiation at high temperatures.

2.6.2.4 Kirchhoff's Law :

When in thermal equilibrium, the absorbed flux equals the emitted flux, and the intensity, in all directions and at every point, is equivalent to that of equilibrium radiation (Iλ(T) defined by Planck's law). Consequently, we can express the emissivity coefficient in terms of the absorption coefficient by the following relationship [17], defining Kirchhoff's law:

$$\varepsilon_\lambda(T) = k_\lambda(T) \times I_\lambda^0(T) \tag{2.40}$$

Where :

$$\frac{\varepsilon_\lambda(T)}{k_\lambda(T)} = I_\lambda^0(T) = \frac{2hv^3}{C^2}\left[\mathrm{Exp}\left(\frac{hv}{k_bT}\right) - 1\right]^{-1} \tag{2.41}$$

And :

- $\varepsilon_\lambda(T)$: Emission coefficient

- $k_\lambda(T)$: Absorption coefficient

2.6.3 Radiative Flux :

In the general case, the field of directional intensity is determined by solving an equation called the radiative transfer equation (RTE). This equation is derived by considering the evolution, between two positions *x* and *x+dx*, of the directional radiative flux propagating within the solid angle dΩ centered around the direction Δ, through the element dx normal to it (Figure 2.3).

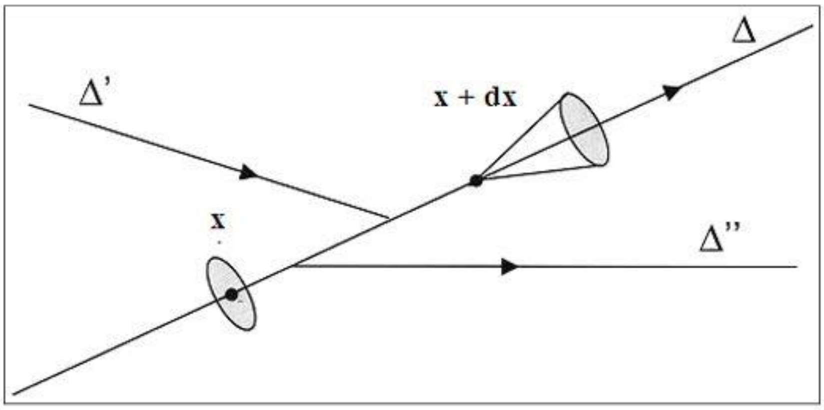

Fig 2.3: Geometric parameters for the evolution of flux along the optical path [18]

The radiative flux is also obtained by integrating the spectral intensity over all wavelengths and all possible directions :

$$q^{md} = \iint_{\Omega} I_\lambda d\lambda d\Omega \qquad (2.42)$$

2.6.3.1 The global Radiative Transfer Equation (RTE) :

In media with unit optical index, the mathematical formulation of the RTE is as follows ;

$$\frac{dI_\lambda(x,\Delta)}{dx} = \underbrace{\varepsilon_\lambda(x)}_{\text{emission}} + \underbrace{\frac{\sigma_\lambda(x)}{4\pi}\int_0^{4\pi} P_\lambda(\Delta'' \to \Delta, x) I_\lambda(x,\Delta) d\Omega}_{\text{dispersion constructive}} - \underbrace{\big(k_\lambda(x) + \sigma_\lambda(x)\big) I_\lambda(x,\Delta)}_{\text{absorbtion +dispersion}} \qquad (2.43)$$

- In this expression :

  $k_\lambda(x)$: absorption coefficient

$\varepsilon_\lambda(x)$: Emission coefficient

$\sigma_{\hat{\lambda}}(x)$: Dispersion coefficient

$P_\lambda(\Delta'' \rightarrow \Delta, x)$: function of the dispersion phase

2.6.4 . Radiative properties of the medium (radiation emission and absorption)

In our applications, we will consider two important processes regarding the absorption and emission of radiation in species-field transitions, referred to by some authors as bound-free transitions.

2.6.5 Expression of the radiative flux and volumetric radiative power :

At any point in space, we define the radiative flux vector q^{rad} par la relation suivante [18]:

$$q^{sul}(x) = k_\lambda(x)\rho \int_0^\infty \int_0^{4\pi} I_\lambda(x,u) \parallel \vec{u} \parallel^{u \leq u\Omega\Omega} \tag{2.44}$$

The volumetric radiative power at a point s is expressed as the negative of the divergence of the radiative flux

$$P^{rad}(x) = -[\nabla q^{rad}]_x \tag{2.45}$$

Where :

$$P^{\mathrm{nud}}(x) = -\int_0^\infty \int_{4=} \frac{dI_\lambda(x,u)}{dx} d\Omega d\lambda \tag{2.46}$$

Chapter 3

Numerical modelization

3.1 introduction :

Numerical modeling in fluid mechanics involves applying mathematical and computational methods to simulate incompressible fluid flow, critical across industries like aerospace, maritime, and medicine. Computational Fluid Dynamics (CFD) is pivotal, allowing detailed study of fluid behavior in diverse scenarios. Theoretical and Numerical Methods for Fluid Mechanics encompass error analysis, equation roots, Navier-Stokes equations, and methods like finite differences, Fourier decomposition, and stability analysis. Modern techniques such as finite volume, finite element, and spectral methods are fundamental for engineering modeling.

Various numerical computation codes, whether commercial, open-source, or institution-specific, are available. For our project, ANSYS Fluent CFD software will be utilized. ANSYS Fluent is renowned for its robust physics modeling capabilities, accurately simulating fluid flow, heat transfer, chemical reactions, and more. Its user-friendly interface simplifies the entire CFD process from preprocessing to post-processing, offering sophisticated physics models and customizable environments. Features like single-window workflow enhance efficiency in analyzing complex fluid dynamics scenarios, making ANSYS Fluent a preferred choice in engineering simulations.

3.2 Introduction to the Fluent Computational Code :

ANSYS FLUENT is a commercial Computational Fluid Dynamics (CFD) code, designed to model fluid flows and heat transfers in complex geometries.

The main steps of a simulation in Ansys Fluent involve several stages, beginning with the preparation of the geometry and ending with the analysis of the results. Here are the primary steps:

Preparing the geometry: Create a watertight geometry suitable for a CFD simulation using Ansys Discovery or another appropriate tool. Ensure that the geometry meets the requirements for a successful simulation.

3.3 Meshing:

Mesh generation in Ansys Fluent is a critical process that involves dividing the computational domain into small sub-volumes to solve fluid dynamics equations accurately. Here is an elaboration on mesh generation based on the provided search results:

- Importance of Meshing : Meshing, also known as mesh generation, is crucial for structural Finite Element Analysis (FEA) and Fluid Computational Fluid Dynamics (CFD) simulations. A detailed mesh enhances the accuracy of 3D CAD models, leading to high-fidelity simulations.

- Ansys Meshing Capabilities: Ansys provides high-performance automated meshing software that caters to FEA, CFD, and other multiphysics solutions. The software offers a range of meshing methods from easy automated meshing to highly crafted meshing, covering a spectrum from high-order to linear elements.

- Mesh Generation Process: Once the geometry is prepared, the computational domain is divided into small sub-volumes where fluid dynamics equations are solved to understand fluid behavior around objects. Creating an appropriate mesh is fundamental for engineering simulations as it influences accuracy, convergence, and simulation speed.

- Ansys Fluent Meshing Technology : Ansys Fluent incorporates advanced automated mesh generation tools that provide faster and more accurate solutions for CFD simulations. Recent updates to Fluent Meshing introduce Mosaic-enabled meshing technology that automatically generates different mesh and element types in different regions, optimizing accuracy and speed.

- Optimizing Mesh Quality: Ansys Polyflow offers advanced fluid dynamics technology for industries like polymer, glass, metals, and cement processing. Ansys Chemkin-Pro specializes in modeling complex gas phase and surface chemistry reactions. Ansys TurboGrid complements rotating machinery simulation with a specialized tool for rapid 3D design of rotating machinery components.

The computational domain is defined by a mesh that represents the fluid and the solid faces involved. The key components of the mesh include:

- Cell: Control volume dividing the geometry.

- Face : Boundary of a "cell" where boundary conditions are defined.
- Edge: Boundary of a "face."
- Node: Mesh point.
- Zone: Group of "nodes," "faces," and/or "cells."

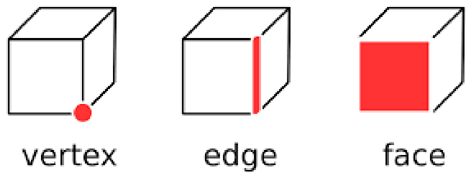

Figure 3.1 : Mesh component

3.3.1 Importance of Mesh quality :

Mesh quality serves as the foundation upon which accurate and reliable computational fluid dynamics (CFD) simulations are built. By ensuring a high-quality mesh, researchers and engineers can enhance the precision and credibility of their numerical analyses.

3.3.2 Diffrenet criteria of quality :

3.3.2.1Skewness :

Skewness in meshing is a critical quality metric that plays a significant role in ensuring the accuracy and reliability of computational simulations. In the context of Ansys Fluent,
skewness is evaluated to determine the deviation of the edge and angle of the mesh from the ideal state, such as an equilateral triangle or square.
The skewness value is calculated based on the difference between the ideal cell size and the actual cell size, with lower values indicating a better quality mesh. Skewness can be assessed using different methods :
such as the equilateral volume method or the angle deviation method, each providing insights into the quality of the mesh elements.

- ✓ Maintaining low skewness values is essential as highly skewed elements can lead to numerical inaccuracies and convergence issues in simulations. By understanding and managing skewness effectively, engineers and researchers can optimize mesh quality, improve simulation results, and enhance the overall reliability of their computational fluid dynamics analyses.

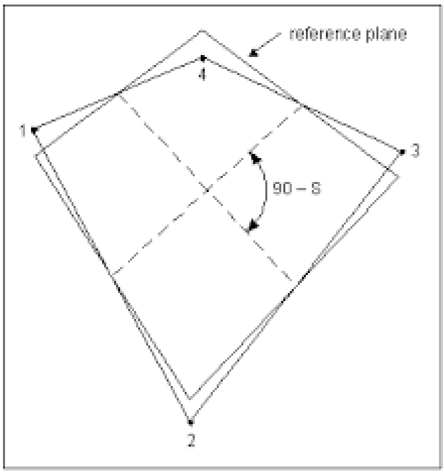

Figure 3.2 : (skewness)[21]

3.3.2.2 The non – orthogonal quality :

Non-orthogonal quality is a crucial mesh metric that measures the angle between the vector connecting two adjacent cell centers and the normal of the face shared by these cells. In the context of computational fluid dynamics (CFD) simulations, maintaining good non-orthogonal quality is essential for ensuring numerical stability and solution accuracy. A lower non-orthogonality value indicates a more orthogonal mesh, which is favorable for efficient and reliable simulations.

- The range of non-orthogonality typically falls between 0 (ideal) and 90 (worst), with 0 representing an orthogonal mesh.
- High levels of non-orthogonality can lead to numerical instability, causing simulations to take longer to converge or even diverge.
- To ensure robust CFD simulations, it is recommended to keep the non-orthogonality below a certain threshold, such as 70, to maintain computational efficiency and accuracy in the results.

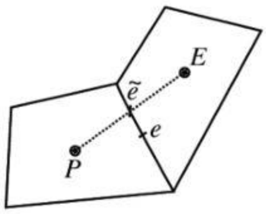

Figure 3.3 : The non orthogonality [33]

3.3.2.3 Aspect ratio :

Aspect ratio is the measure of a mesh element's deviation from having all sides of equal length. A high aspect ratio occurs with long, thin elements. Entering an overly large value for the **Minimum Element Size** mesh control may cause the mesh generator to create solid elements with high aspect ratios.

Creo Simulate calculates aspect ratio, R, according to this formula:

$$R = E/h \tag{3.1}$$

where E is the longest edge and h is the shortest height—the distance between a vertex and the opposite surface or edge.

3.4 Problem and Solution :

In this study, our goal is to simulate hypersonic flows around blunt bodies re-entering the atmosphere in two dimensions, considering viscosity and chemical imbalances. We assume a chemical flow at vibrational equilibrium and we take radiation into consideration , as they become significant only at speeds exceeding 8000 m/s. Our model treats air as a mixture of five ideal gases ($O2$, $N2$, NO, O, N) in chemical nonequilibrium.

Initially, we focus on a simplified scenario using a "half sphere" model, specifically the "Lobb" sphere, to better grasp the phenomenon and refine our computational code. Subsequently, we extend our analysis to a delta profile resembling a typical shuttle orbiter configuration, maintaining the same Lobb sphere radius. This step aims to determine the optimal re-entry trajectory design.

3.4.1 Mesh and geometry :

3.4.1.1 Part A. study of physicochemical processes in a shock layer around a blunt body The rounded body chosen for the simulation was the "Lobb" sphere experiment performed on a sphere-cone body with:

- ✓ The radius of the sphere is R = 6.35mm
- ✓ the length of the cylinder is 1.3m Th study was simulated under the flowing free stream conditions.

Table 3.1 Lobb sphere free stream boundary condition [22]

α	M_∞	Reaction. N	T_∞[k]	$\rho_\infty(\mathrm{kg/m^3})$	P_∞[Pa]	K	ω
0°	15.35	5	293	7.89610^{-3}	664	3245.962	64.607

3.4.1.1.1 Geometry Creation :

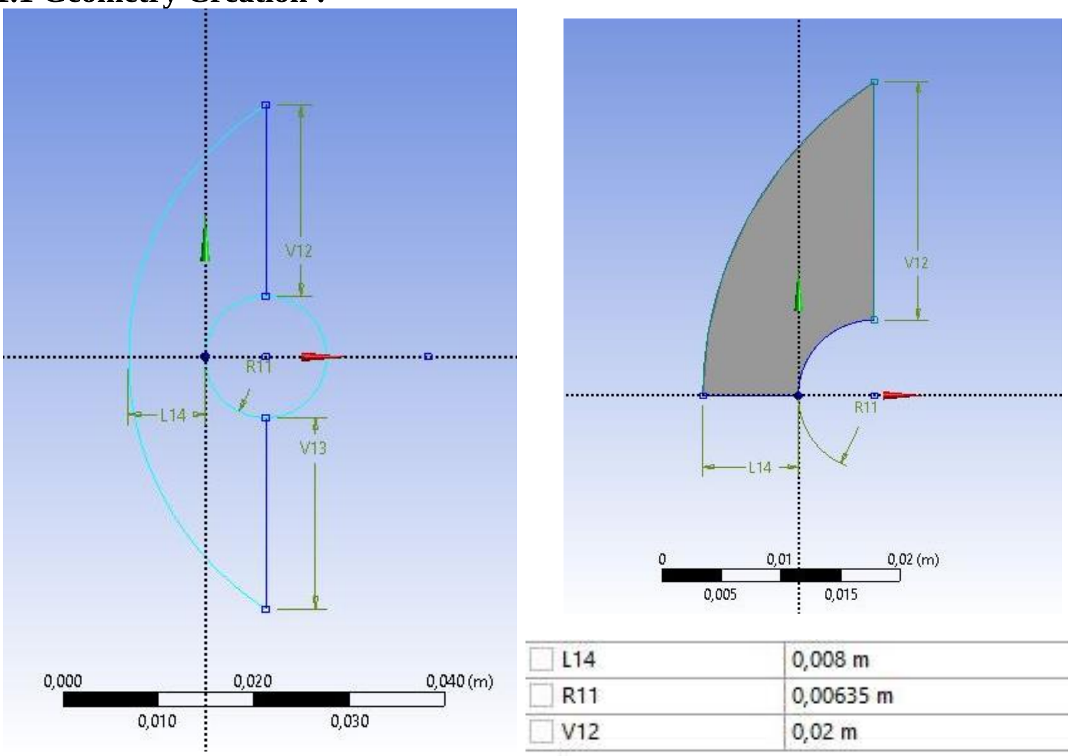

Figure 3.4 : Lob sphere geometry creation and cotation.

The initial stage of the simulation involves constructing the geometry of the problem using ANSYS

DesignModeler software. The geometry is designed to facilitate simulation using axisymmetric Navier-Stokes equations. Consequently, a two-dimensional symmetric geometry is crafted, with an axis defined at the radial center of the body under study. This approach allows for a reduction in the computational domain and, consequently, a decrease in calculation time.

3.4.1.1.2 Mesh construction :

Our geometry is characterized by its simplicity, where the flow closely follows the shape of the geometry itself. To ensure optimal alignment between the flow and our mesh, we opt for a quadrilateral cell mesh.. Therefore, we initiate the process with a structured 2D mesh composed of quadrilateral cells to ensure accurate representation of the flow dynamics.

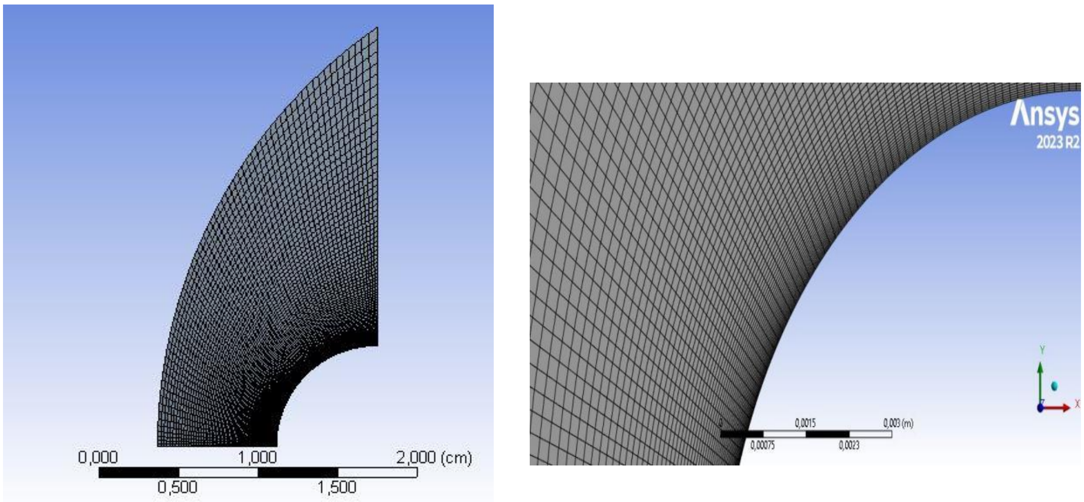

Figure 3.5: Lob sphere Mesh

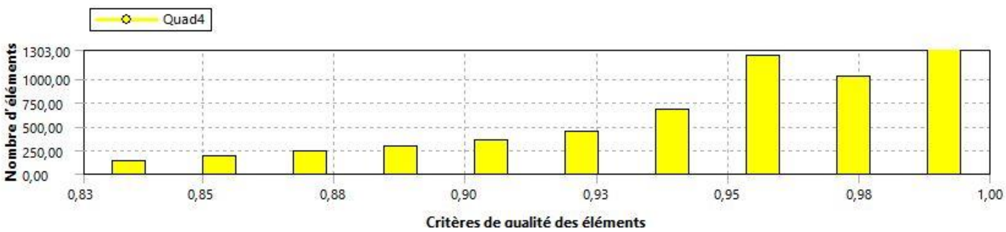

Orthogonal quality

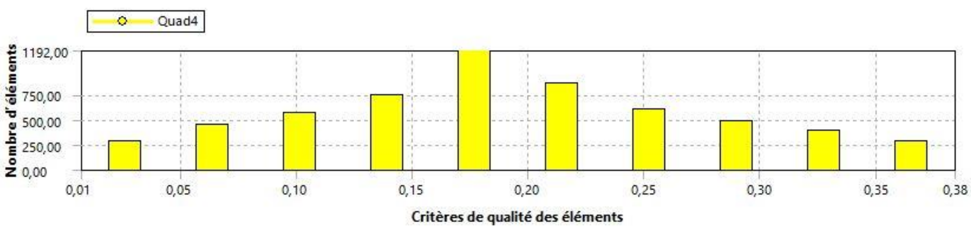

Skewness

3.4.1.1.3 Identification of the boundary condition :

We're bound to label each boundary in the geometry by creating named selections (inlets, the outlet, body and the symmetry surface) In order to simplify our work later on ANSYS Fluent

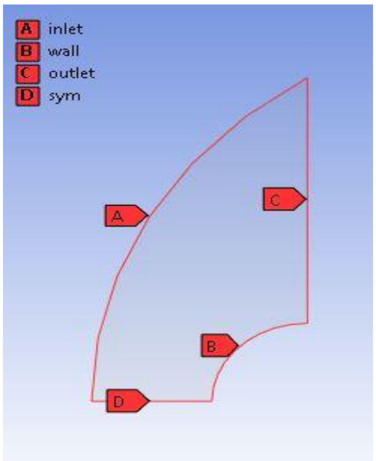

Figure 3.6 : Lob sphere Identification of Boundary conditions

3.4.1.2 Part B: Study of re-entry trajectory design over delta body profile

Assuming the same flow hypothesis, we simulate a blunted delta profile body with the same nose radius of the previous blunted Lobb sphere.

- R=0.00635m
- Length of 0.23m
- Sweep angle 15°

3.4.1.2.1 Delta profile

In order to study the flow along body surface streamline, we simulate a flow over a delta body profile so that we can study the trajectory design: the maximum deceleration, maximum heating rate and wall temperature with respect to angle of attack, altitude, re-entry velocity variations. The free flow condition is obtained based on the flight condition for three typical shuttle trajectory points in the altitude range of 60.96 to 76.20 km (200 000 to 250 000 ft) at velocities of 4.88 to 7.32 km/sec (16 000 to 24 000 ft/sec), respectively.[36]

3.4.1.2.1.1 Geometry Creation :

Similarly, we sketch the delta profile geometry. However, this time we cannot divide the computational domain, as the flow will lose its axisymmetry when the angle of attack is altered.

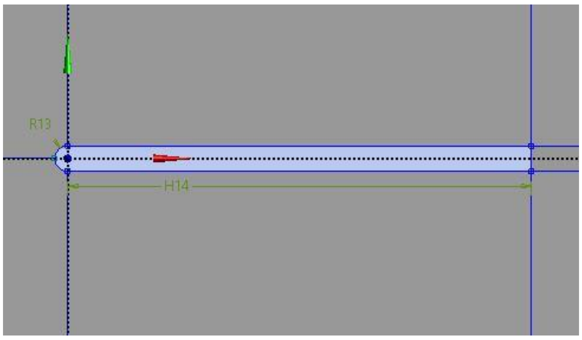

H14	23 cm
R13	0,635 cm

Figure 3.7 : Profile geometry creation

3.4.1.2.1.2 Mesh construction

The flow follows a geometric shape, so a structured grid with quadratic cells was developed for the computational domain.

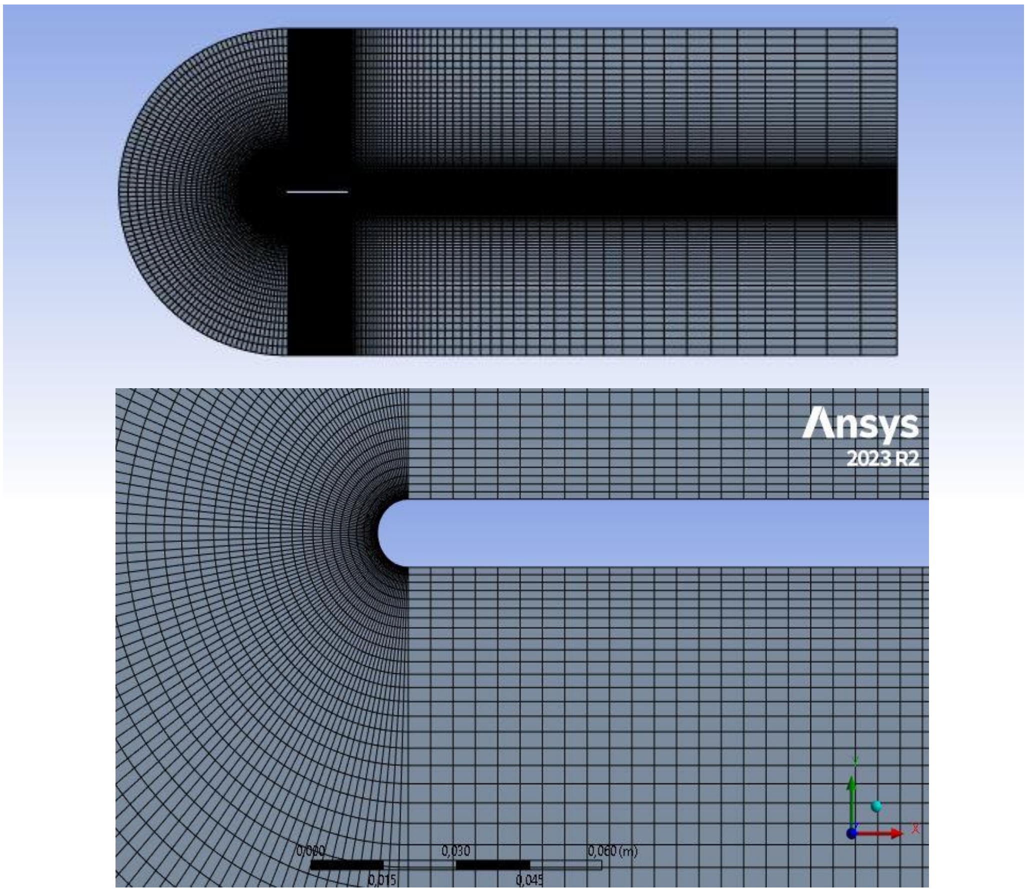

Figure 3.8 : Delta profil Geometry and Mesh

Orthogonal Quality

Skewness

3.4.1.2.1.3 Identification of the boundary conditions

The top boundary was extended 5L vertically from the ground of the model and 5L from the side walls. Where L is the length of the wall and set to be 0.23m. On the other hand, the inlet and outlet boundary were extended 5H and 15H from the wall, respectively. The size of the domain was built based on recommendation **by Franke et al. [24] and Tominaga et al. [25].oumaima**

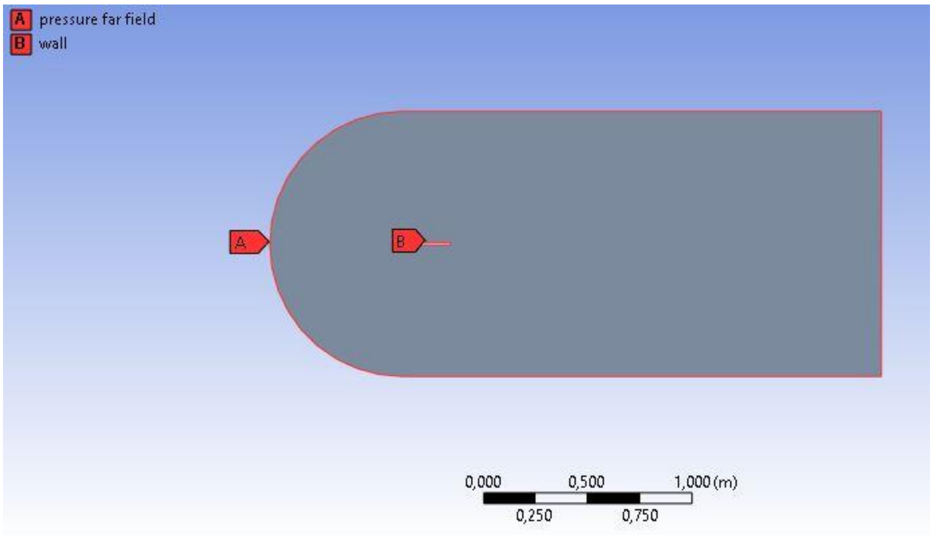

Figure 3.9 : : Identification of boundary conditions

3.4.2 Setting in data and simulation

3.4.2.1 Choice of calculation mode

under the Processing Options in Ansys FLUENT, you can find the Parallel Settings tab, which allows you to configure the simulation to run on multiple cores rather than a single core. Utilizing parallel processing enhances computational efficiency and reduces simulation time significantly.

Generally, the single-precision solver is adequate for most simulations. However, when dealing with problems that involve geometries with highly varying length scales, single-precision calculations may fall short in accurately representing the node coordinates. In such cases, double-precision calculations are essential to capture the intricate details and provide accurate results. Consequently, for our simulations, we will opt for the double-precision mode to ensure the precision required for resolving complex geometrical features.

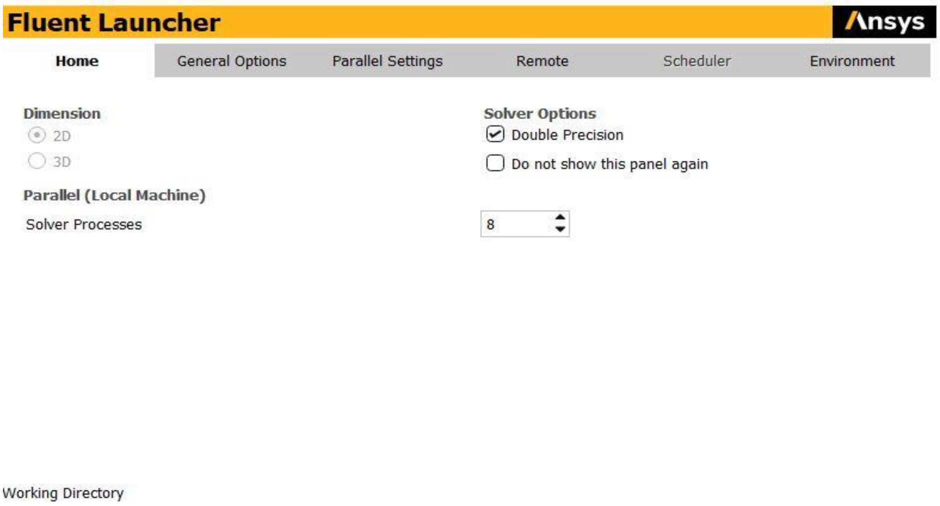

Figure 3.10 choice of calculation mode and type of dimension

4.2.2 Choice of solver:

In ANSYS FLUENT, choose the density-based solver for high-speed compressible flows with significant density variations due to shocks or chemical reactions. It's ideal for supersonic aerodynamics and explosive dynamics. Conversely, opt for the pressure-based solver for low-speed incompressible or mildly compressible flows, such as HVAC systems or water flow simulations, where density changes are negligible. This solver is robust for a wide range of applications, offering easier convergence and versatility in handling multiphase and complex boundary conditions.

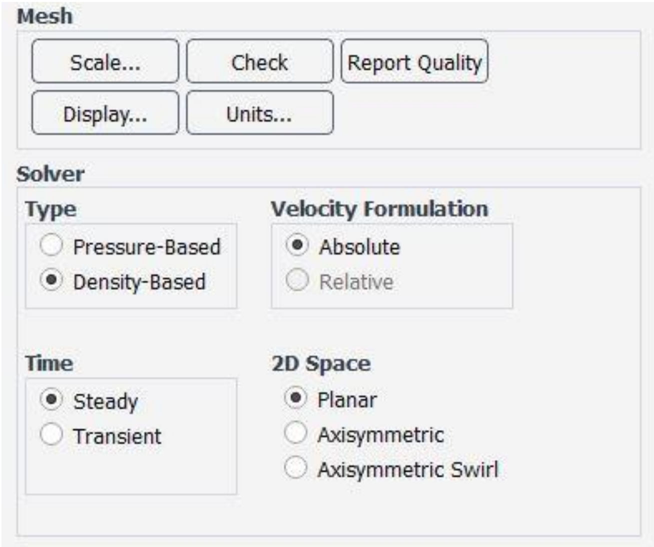

Figure 3.12 choice of solver

3.4.2.3 Choice of model

Ansys Fluent offers a range of models, starting with the activation of the energy equation as the initial step.

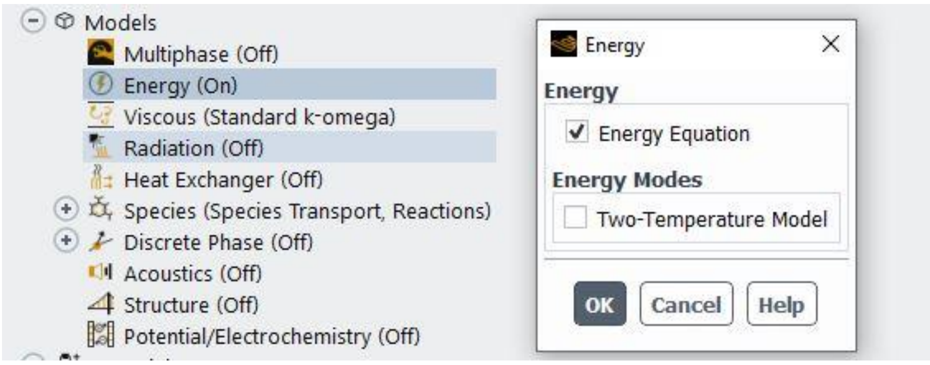

Figure 3.13 : choice of model

3.4.2.3.1 Choice of turbulence model

Choosing the appropriate turbulence model in ANSYS FLUENT depends on the specifics of your flow problem. Here are the key factors to consider:

Flow Characteristics

- **Laminar Flow:** If the flow is laminar, you might not need a turbulence model.

- **Turbulent Flow:** For turbulent flows, consider the following options.

Complexity of Geometry and Flow Patterns

- **Simple Flows:** For simple, steady-state flows, use the **k-epsilon** model. It is robust and converges quickly.

- **Complex Flows:** For complex geometries or flows with significant separation and recirculation, consider the **k-omega** model. It captures adverse pressure gradients and flow separation more accurately.

Flow Behavior and Specific Needs

- **Near-Wall Treatment:** For flows where near-wall treatment is crucial, such as boundary layer flows, the **k-omega** models or **Reynolds Stress Model (RSM)** might be appropriate.

- **Large Eddy Simulation (LES):** Use LES for high-fidelity simulations of large-scale turbulent structures, especially in transient analyses.

- **Detached Eddy Simulation (DES):** Use DES for flows with both large-scale and wall-bounded turbulence, balancing between LES and RANS models.

In our study we have chosen the model K Omega turbulence model for its superior accuracy in predicting near-wall flow behavior, which is crucial for hypersonic flows where surface heat transfer is significant. It performs well in scenarios with adverse pressure gradients, common during atmospheric reentry. Additionally, the model is more robust and stable forour complex flows involving strong shocks.

By considering these factors, you can select the most appropriate turbulence model for your specific simulation needs in ANSYS FLUENT.

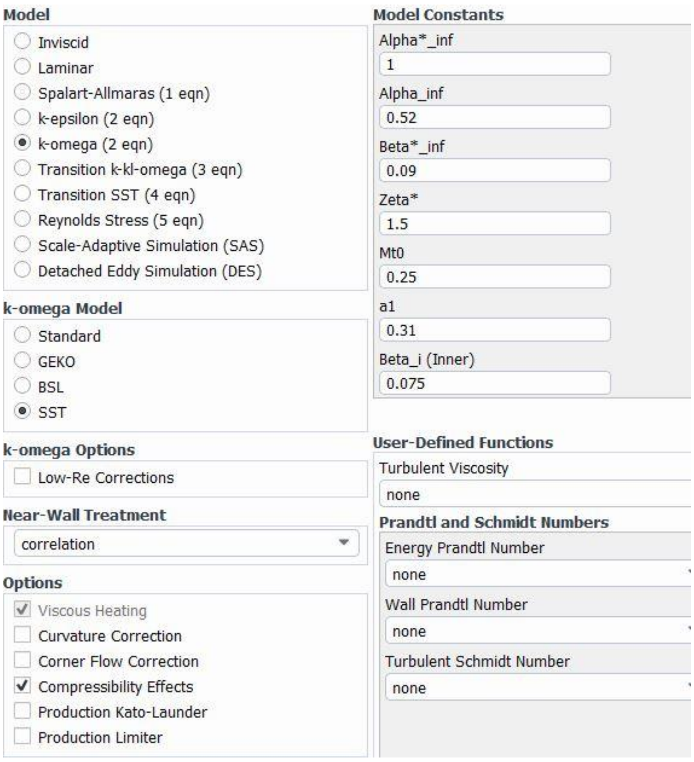

Figure 3.14 : Choice of turbulence Model

3.4.2.3.2 Building a Model for Species Reactions and Transport :

Building a model for species reactions and transport in ANSYS Fluent involves several steps. These steps will guide you through setting up the computational domain, defining materials, specifying reaction mechanisms, setting boundary conditions, and solving the model. Here’s a detailed process:

Models :

- **Species Transport**: Enable the species transport model under the "Models" tab.
- **Volumetric Reactions**: Enable volumetric reactions if your model includes chemical reactions occurring in the bulk phase.
- **Eddy Dissipation Concept**: For turbulent reacting flows, we consider using the Eddy Dissipation Concept model.

Materials :

- we Define the materials involved in your simulation. This includes all reactants, products, and possibly inert species.
- we Input necessary material properties such as density, specific heat, viscosity, and species diffusivities.

Figure 3.15 : choice of materials

Reactions :

- **Reaction Mechanisms**: we Define the chemical reactions.
    - We Go to the Reactions tab, add a new reaction mechanism.
    - We Specify the reactants, products, and their stoichiometric coefficients.
    - We Define the reaction rate parameters (Arrhenius constants).
- **Reaction Kinetics**: we Choose the appropriate kinetic model (e.g., Arrhenius, Eddy Dissipation).

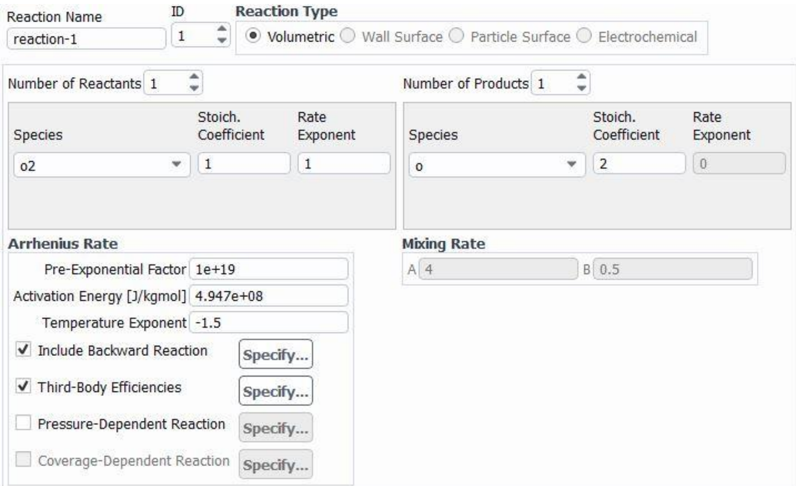

Figure 3.16 : setting reactions

The appropriate Reaction model will be displayed in the Reaction drop-down list in the Edit Material dialog box. The reactions are modeled in the following form:

$$O_2 + m \Leftrightarrow 2O + m$$
$$N_2 + m \Leftrightarrow 2N + m$$
$$NO + m \Leftrightarrow N + O + m$$
$$N_2 + O \Leftrightarrow NO + N$$
$$NO + O \Leftrightarrow N + O_2$$

Where M is the catalyst which can be any of the five species (O_2, N_2, NO, O, N).

Our reactions are reversible so we activate the Include Backward Reaction option and therefore the velocity exponent for each species is equivalent to the stoichiometric coefficient of that species which is the constant $v'_{i,r}$ and $v''_{i,r}$ in Equation 3.4. (Stoic. Coefficient = Rate Exponent),

$$\sum_{i=1}^{N} v'_{i,r}\mathcal{M}_i \rightleftharpoons^{k_{f,r}}_{k_{b,r}} \sum_{i=1}^{N} v''_{i,r}\mathcal{M}_i \tag{3.2}$$

In Fluent, and for reversible reactions the molar production rate of species s from reaction r is given by:

$$\hat{R}_{i,r} = \Gamma\left(v''_{i,r} - v'_{i,r}\right)\left(k_{f,r}\prod_{j=1}^{N}\left[C_{j,r}\right]^{\eta'_{j,r}} - k_{b,r}\prod_{j=1}^{N}\left[C_{j;r}\right]^{v'_{j,r}}\right) \tag{3.3}$$

- Where

  $v'_{i,r}$ stoichiometric coefficient for reactant i in reaction r

  $v''\ _{l,r}$ stoichiometric coefficient for product i in reaction r

  $v'_{j,r}$ rate exponent for reactant species j in reaction r

  $v''_{j,r}$ rate exponent for product species j in reaction r

  Because we are using the laminar finite-rate we have to enter the following parameters for the Arrhenius rate:

Pre-Exponential Factor :

$$k_{f,r} = A_r T^{\beta_r} e^{-E_r/RT} \tag{3.4}$$

Activation Energy the constant $E_{r,f}$ in the precedent equation

Temperature Exponent the value for the constant β_r in the Arrhenius equation

Third-Body Efficiencies the values for $\gamma_{j,r}$ in following Equation

$$\Gamma = \sum_{j}^{N} \gamma_{j,r} C_j \tag{3.5}$$

3.4.2.3.3 Boundary conditions specifications :

Specifying boundary conditions accurately is crucial for obtaining reliable results in ANSYS Fluent simulations involving species reactions and transport. Here is a detailed guide on how to set up various boundary conditions for such simulations :

Table 3.2 Configuration of boundary conditions :

Flow inlet	**Pressure far field**	**Temperature ; 293 k** **Gauge pressure ; 664Pa** **Mass fraction of species N2 and O2 ; 0.767 and 0.233**
Body	**Wall**	**Temperature : 1000k** **No slip condition**
Axis symmetry	**Axis**	**None**
Flow outlet	**Pressure outlet**	**None**

Fluent performs all its calculations using gauge pressure to avoid numerical errors during computations. The relationship between absolute pressure and gauge pressure is given by:

$$P_{abs} = P_{0p} + P_{\text{Gauge}} \tag{3.1}$$

By default, Fluent uses the atmospheric pressure value as the operating pressure. In our case study, since we are operating at relatively low pressures, this operating pressure is set to zero.

3.4.2.4 Solution:

Figure 3.17 - The Solution dialog box

3.4.2.4.1 Choice of the formulation algorithm:

The "Solution Methods" task page provides options to customize various parameters for your calculations.

3.4.2.4.1.1 Choice of the formulation algorithm:

Implicit methods compute unknown values using equations that incorporate both current and neighboring cell values, resulting in a system where each unknown appears in multiple equations solved simultaneously. This approach is stable for stiff problems and offers high accuracy per iteration but is computationally intensive due to solving multiple equations concurrently.

Conversely, explicit methods compute unknown values using relations that involve only current cell values, leading to a system where each unknown appears in a single equation solved sequentially. This method is computationally efficient per iteration but may require smaller time steps for stability in complex or rapidly changing scenarios.

In the context of density-based solvers, choosing the implicit option results in a system of linear equations for each cell, where equations are implicitly linearized across all dependent variables simultaneously. The explicit option similarly results in a system of equations per cell but linearizes equations explicitly, updating all dependent variables concurrently.

Regarding convective flux types like Roe-FDS and AUSM, they provide different methods for calculating convective fluxes in CFD simulations, each with its strengths in accuracy and stability depending on the flow conditions and numerical requirements.

3.4.2.4.1.2 The choice of the spatial discretization scheme :

3.4.2.4.1.2.1 Choice of Gradient method :

Selecting the method to compute gradients is crucial for accurately constructing scalar values at cell faces, calculating secondary diffusion terms, and deriving velocity derivatives. In our investigation, we adopt the Least-Squares Cell-Based approach for gradient computation. This method enhances accuracy, reduces artificial diffusion, and optimizes computational efficiency compared to alternative techniques.

3.4.2.4.1.2.2 The choice of the precision of the diagrams used :

When first-order accuracy is desired, quantities at cell faces are determined by assuming that the cell centre values of any field variable represent a cell-average value and hold throughout the entire cell; the face quantities are identical to the cell quantities. While, when second-order accuracy is desired, quantities at cell faces are computed using a multidimensional linear reconstruction approach. In this approach, higher-order accuracy is achieved at cell faces through a Taylor series expansion of the cell-cantered solution about the cell centroid.[26]

First-order discretization suffices when flow aligns with the grid; second-order gives better accuracy for non-aligned flows and reduces numerical diffusion in complex scenarios. Starting with second-order from the outset is often feasible, though beginning with first-order and transitioning can optimize results in some cases. Generally, first-order schemes offer faster convergence but less accuracy, particularly noticeable on triangular or tetrahedral grids.

3.4.2.4.2 Solution Controls : The Solution Controls task page allows adjustment of critical solution parameters. The Courant Number governs the time step factor in density-based solvers. Default under-relaxation factors are generally suitable but may need reduction for highly nonlinear issues like turbulence. Only modify under-relaxation factors if residuals rise persistently after initial iterations; in such cases, adjusting factors to approximately 0.2, 0.5, 0.5, and 0.5 can stabilize convergence.

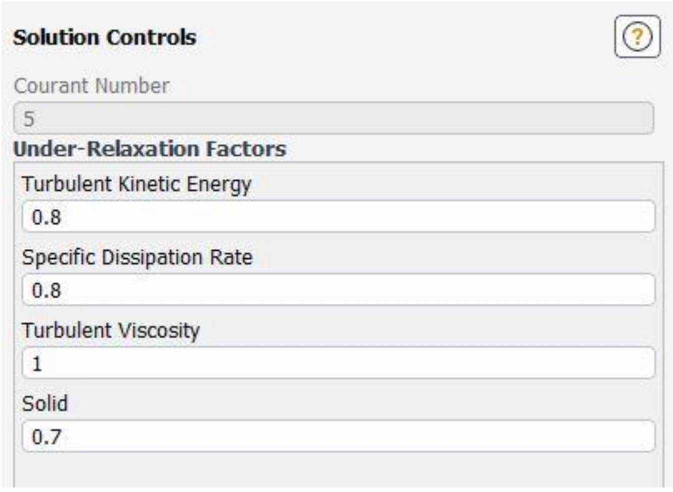

Figure 3.18: Solution Controls.

3.4.2.4.2.1 Solution limits :

In ANSYS FLUENT, limits are applied to pressure, static temperature, and turbulence quantities to prevent them from reaching extreme values like zero, negative, or excessively large values during calculations. These limits ensure numerical stability and prevent unrealistic physical conditions. Typically, the default solution limits are adequate and do not require adjustment. If warnings indicate that variables are repeatedly resetting to these limits, verify the problem setup including dimensions, boundary conditions, and material properties for accuracy. Only in rare instances, such as when expecting temperatures below a minimum threshold, should solution limits be adjusted to accommodate specific requirements.

3.4.2.4.3 Solution initialization :

Before starting our CFD simulation, we must provide ANSYS Fluent with an initial boundary condition of the solution flow.

```
  iter        scalar-0

  1         1.000000e+00
  2         3.924794e-06
  3         2.645149e-07
  4         2.219923e-08
  5         1.658714e-09
  6         1.514969e-10
  7         1.173818e-11
  8         1.119240e-12
  9         8.825452e-14
  10        8.613204e-15

Hybrid initialization is done.
```

Figure 3.19 : solution initialization

the Fluent solver proceeds by successive iterations to solve the matrix system obtained by discretization of the equations by a finite volume method. The iteration procedure requires that all the variables are initialized before the start of the calculation. An initialization improves the stability and the speed of convergence. In some cases, a correct initial solution is necessary [32].

For our calculation We set a velocity field equal to the entry velocity in the whole domain as the starting point of the iterations. The solver starts from the initial solution and due to an iterative algorithm of resolution of the matrix system obtained by discretization, will perform iterations. If all goes well, each iteration must modify the current solution to replace it with a solution closer to the exact solution sought. With each iteration and for each equations an error, called residue, is calculated compared to an exact solution of the system. A calculation diverges if the residuals increase during iterations.

3.4.2.4.4 Calculation control :

he Run Calculation task page allow us to start the solver iterations Number of Iterations

• for steady flow calculations: sets the number of iterations to be performed.

• For unsteady calculations: using the explicit unsteady formulation, this will specify the number of time steps, since each iteration will be a time step.he Run Calculation task page allow us to start the solver iterations Number of Iterations

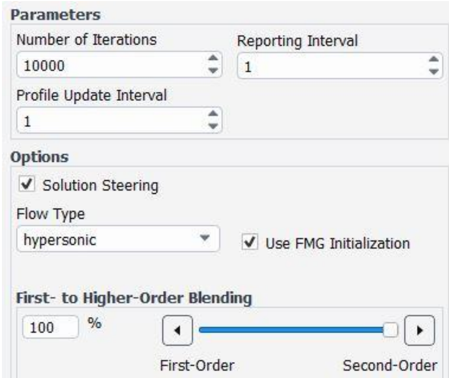

Figure 3.20:Run calculation

- for steady flow calculations: sets the number of iterations to be performed.
- For unsteady calculations: using the explicit unsteady formulation, this will specify the number of time steps, since each iteration will be a time step.

Convergence :

- ✓ Upon convergence, all discretized conservation equations (momentum, energy, etc.) in each cell conform to a specified tolerance, and the solution remains unchanged over time. Convergence monitoring is achieved through residuals. Typically, a decrease in residual magnitude by approximately 10^{-3} indicates at least qualitative convergence, establishing the primary flow characteristics [32].
- ✓ Residuals are computed from corrections in problem variables between the current and previous iterations. In most cases, Fluent's default convergence criterion, "residual," suffices. Convergence is achieved when residuals reach 10^{-3}
- ✓ However, in some cases, calculations may require pushing the threshold to 10^{-6} 10^{-4} There is no universal rule; adjustments depend on specific simulation requirements [32]

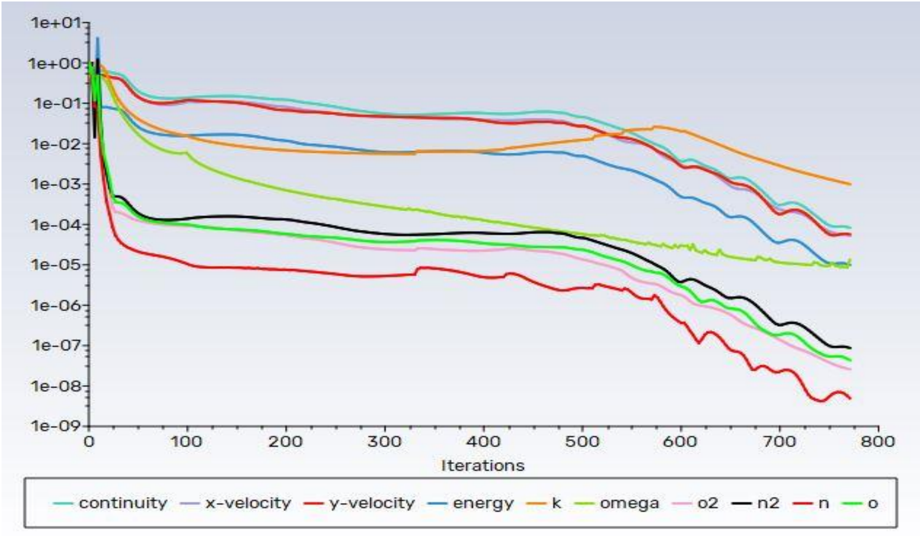

Figure 3.24 : The evolution of the residuals for the initial mesh.

3.4.3 Grid independency study :

Also known as a mesh convergence study, is a crucial step in our simulation to ensure that the results are independent of the mesh size used in the simulation. In ANSYS, this process involves running simulations with progressively finer meshes and comparing the outcomes to determine if further refinement has a negligible impact on the results.

- ✓ This study helps in identifying the optimal mesh that balances computational efficiency and accuracy. During the grid independence study, key parameters such as in our case temperature distributions are monitored across different mesh resolutions.
- ✓ The objective is to reach a point where changes in these parameters fall below a predetermined threshold, indicating that the solution is convergent and not significantly influenced by the mesh. Conducting a grid independence study ensures the reliability and robustness of our simulation results.
- ✓ **3.4.3.1.1 Lob Sphere Grid independency study :**

We observe that from adapt 3 onwards, the results become mesh-independent, as no temperature variation is detected during further refinements.

- ✓ from adapt 3 with a temperature of 9074K to adapt 4 with temperature 9083K so we can consider that the “adapted 3 mesh” is the optimum mesh

Table 3.3 Lob sphere Grid independency study

Adaptaion	initial	Adaptation1	Adaptation2	Adaptation3	Adaptation 4
Cells	6004	7980	12996	48278	**84304**
Elements	5625	7800	36200	44838	**82000**
T(k)	5434 k	7390k	9023k	9074K	9083K

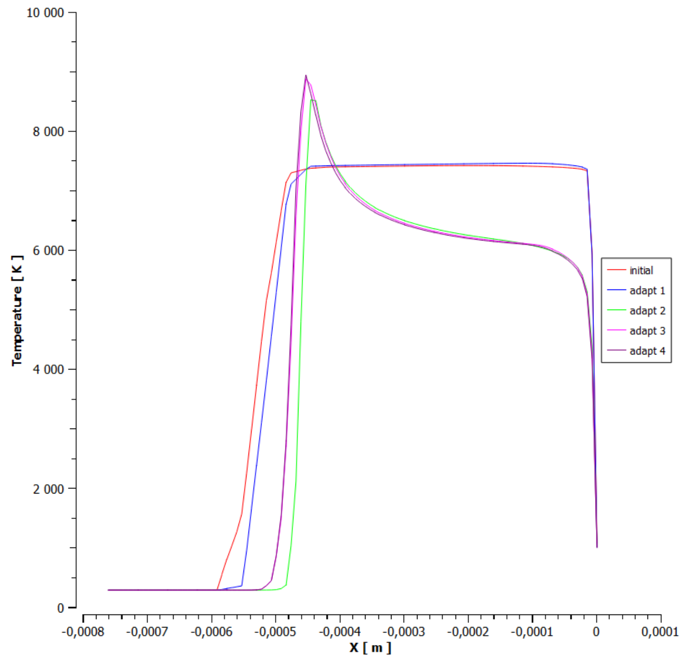

Figure 3.22 : Lob sphere grid independency

3.4.3.2 Delta profile grid independency study :

We observe that from adapt 3 onwards, the results become mesh-independent, as no temperature variation is detected during further refinements.

- ✓ from adapt 3 with a temperature of 7664 k to adapt 4 with temperature 7714 k so we can consider that the “adapted 3 mesh” is the optimum mesh.

Table 3.4 Delta Profile Grid independency study

Adaptaion	Initial	Adaptaion1	Adaptaion2	Adaptaion3	Adaptaion4
Cells	18866	41226	360846	397558	643648
Elements	18550	40725	119720	131912	213692
T(k)	5749 k	6205 k	7522 k	7664 k	7714 k

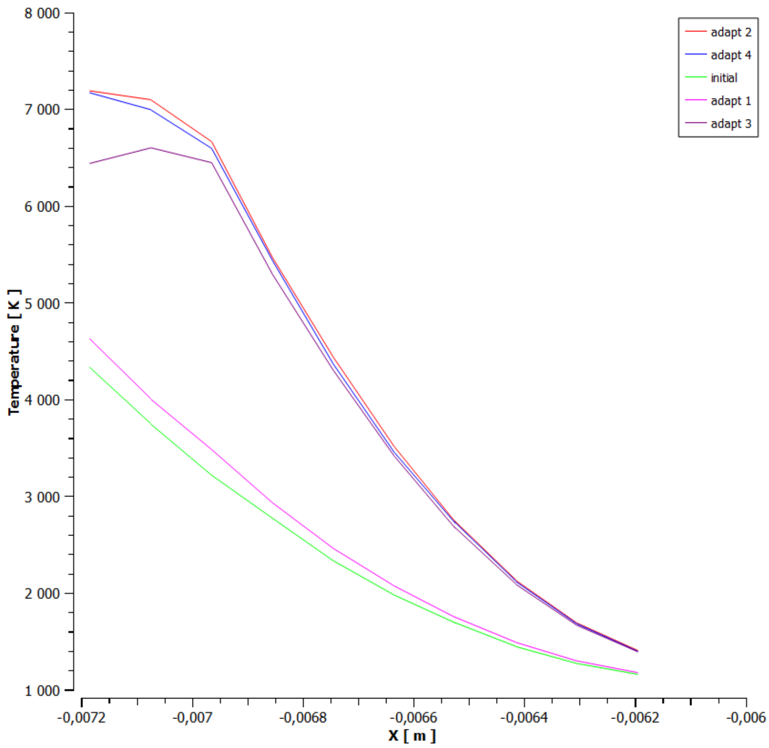

Figure 3.23 : Delta profile grid independency.

Chapter 4
Results And Discussions

4.1 Introduction :

Re-entry mission requirements play a crucial role in shaping vehicle design. Key factors such as deceleration, thermal management, and precision must be carefully balanced, as they are heavily influenced by the design choices.

Our task is finding an optimal balance between these trajectory parameters and the vehicle's structural and material design to fulfill mission objectives. Furthermore, the impact of radiation during re-entry must be addressed to ensure the protection of both the payload and onboard systems.

By utilizing ANSYS Fluent simulations, we approach these challenges from two broad perspectives, striving to harmonize all the conflicting demands of the mission.

Our study consists of :

In this chapter, we present:

- The Lobb sphere blunted nose, used to investigate the thermochemical nonequilibrium effects in re-entry hypersonic flow, including the impact of radiation.
- The delta profile, employed to examine trajectory design, with an added focus on radiation effects in the analysis.

4.1.1 Results Validation :

we compare our findings and results with those from previous studie to ensure the validity of our numerical results and to account for potential errors in the computational code Our results align closely with those obtained by Tristan, confirming the accuracy of our calculations .

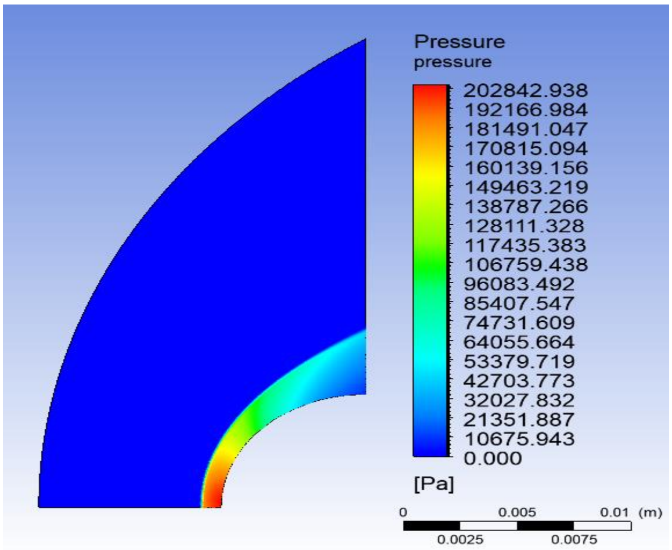

Figure 4.1 : Pressure field

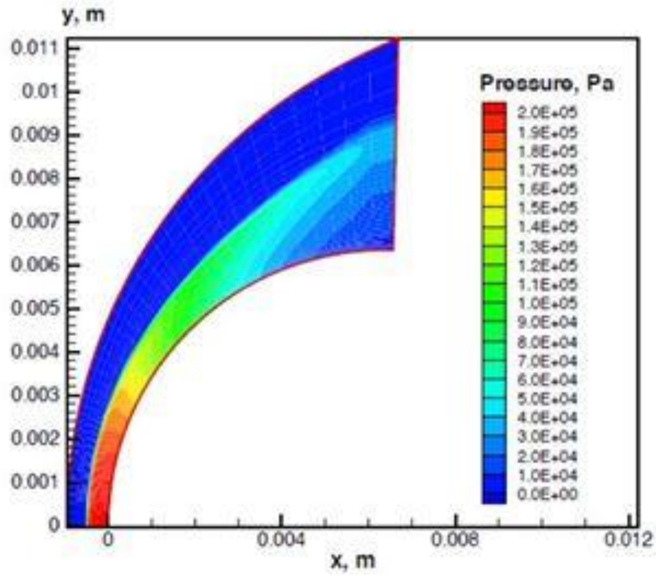

Figure 4.2 : Pressure field [29]

comparing our results in figure (4.1) with that of Tristan in figure (4.2), one can notice an excellent similarity with a slight error of 4.95%. between the two results for the different isobar zones in the relaxation zone.

4.2 Thermochemical nonequilibrium flow study :

4.2.1 Change in flow temperature after shock :

The shock wave is a mathematical discontinuity with a thickness of just a few microns. Over this very short distance, the flow particles experience intense compression, causing a significant portion of their kinetic energy to be transferred to them. This energy transfer results in a sudden temperature rise, reaching approximately 10,000 K from an initial upstream temperature of 293 K. This temperature increase is accompanied by a substantial pressure surge, around 2×10^5 Pa, leading to an extremely strong deceleration of the flow. Consequently, the flow transitions to subsonic speeds, with the Mach number dropping below one.

The maximum temperature behind the shock decreases until it reaches the equilibrium temperature of approximately 6000K in a distance of 0.50 mm. the appearance of the reactions of dissociation and exchange in the shock wave (chemical phenomena) which are endothermic phenomena, molecules absorb energy to recombinant or to break the links between them which cause a decrease in temperature to the wall by approximately 40% it's maximum value. [33].

These findings align well with the theory of normal shock waves and have been validated by the Rankine-Hugoniot jump equations.

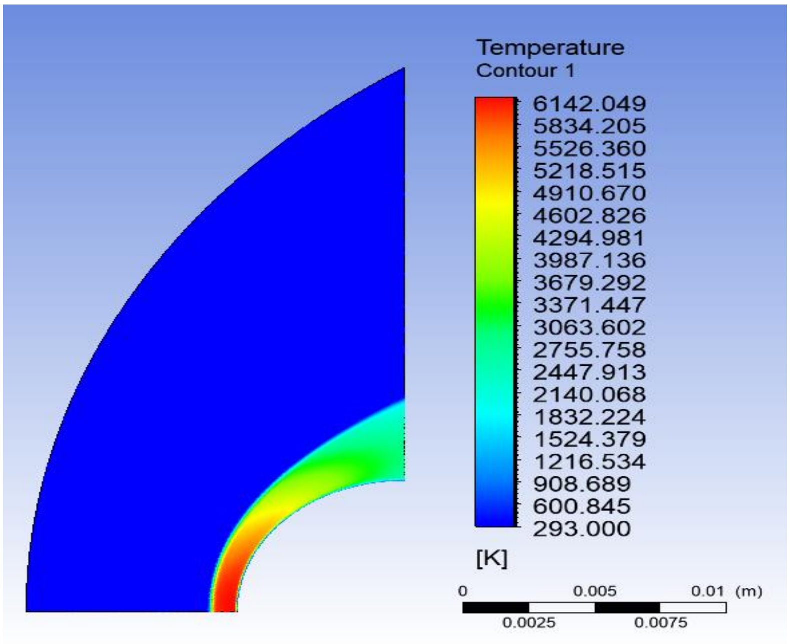

Figure 4.3 : Temperature variation across the shock wave in the non-equilibrium flow

4.2 Thermochemical nonequilibrium flow study

4.2.1 Simulation of the Non-Reactive Flow Around the Lobb Sphere:

Firstly, the simulation is conducted with a non-reactive flow, meaning no chemical reactions occur during this initial phase. Additionally, vibrational energy is not considered in this part of the simulation. This simplification allows for a clearer analysis of the basic flow characteristics without the added complexity of chemical reactions and vibrational energy effects.

In this initial setup, the simulation involves only two chemical species:

- Dinitrogen (N_2): This is the most abundant component, reflecting the major presence of nitrogen in the flow.
- Dioxygen (O_2): This is the secondary component, representing the oxygen present in the flow.

By starting with a non-reactive flow with these two species, the simulation provides a baseline understanding of the flow dynamics around the Lobb sphere without the influence of reactions or vibrational energy. This step is crucial for establishing initial conditions and understanding the fundamental behavior of the flow before introducing the complexities of reactive simulations and vibrational energy considerations..

4.2.1.1 Change in Mach number of flows after shock

An increase in the upstream Mach number results in a substantial temperature rise. This phenomenon occurs because the higher kinetic energy of the flow translates into increased thermal energy. As the Mach number increases, the flow's kinetic energy increases proportionally, leading to a more pronounced conversion into heat energy. Therefore, the temperature of the flow increases significantly with higher Mach numbers due to this intensified energy conversion process.

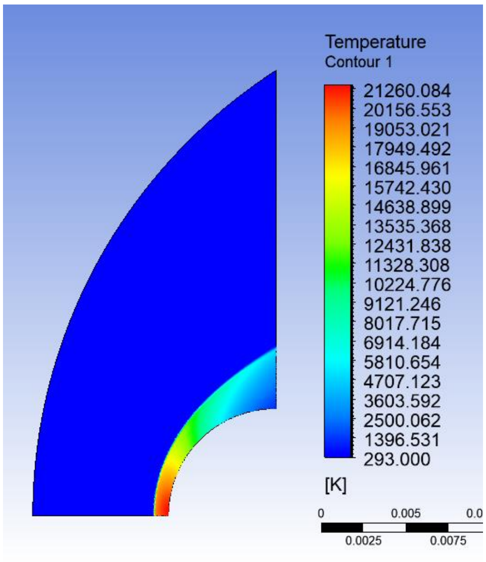

(A)

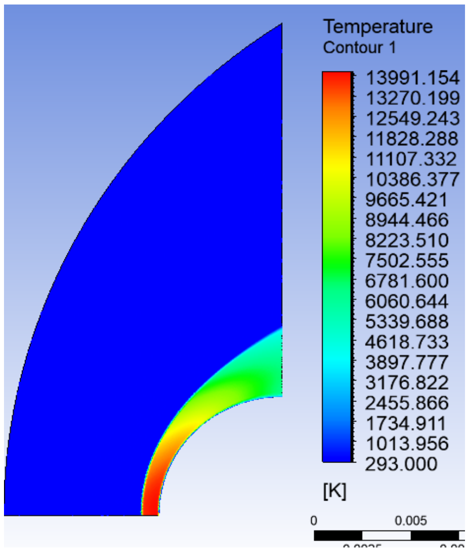

(B)

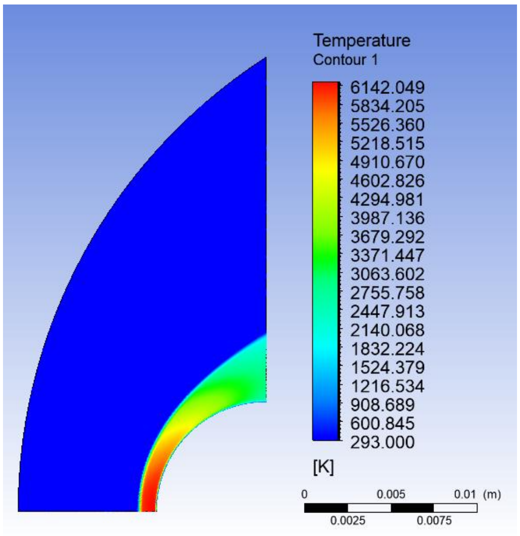

(C)

T=293 k

P = 664 Pa

$\rho = 7{,}896\ 10^{-3}\ kg/\ m^3$

(A) : M = 20

(B) M: = 15.35

(C) : M = 10

Figure 4.4 : Temperature Contour for Non-Reactive Flow in.

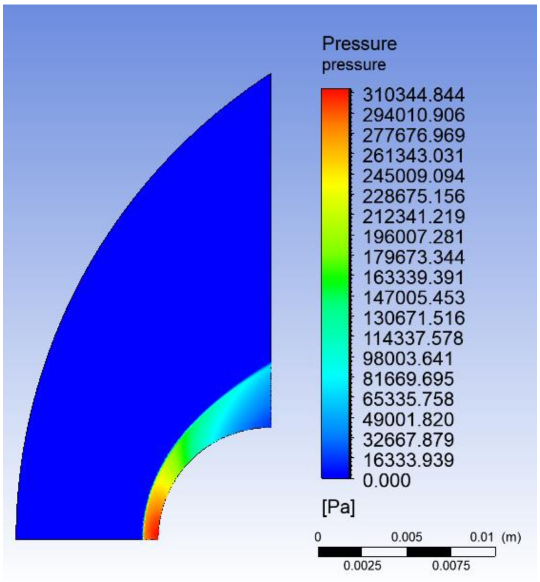

(A)

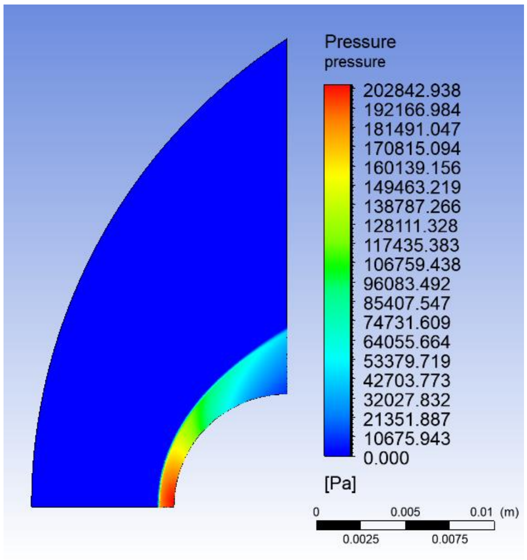

(B)

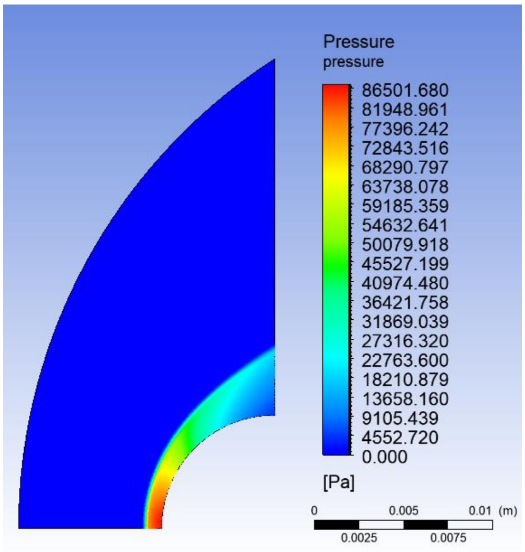

(C)

T=293 k

P = 664 Pa

$\rho = 7{,}896\ 10^{-3}\ kg/\ m^3$

(A) : M = 20

(B) M: = 15.35

(C) : M = 10

Figure 4.5 : Pressure Contour for Non-Reactive Flow

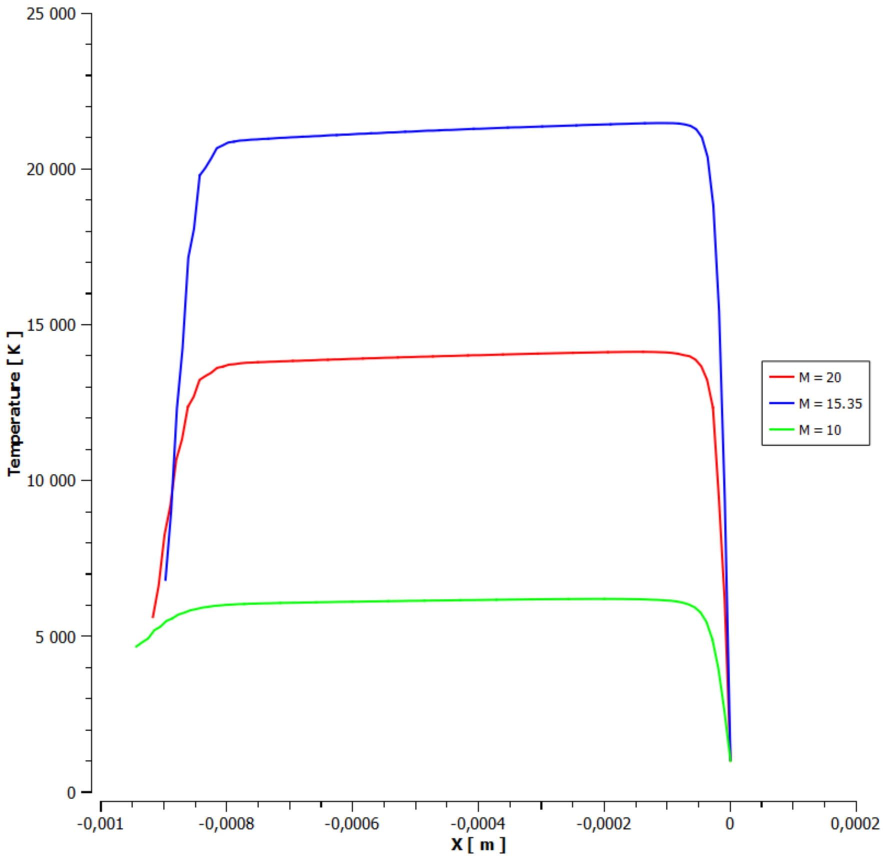

Figure 4.6 : influence of Mach number on the evolution of tempareure for a non reactif gas.

4.2.2 Reactive flow in thermochemical nonequilibrium around the Lobb sphere :

In our study , Our simulation accounts for five different chemical species, following a Zeldovich model with 5 reactions and 17 reactions.

We observe that an increase in the upstream Mach number leads to a significant rise in temperature within the relaxation zone. This is due to the substantial dissipation of the upstream flow's kinetic energy into thermal heat energy. As the Mach number increases, the kinetic energy of the flow intensifies, and when this energy is converted into heat, it results in a higher temperature.

Additionally, the distance between the shock wave and the wall is shorter when the flow is considered reactive. In a reactive flow, chemical reactions and energy exchanges occur, causing changes in flow properties that bring the shock wave closer to the surface.

Moreover, as the Mach number increases, the relaxation zone becomes narrower.

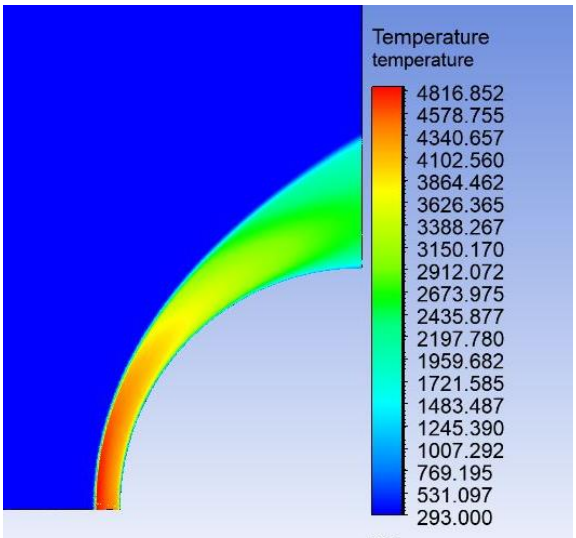

(A)

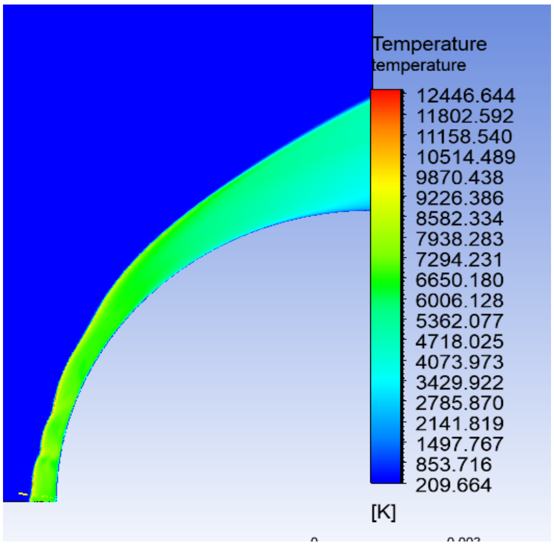

(B)

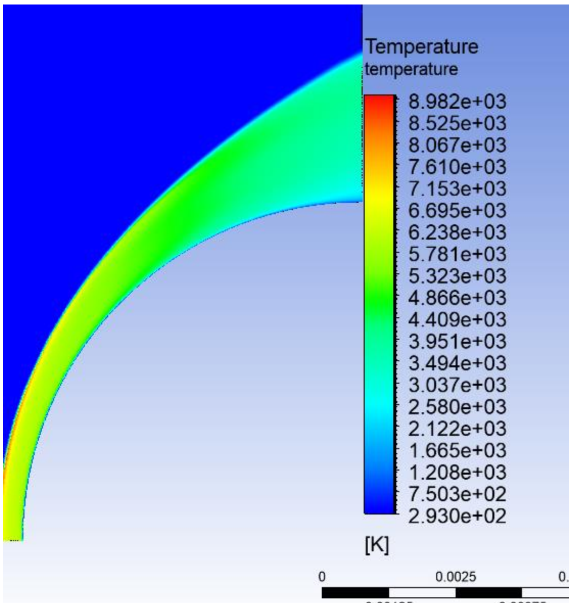

T = 293k ,

P = 664 Pa

$\rho = 7{,}896\ 10^{-3}\ kg/\ m^3$

(A) : M = 20

(B) M: = 15.35

(C) : M = 10

(C)

Figure 4.7 : Evolution of temperature in function of Mach number , Zeldovich 5 reactions Model .

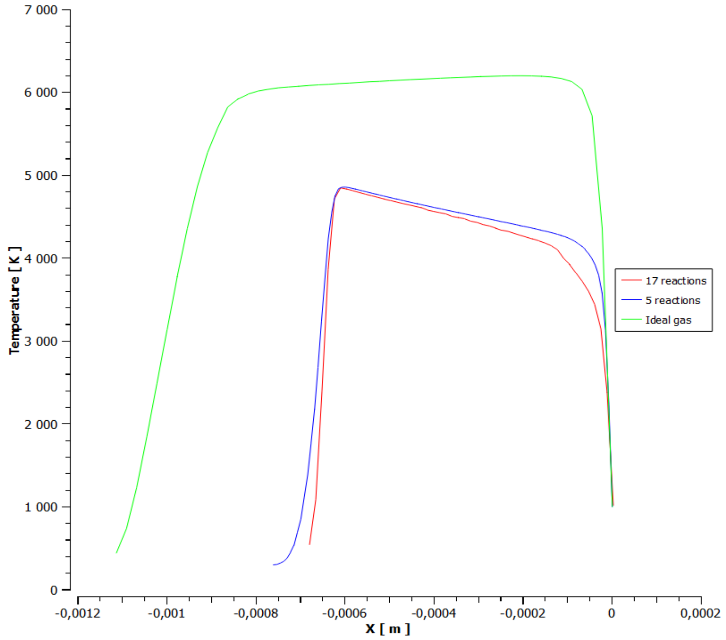

Figure 4.8 : Evolution of temperature in function of Mach number , Zeldovich 5 reactions Model for M = 10

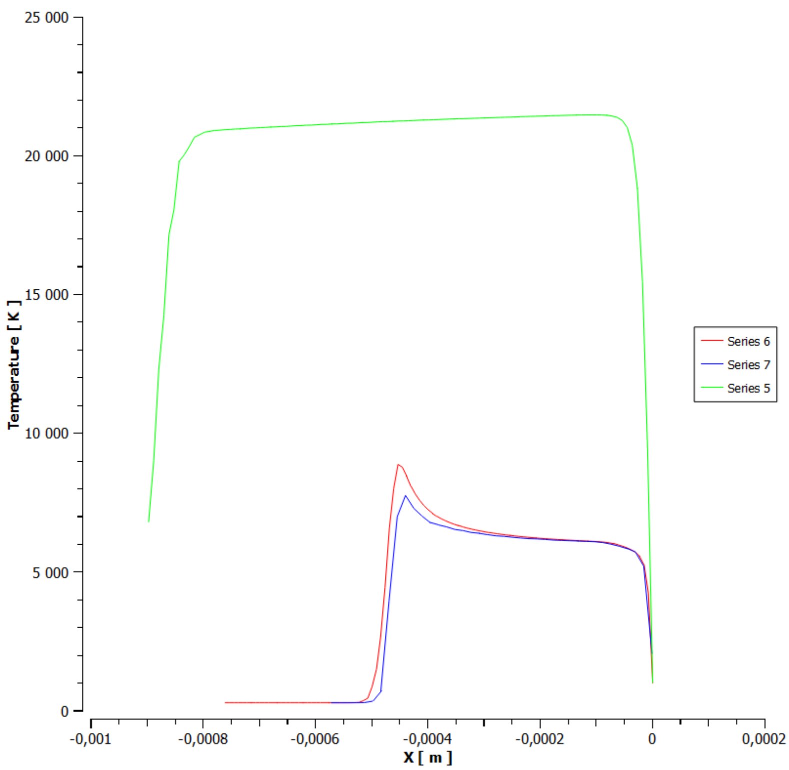

Figure 4.9 : Evolution of temperature in function of Mach number , Zeldovich 5 reactions Model for M = 15.35

4.2.2 Influence of the chemical Model on the temperature variation

As we know a catalyst accelerates the reaction by offering an alternative pathway with lower activation energy, resulting in a greater temperature decrease in the 17-reaction model, as illustrated in the figure.

The 17-reaction kinetic model reduces the maximum temperature by 11% compared to the 5-reaction kinetic model.

This reduction is due to the presence of a catalyst in the 17-reaction model, which increases the number of effective collisions at the same temperature.

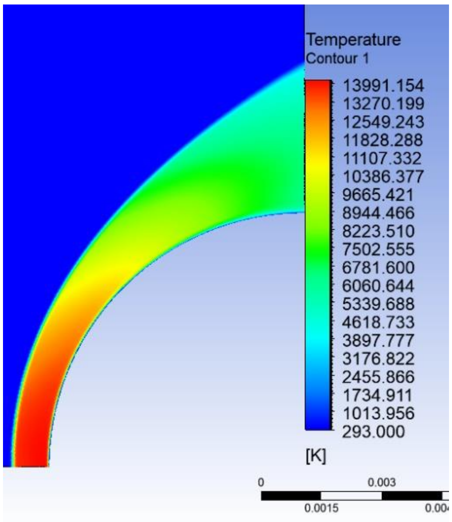

(A)

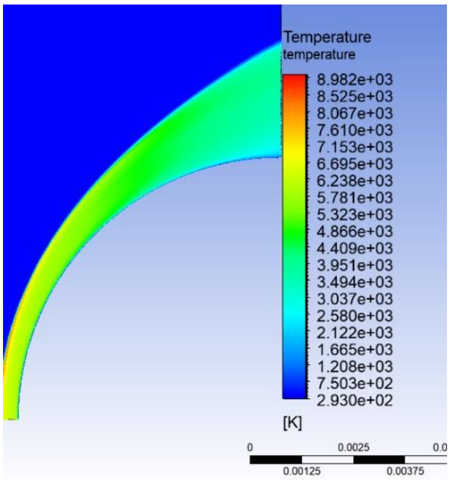

(B)

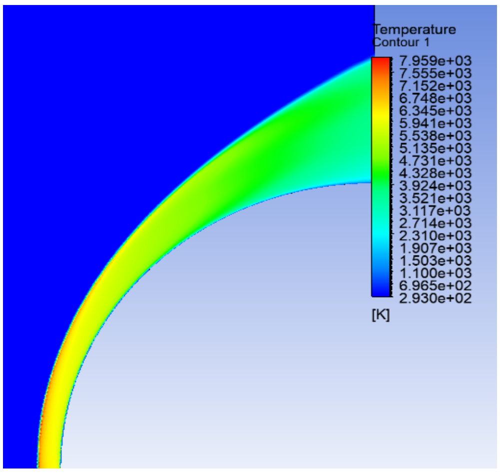

(C)

M = 15.35 , P =293 k

P = 664 Pa

$\rho = 7{,}896\ 10^{-3}$

A : Ideal gas

B : 5 reactions Model

C : 17 reactions Model

Figure 4.10 : Evolution of temperature in function of Mach number , Zeldovich 5 reactions Model for M = 15.35

4.2.3 Mass fractions of species :

The stagnation line is the streamline that comes to a stop at the surface of a bluff body due to the opposing flow. the mass fractions of all the species vary along the stagnation line. This is because the composition of the gas mixture is changing as it interacts with the surface of the bluff body. The specific changes will depend on the type of flow, the gas mixture, and the surface of the bluff (lob sphere) body.

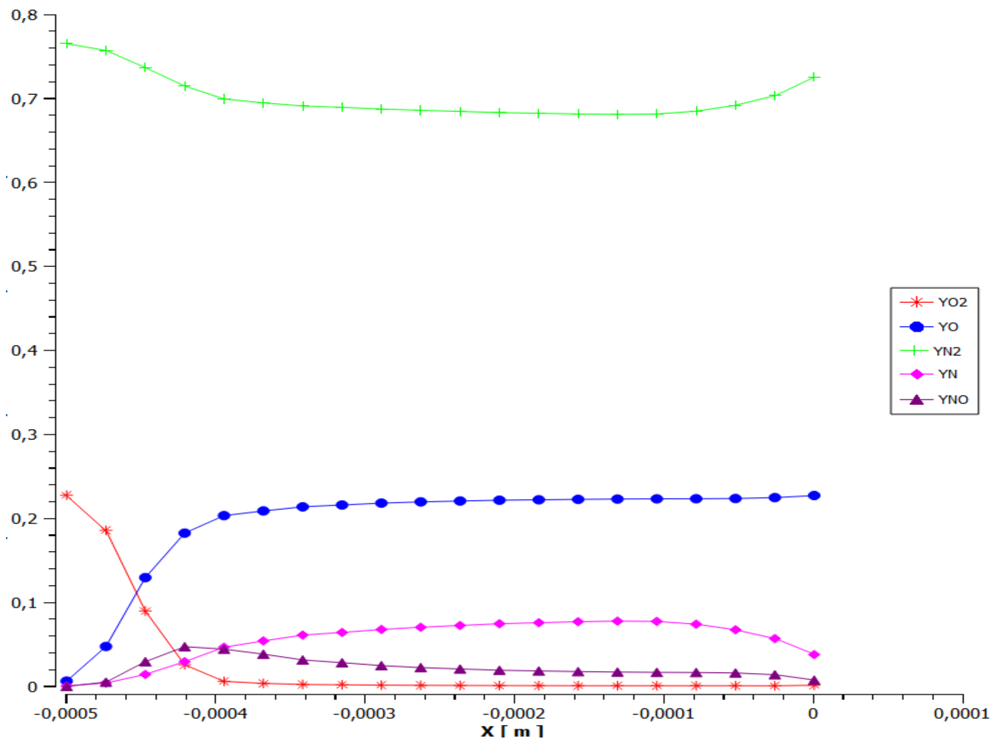

Figure 4.11: Ourvresults for Mass fractions of species along the stagnation line for M=15.35

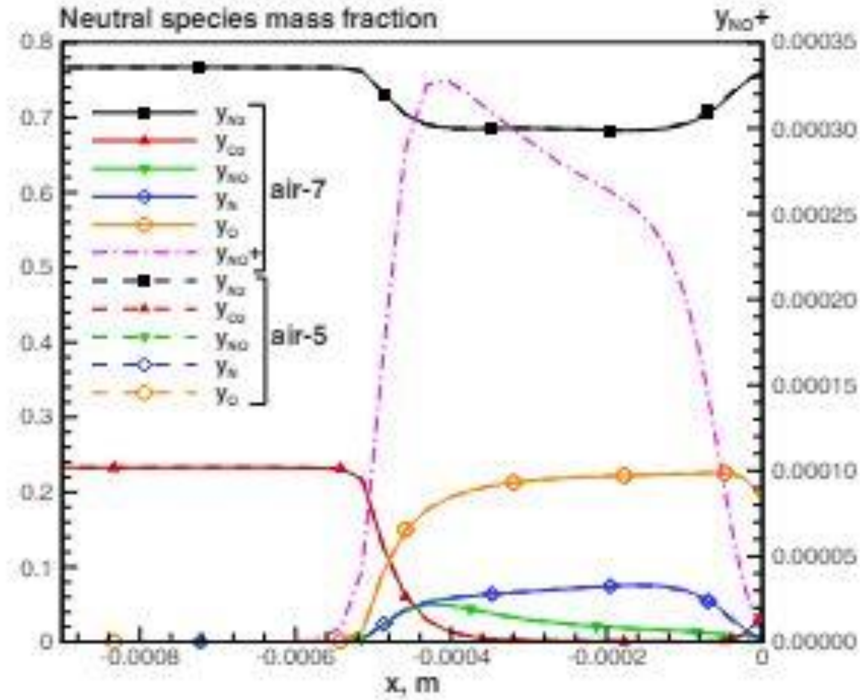

Figure 4-12: Tristan results for Mass fractions of species along the stagnation line for M=15.35

The characteristic temperature of a molecule is the temperature at which significant molecular dissociation begins to occur. For oxygen (O2) molecules, this characteristic temperature is approximately half that of nitrogen (N2) molecules. This means that oxygen molecules require less energy to start dissociating compared to nitrogen molecules.

In a high-energy environment like our study environement :

- Oxygen molecules (O2) have a lower threshold for dissociation due to their lower characteristic temperature. As a result, a higher percentage of oxygen molecules will dissociate because it takes less energy for them to break apart into individual atoms.

- Nitrogen molecules (N2), on the other hand, have a higher characteristic temperature, meaning they need more energy to start dissociating. Therefore, fewer nitrogen molecules will dissociate under the same conditions because reaching the necessary energy level for their dissociation is harder.

- As stated, more than 95% of oxygen molecules dissociate, whereas less than 10% of nitrogen molecules do, indicating that oxygen dissociates much more readily than nitrogen in the given conditions. This difference is primarily due to the lower energy

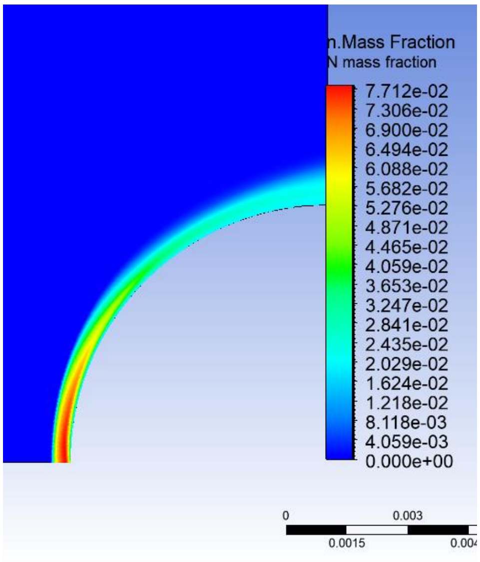

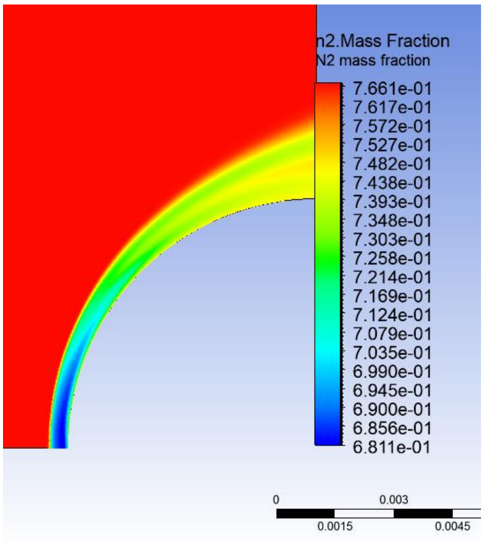

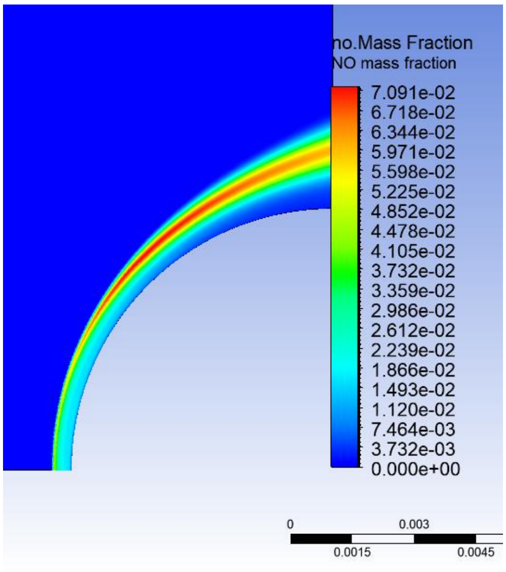

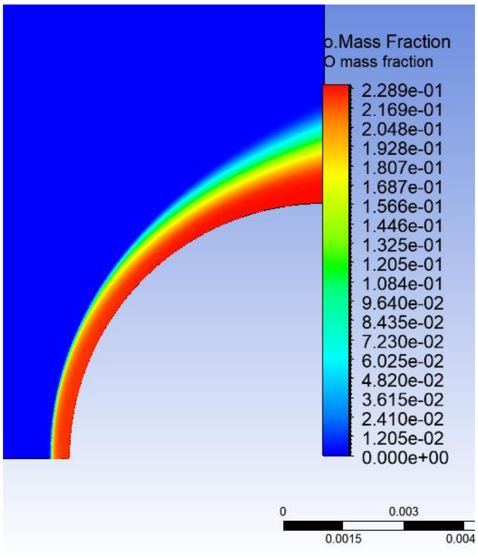

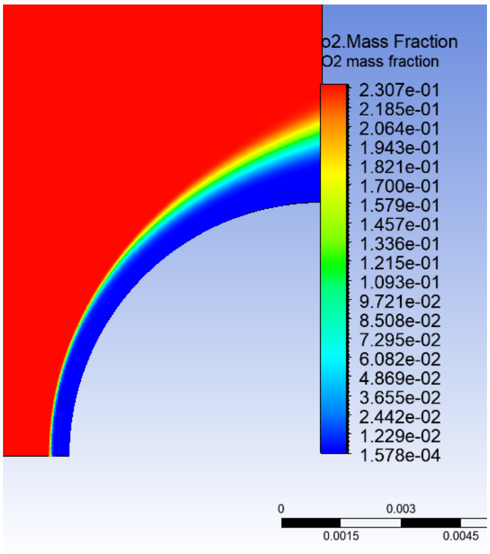

M = 15.35 ,

T =293 k

P = 664 Pa

$\rho = 7{,}896\ 10^{-3}$

Figure 4.13 : Evolution of species in relaxation zone according to 5 reactions chemical kinetic model for M = 15.35

4.2.4.1 Radiation effect on temperature evolution :

When considering the temperature evolution of a bluff body during re-entry into the Earth's atmosphere, radiation plays a significant role. Let's break down the effects and compare the scenarios with and without radiation like illustrated in the next figure :

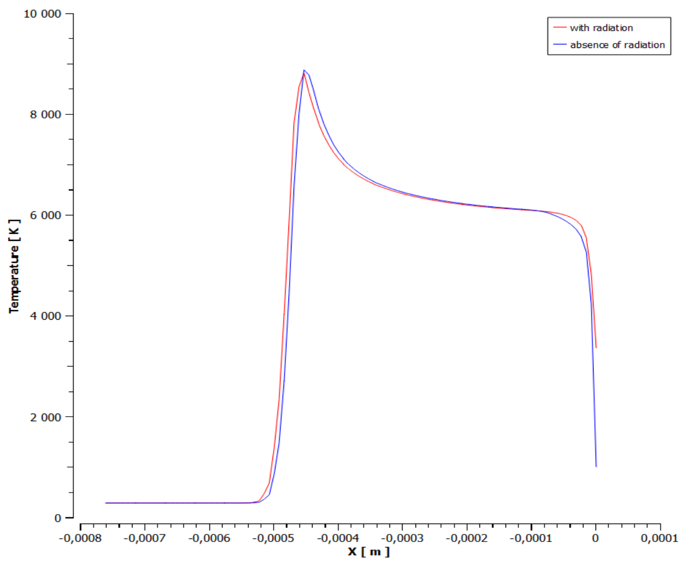

Figure 4.14 : disturbution of temperature along the stagnation line with/without radiation effect for 5 reaction Model for M = 15.35

A bluff body, such as a spacecraft or missile, has a blunt shape that creates a high-pressure region at the front and low-pressure wake at the back during re-entry. This shape is efficient for managing high thermal and aerodynamic loads.

The primary mode of heat transfer to the bluff body during re-entry is convective heating from the hot gases in the boundary layer. As the high-speed re-entry compresses and heats the air, it leads to a significant convective heat flux to the body's surface. This causes the surface temperature to rise as the heat is conducted into the body As we notice a slight decrease in temperature in the presence of radiation effect for the body compared to the case where radiation effects are not considered.

From the previous figure The shock wave might form slightly closer to the body.

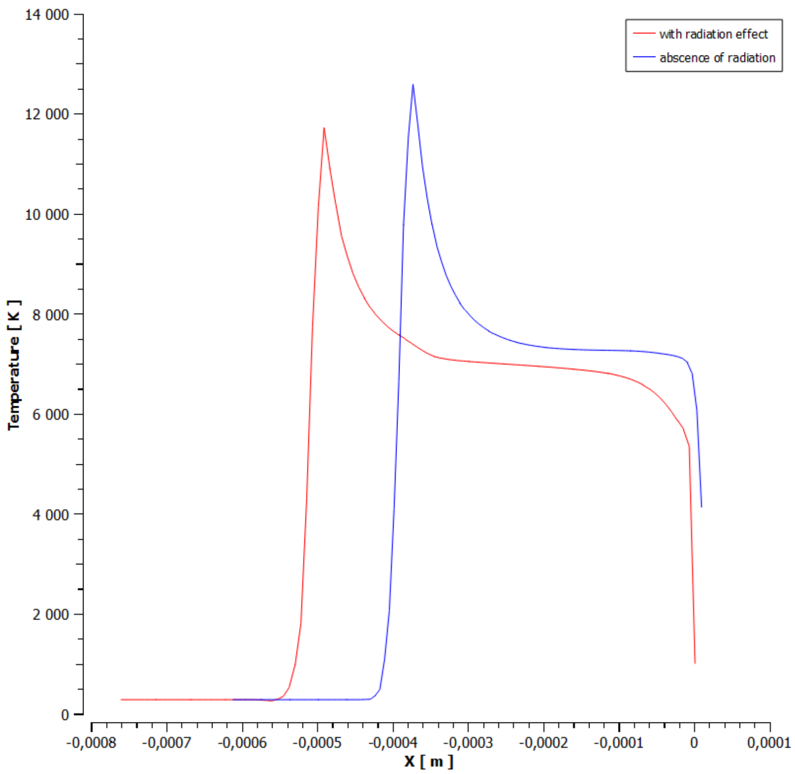

Figure 4.15 : disturbution of temperature along the stagnation line with/without radiation effect 5 reaction Model for M = 20

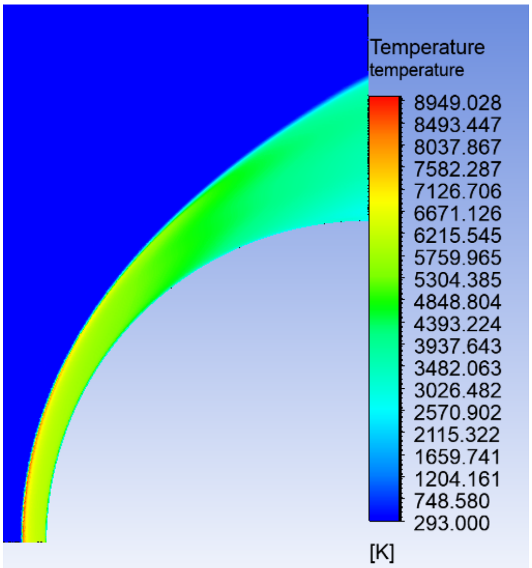

Fig A)

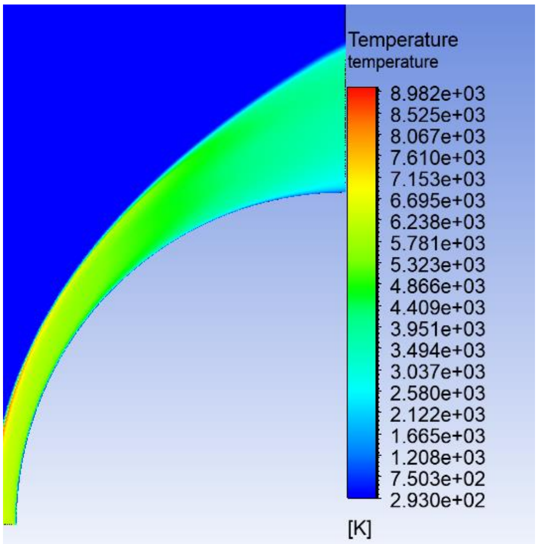

fig B)

Figure 4.16 : disturbution of temperature along the stagnation line with/without radiation effect 5 reaction Model for M = 15.35

Fig A) : with radiation	fig B) without radtion

The effect of Mach number Variation on radiation :

With increased radiative heating at higher Mach numbers, the surface temperature of the bluff body rises more rapidly compared to lower Mach numbers. This is because the body absorbs not only convective heat from the surrounding gases but also significant radiant heat from the shock layer.

The body reaches a new equilibrium temperature where the heat input from both convection and radiation equals the heat conducted into the body and radiated away from its surface. This equilibrium temperature is higher at higher Mach numbers due to the increased radiative heat flux.

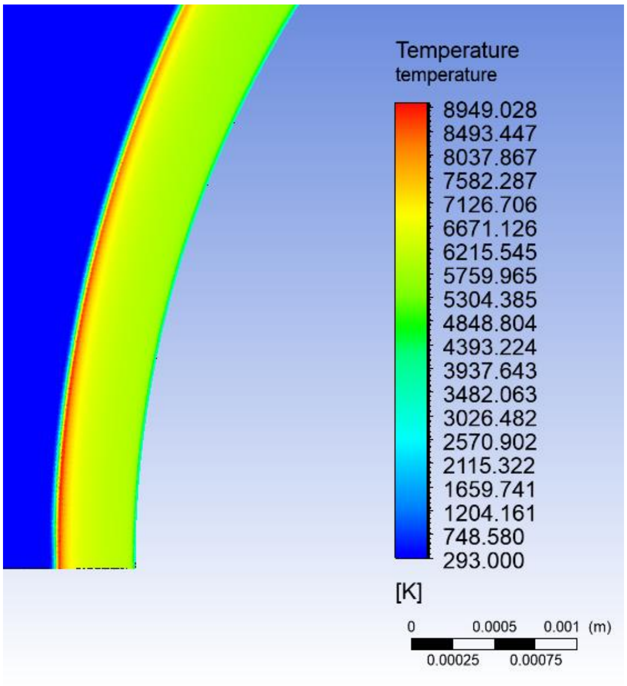

Fig A)

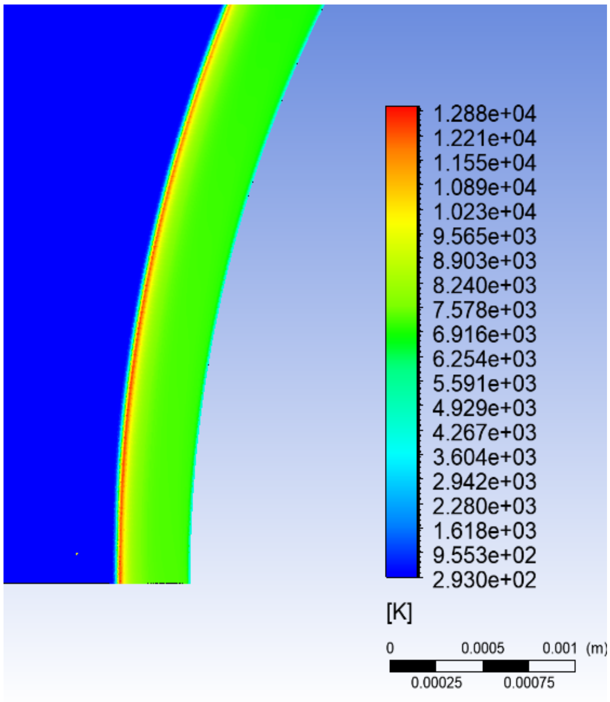

fig B)

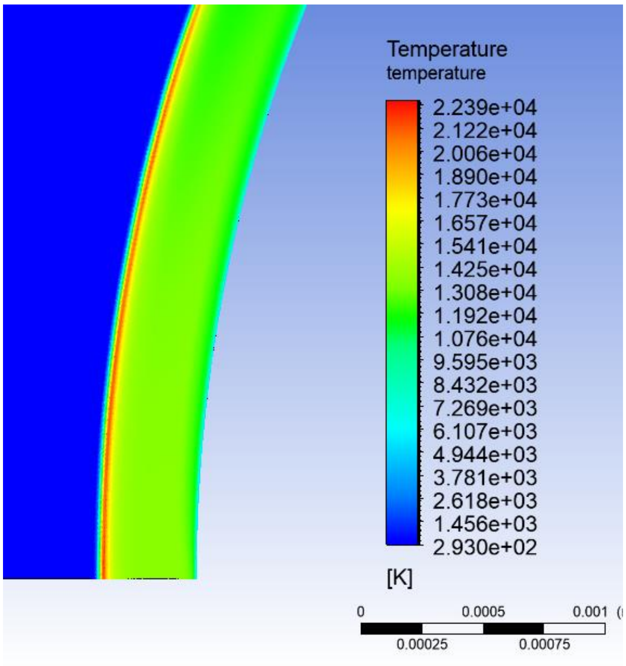

Fig C)

Fig A) : M = 15.35 fig B) M=20 fig C) M=30

Figure 4.17 : disturbution of temperature along the stagnation line with/without radiation effect 5 reaction Model for M = 15.35/ 20

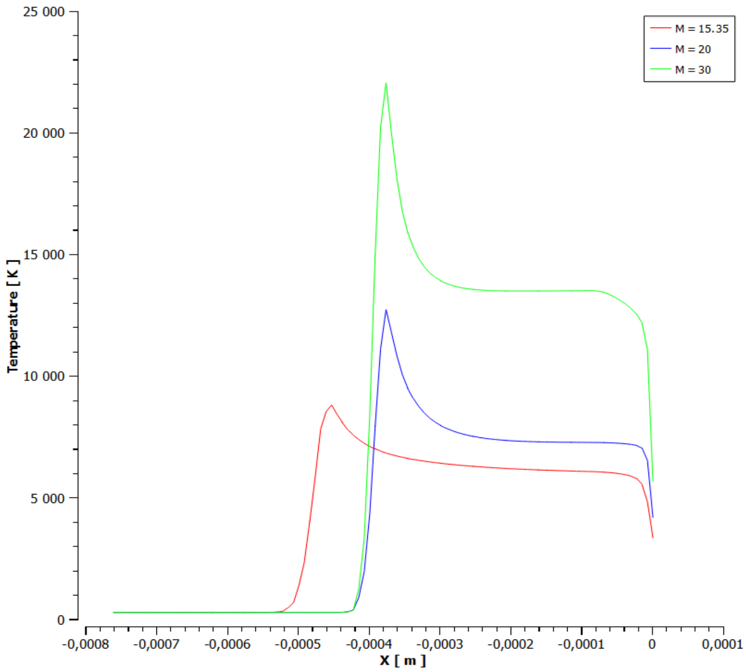

Figure 4.18 : evolution of temperature along the stagnation line with/without radiation effect 5 reaction Model for M = 15.35/20/30

As we can Observe from the previous figure at a Mach number of 30, the flow field reaches extremely high temperatures (up to 23,000 K). The shock wave forms closer to the body (shorter standoff distance) because the compression is more rapid.

At Mach numbers of 15 and 20, the shock standoff distance is longer compared to 30 Mach number.

The high temperature just after the shock results from this intense compression. Dissociation of molecules (N2 and O2) into atoms (N and O) is more prominent at higher Mach numbers because of the short reaction time. Recombination of atoms into molecules happens more at lower Mach numbers where the reaction time is longer. The relaxation zone, where the flow properties return to equilibrium, is shorter at higher Mach numbers.

4.3 Delta profile :

From our simulation re-entry vehicle, we can plot the wall temperature along the vehicle wall for various chemical models, re-entry velocities, flight path angles, and altitudes to study the trajectory design of the lifting body. This process involves creating a computational model to simulate the behavior and characteristics of the vehicle as it descends through the atmosphere. By graphically representing the temperature on the vehicle's surface, we can understand how different chemical reactions in the atmosphere affect the vehicle's thermal environment. The simulations also consider different re-entry velocities and flight path angles, as these factors influence the aerodynamic forces and heating rates experienced by the vehicle. Additionally, the altitude at different points during re-entry affects atmospheric density and pressure, further impacting the vehicle's performance. By analyzing the wall temperature under these various conditions, engineers can design an optimal trajectory that ensures the re-entry vehicle, particularly a lifting body, can safely and efficiently re-enter the atmosphere.

For high-speed re-entry conditions, the Stanton number at the stagnation point can be estimated using approximations developed in the late 1950s by Lees and Allen, and Eggers. These approximations are based on empirical and theoretical analyses of hypersonic flow heat transfer processes. The familiar form of this approximation, dependent on the free-stream Reynolds number scaled by the nose radius, is given by:

$$St_{HIGH\ SPEED} = \frac{h}{\rho_\infty\ cp\ v_\infty} \tag{4.1}$$

$$\mathrm{Re} = \frac{\rho u R}{\mu} \tag{4.2}$$

Once the Stanton number is known, the heat flux at the stagnation point can be estimated using the relationship:

$$q = \rho c_p u (T_\infty - T_w)\ St \tag{4.3}$$

Wall Temperature (T_w) :

Rearranging the heat flux equation, the wall temperature can be solved as:

$$T_w = T_\infty - \frac{q}{\rho c_p u St} \tag{4.4}$$

4.3.1 Results Validation :

.Density gradient in the y direction was used to describe a Schlieren photograph and reconfigured flow field as shown in figure 4.19

Fig (a) α = 0°

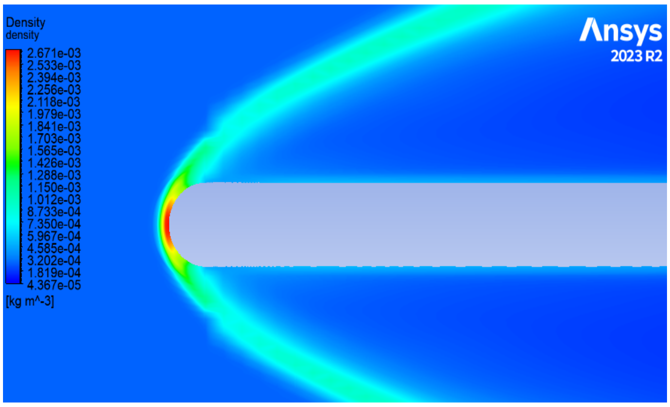

Fig. (B) α = 0°

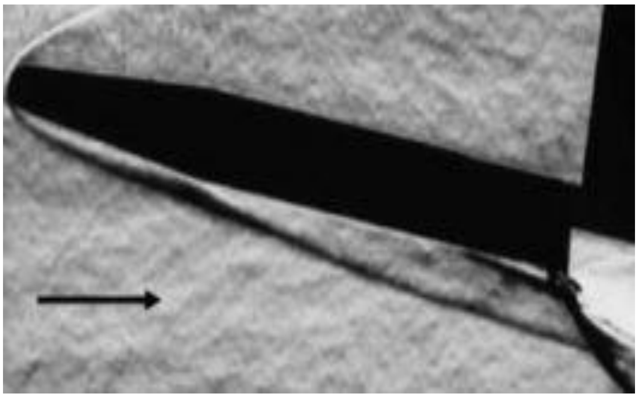

Fig (a) α = 20°

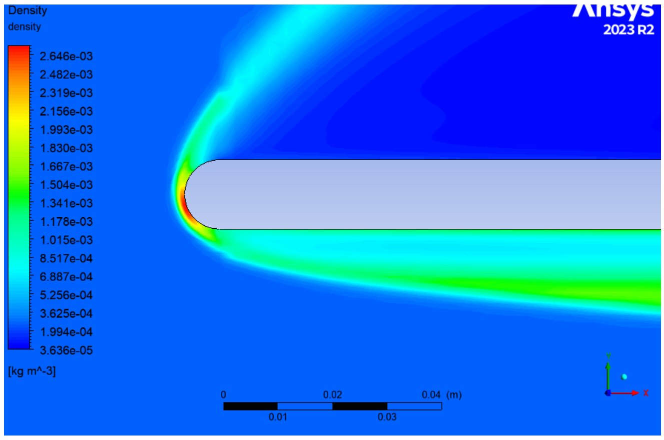

Fig(B)α = 20°

Figure 4.19 : Density gradient Fig (a) Schlieren experimental photograph, Fig(b) CFD simulation [29]

4.3.2 Chemical model effect :

In our study we focused on examining the impact of the chemical reaction model on the wall temperature of a re-entry vehicle.

As shown in figure , We observe that incorporating chemical reactions significantly reduces the maximum wall temperature. Specifically,

- the maximum temperature drops by 35%, from 12,000K under the perfect gas assumption to 7,800K when using a chemical model with 5 reactions (as shown in figure 4.20).

This reduction occurs because, in the post-shock region, more molecules dissociate. Dissociation requires energy to break molecular bonds, which absorbs heat from the surrounding environment. This process is endothermic, meaning it consumes energy and reduces the overall temperature.

The thermal loads on a material sample include the convective heat load from dissociation and the energy released by atom recombination at the surface. Despite the overall temperature reduction, the lower surface temperature increases convective heat transfer to the vehicle. This happens because a lower surface temperature results in a higher temperature gradient at the wall, which, according to Fourier's law, increases the rate of convective heat transfer.

This increase in heat transfer is particularly pronounced in a small region near the stagnation point, where the vehicle is directly exposed to the intense shock wave.

- In the 17-reactions case, the stagnation temperature decreases by approximately 1,000K compared to the 5-reactions and perfect gas cases (as shown in figure 4.19). Additionally, the pressure also decreases when moving from a perfect gas to a 17-reactions dissociated gas model (as shown in figure 4.21).

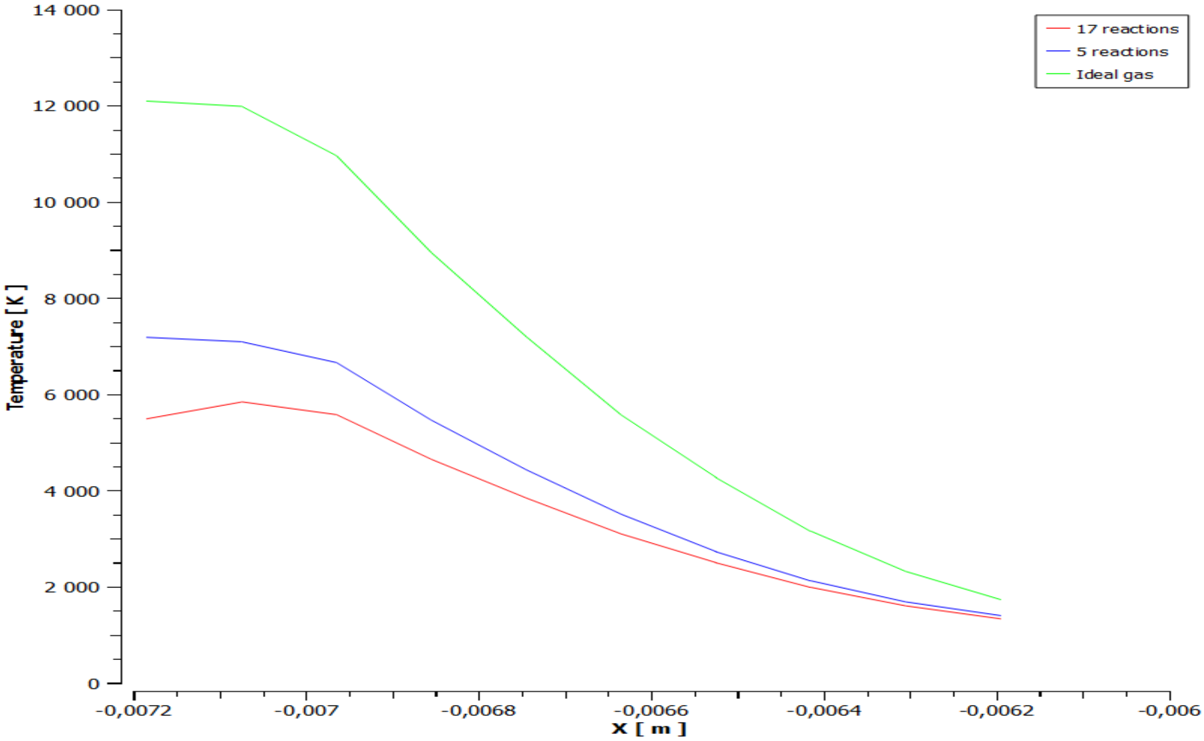

Figure 4.20: Wall temperature distribution along surface streamlines for M = 15.56 and α =0

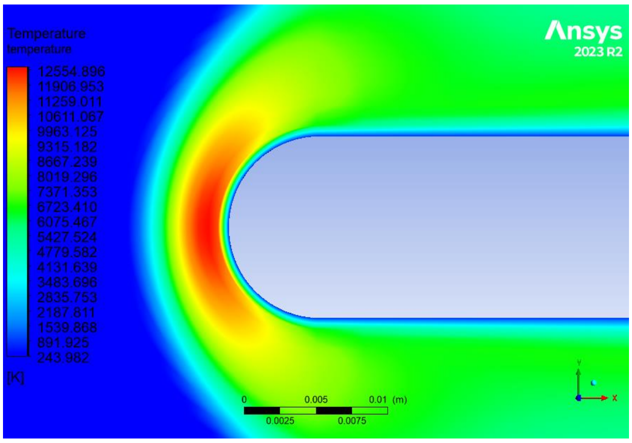

$Fig.\ A)$

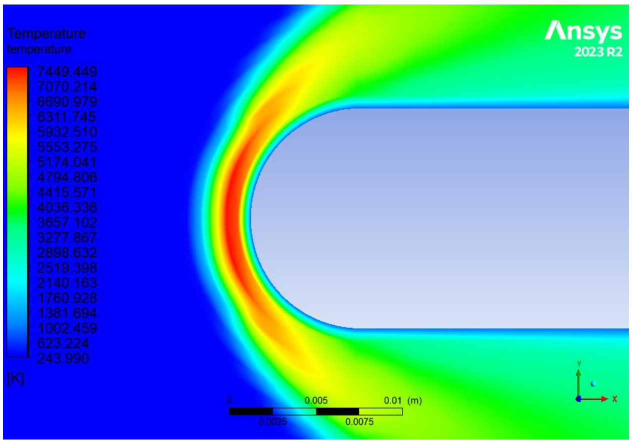

$Fig.\ B)$

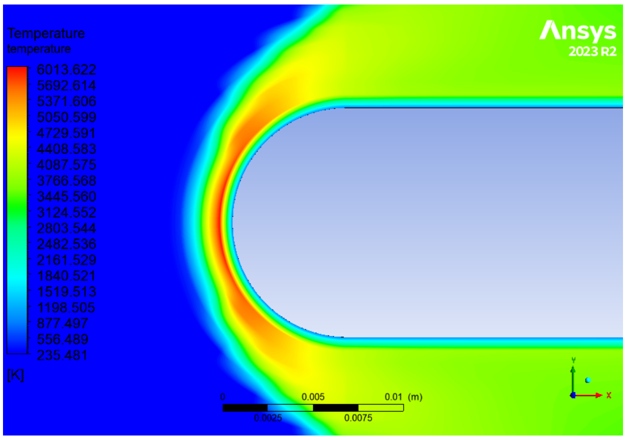

Fig C)

M=15.65, $H = 60.96\ Km$,

$T = 244.4\ k$, $\rho = 2.745\ 10{-}4\ kg$ $m3$ $P = 19.26\ Pa$, $\alpha = 0°$

$Fig.\ A)$ Perfect gas

$FigB)$ 5 $Reactions$

$Fig.\ C)$ 17 $Reaction$

Figure 4.21: Temperature field along surface streamline

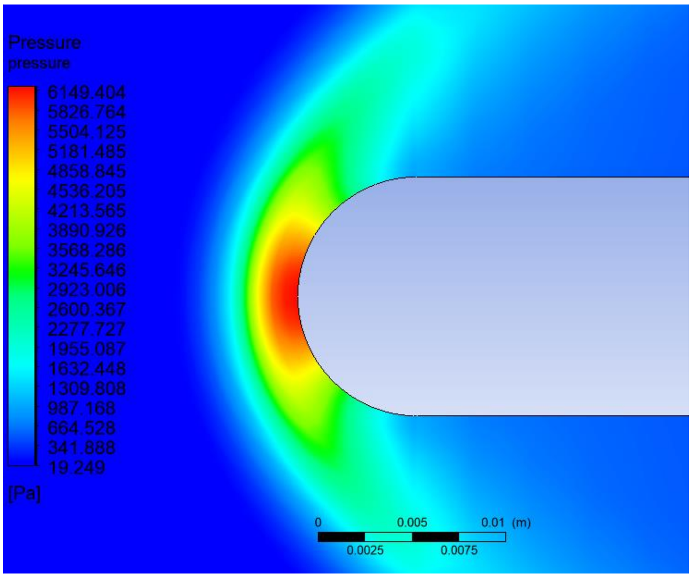

$Fig.\ A)$

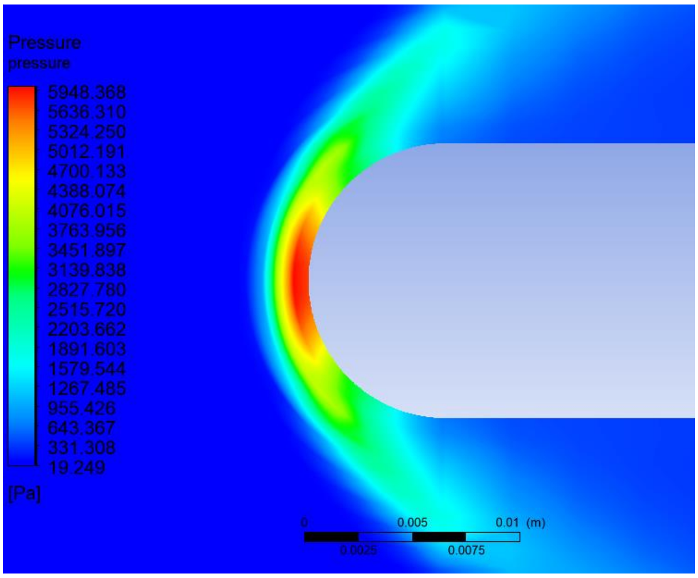

$Fig.\ B)$

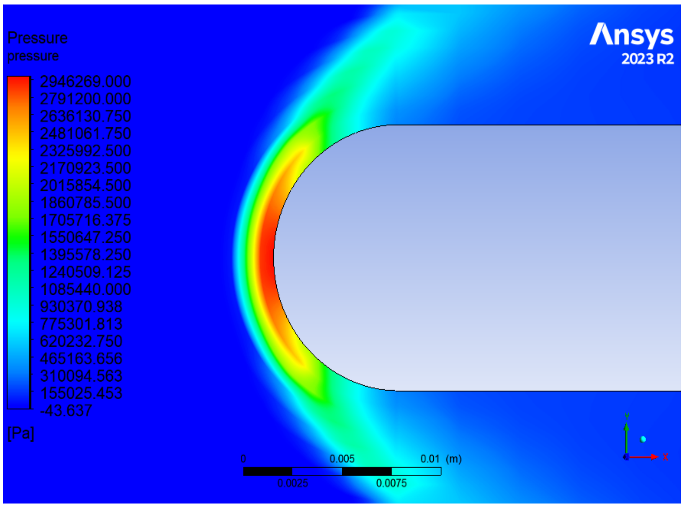

$Fig.\ C)$

M=15.65, H = 60.96 Km,

T = 244.4 k , ρ = 2.745 10−4 kg $m3$ P = 19.26 Pa , α = 0°

$Fig.\ A)$ Perfect gas Fig

$Fig.\ B)$ 5 $Reactions$

$Fig.\ C)$ 17 $Reaction$

Figure 4.22: Pressure field along surface streamline

4.3.2.1 High enthalpy flow:

Re entry Vehicules are exposed to extremely high levels of thermal energy as they pass through the Earth's atmosphere at high velocity. In this high enthalpy range, the behavior of gases deviates from the ideal gas laws, and real gas effects become significant.

To understand the decrease in temperature when accounting for real gas effects, we need to look at enthalpy, which measures the heat content of a chemical system. The change in enthalpy equals the heat released by a reaction. As the temperature rises to the dissociation temperature, the number of molecular interactions increases. When these interactions increase, the internal energy of the molecules also increases. This results in a decrease in temperature because the endothermic nature of the collisions causes the molecules to absorb heat.

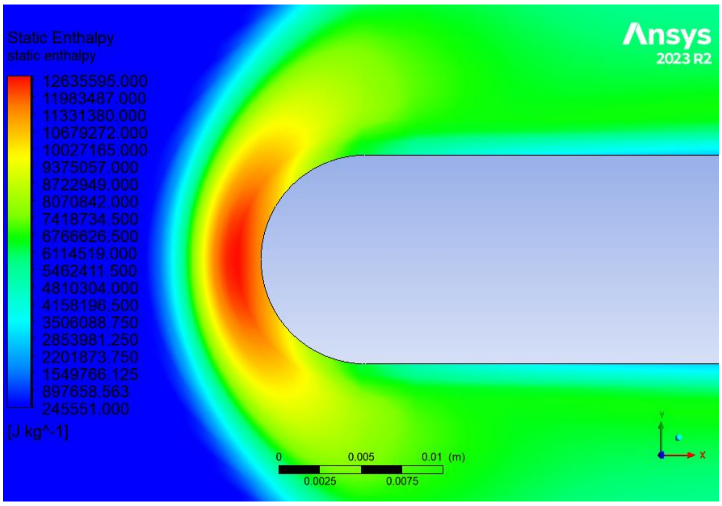

Fig. A)

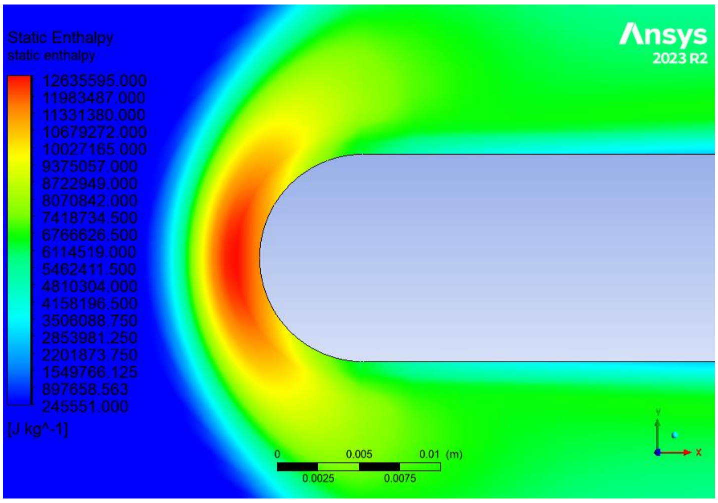

Fig. B)

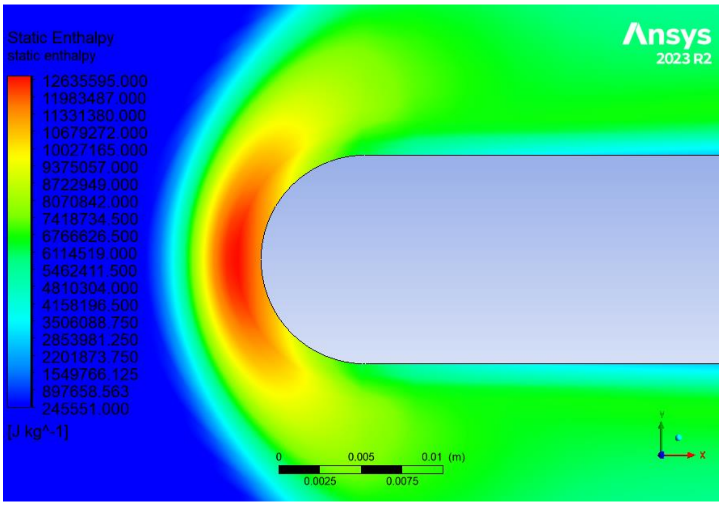

Fig. C)

M=15.65, $H = 60.96\ Km$,

$T = 244.4\ k$, $\rho = 2.745\ 10{-}4\ kg$
$m3$ $P = 19.26\ Pa$, $\alpha = 0°$

$Fig.\ A)$ Perfect gas Fig

$Fig.\ B)$ 5 $Reactions$

$Fig.\ C)$ 17 $Reaction$

Figure 4.23 : Temperature field along surface streamline.

4.3.3 Angle of attack effect :

A steep re-entry causes a low surface heating rate because the vehicle passes quickly through the denser parts of the atmosphere. This short duration of exposure minimizes the overall heating on the vehicle's surface. Additionally, the aerodynamic forces, such as drag and lift, are reduced due to the brief interaction with the dense atmospheric layers.

On the other hand, shallow re-entries lead to higher surface heating rates. In this case, the vehicle travels through the denser parts of the atmosphere more slowly, resulting in prolonged exposure to aerodynamic heating. This increased duration causes higher surface temperatures. Furthermore, the aerodynamic forces increase because the vehicle remains in the denser atmosphere for a longer period, leading to higher drag and lift.

This increase in AOA also corresponds to a rise in wall temperature by 500K, as shown in Fig.(4.24)

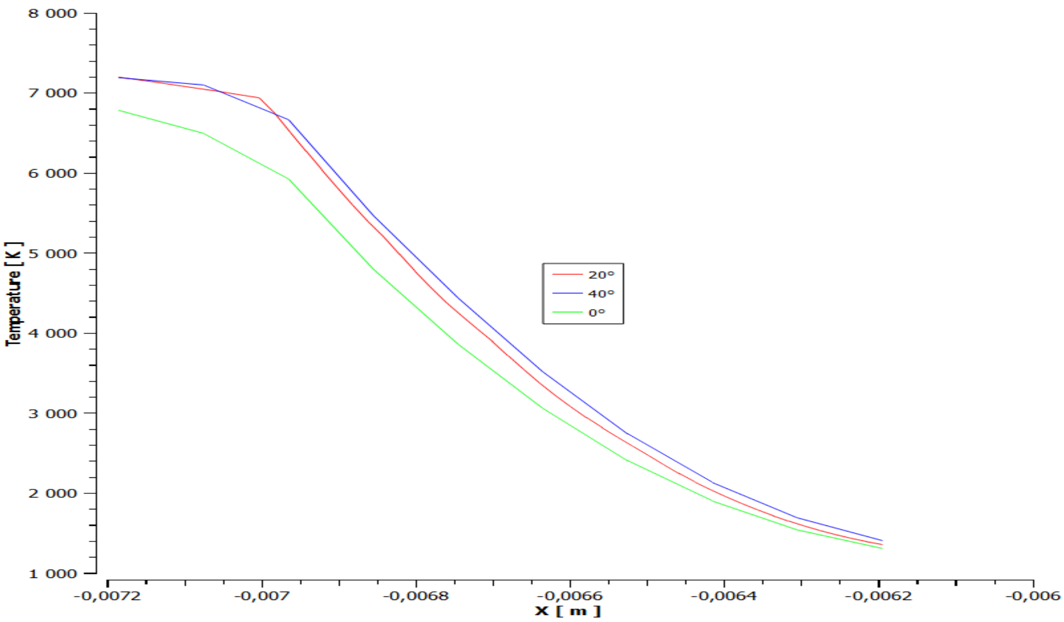

Figure 4.24: Wall temperature distribution along surface streamlines for deferent angle of attack

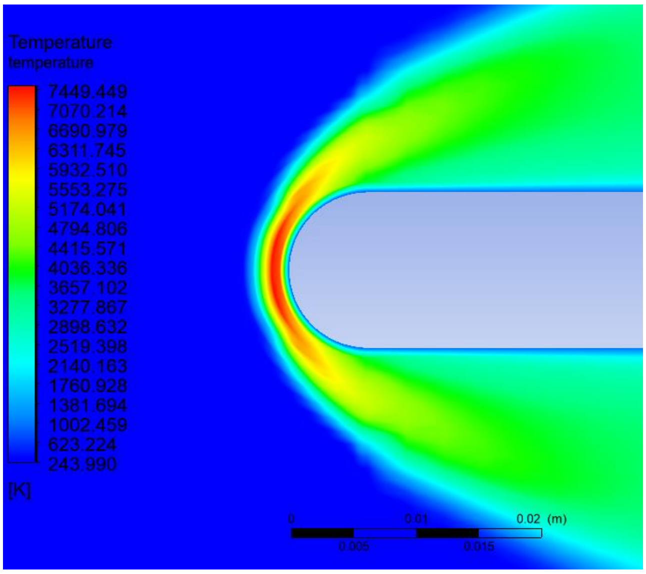

Fig (A) $\boldsymbol{\alpha} = \mathbf{0}°$

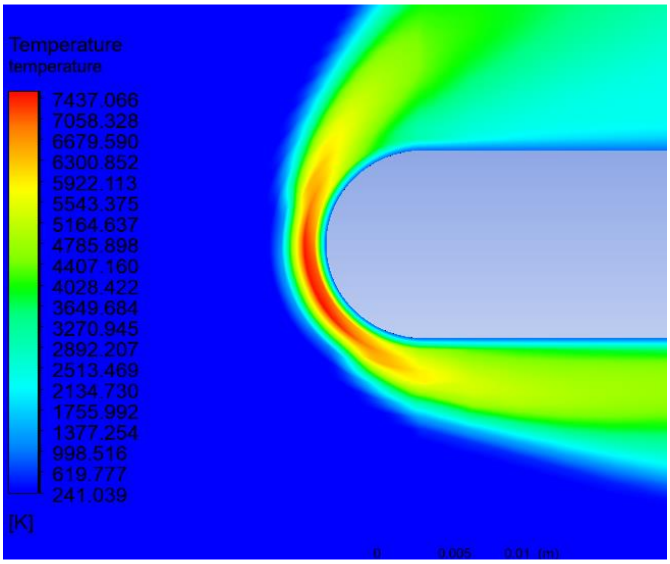

Fig (B) $\boldsymbol{\alpha} = \mathbf{20}°$

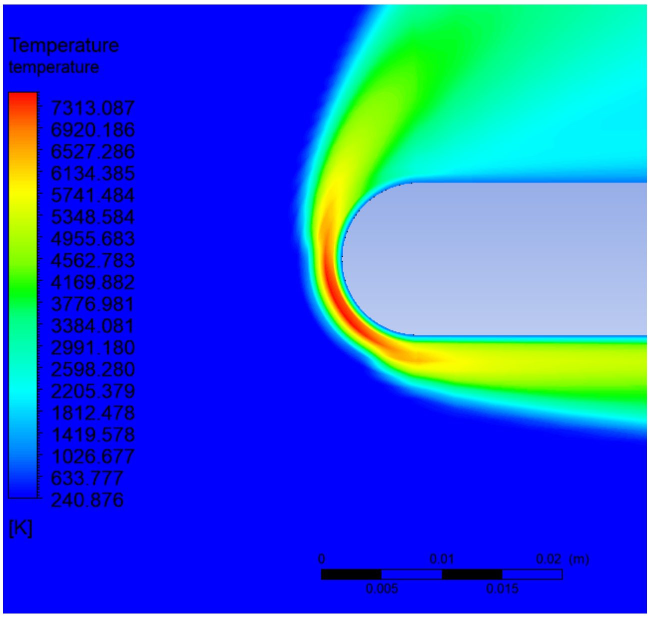

Fig (C) $\boldsymbol{\alpha} = \mathbf{30}°$

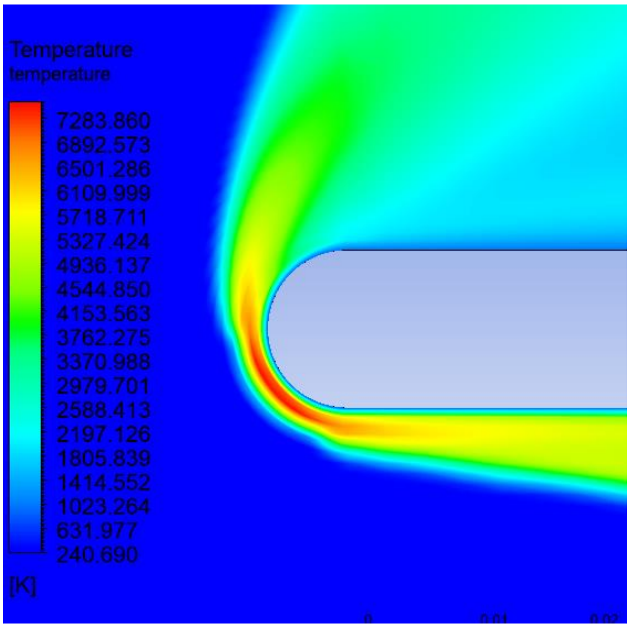

Fig (D) $\boldsymbol{\alpha} = \mathbf{40}°$

M=15.65, $H = 60.96\ Km$, $T = 244.4\ k$, $\rho = 2.745\ 10{-}4\ kg\ m3 / P = 19.26\ P$

figure 4.25: Temperature field along surface stream line at deferent angles of attack

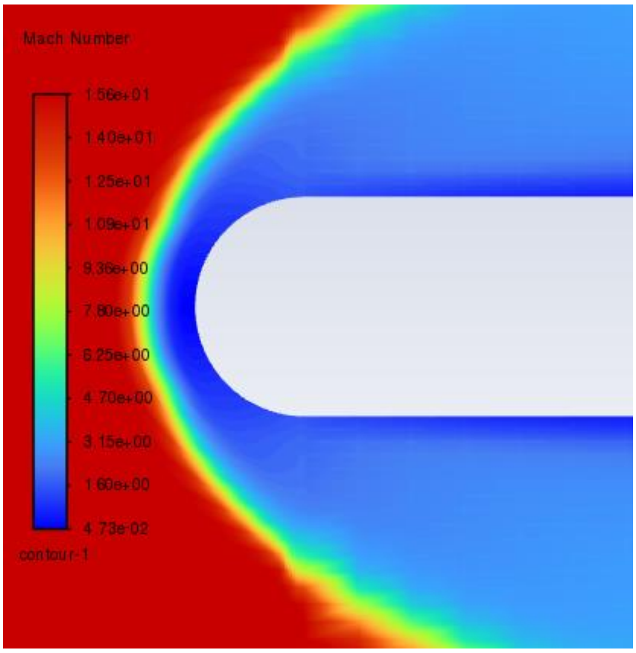

Fig (A) $\boldsymbol{\alpha} = \mathbf{0}°$

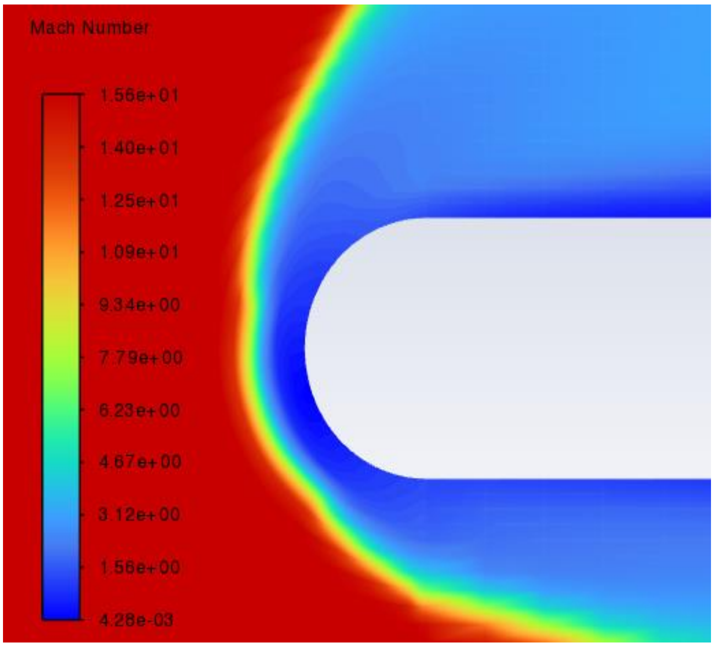

Fig (B) $\boldsymbol{\alpha} = 2\mathbf{0}°$

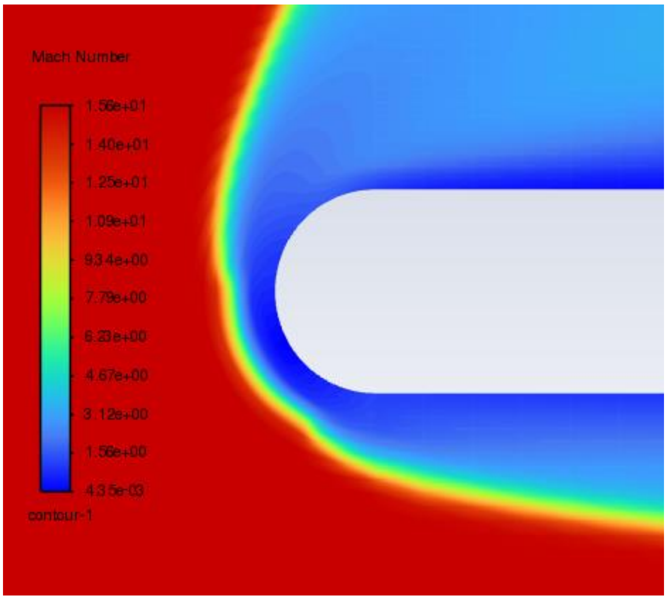

Fig (C) $\boldsymbol{\alpha} = \mathbf{30}°$

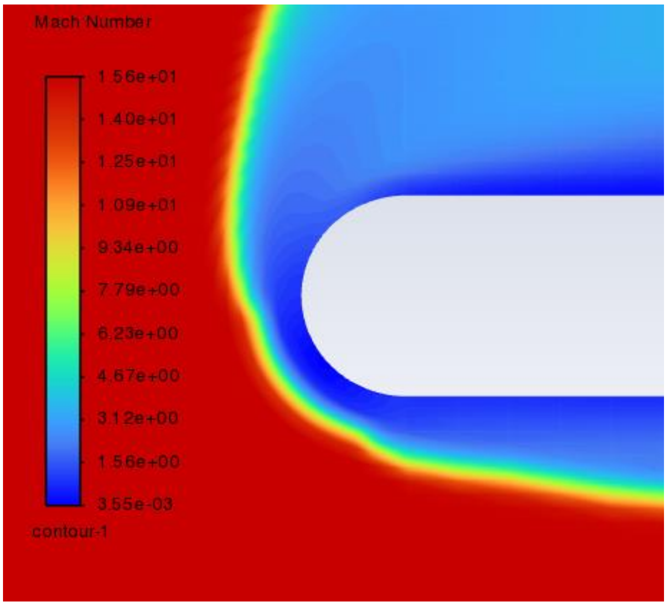

Fig (D) $\boldsymbol{\alpha} = \mathbf{40}°$

$\boxed{\text{M=15.65, } H = 60.96\ Km,\ T = 244.4\ k\ ,\ \rho = 2.745\ 10{-}4\ kg\ m3 / P = 19.26\ P}$

Figure 4.26: Mach number field along surface stream line at deferent angles of attack

4.3.4 Radiation effect on tempeature evolution :

In a hypersonic thermochemical non-equilibrium flow, various chemical reactions occur, many of which are endothermic. These reactions absorb heat from the surrounding gas to break molecular bonds, thereby reducing the temperature of the flow and the vehicle's surface.

As we can see The radiation effect can enhance these endothermic reactions by providing additional pathways for energy dissipation. Additionally, the shock layer formed in front of the vehicle can radiate energy away. High-energy particles within this layer emit radiation as they relax to lower energy states.

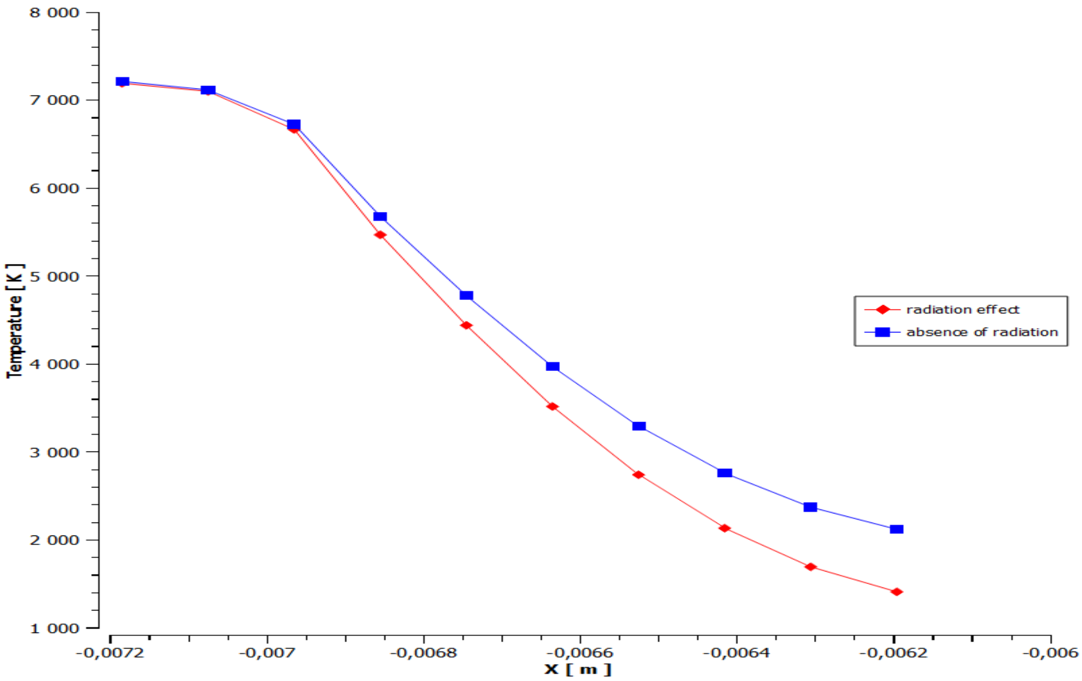

Figure 4.27 ; Temperature field evolution variation in the presence and absence of radiation effect for M = 15.56

This radiation removes energy from the shock layer, contributing to a decrease in temperature both in the shock layer and at the vehicle's surface as shown in (figure 4 .27) and (figure 4.28) there has been a decrease in temperature by approximatly 180k in the presence of radiation effect.

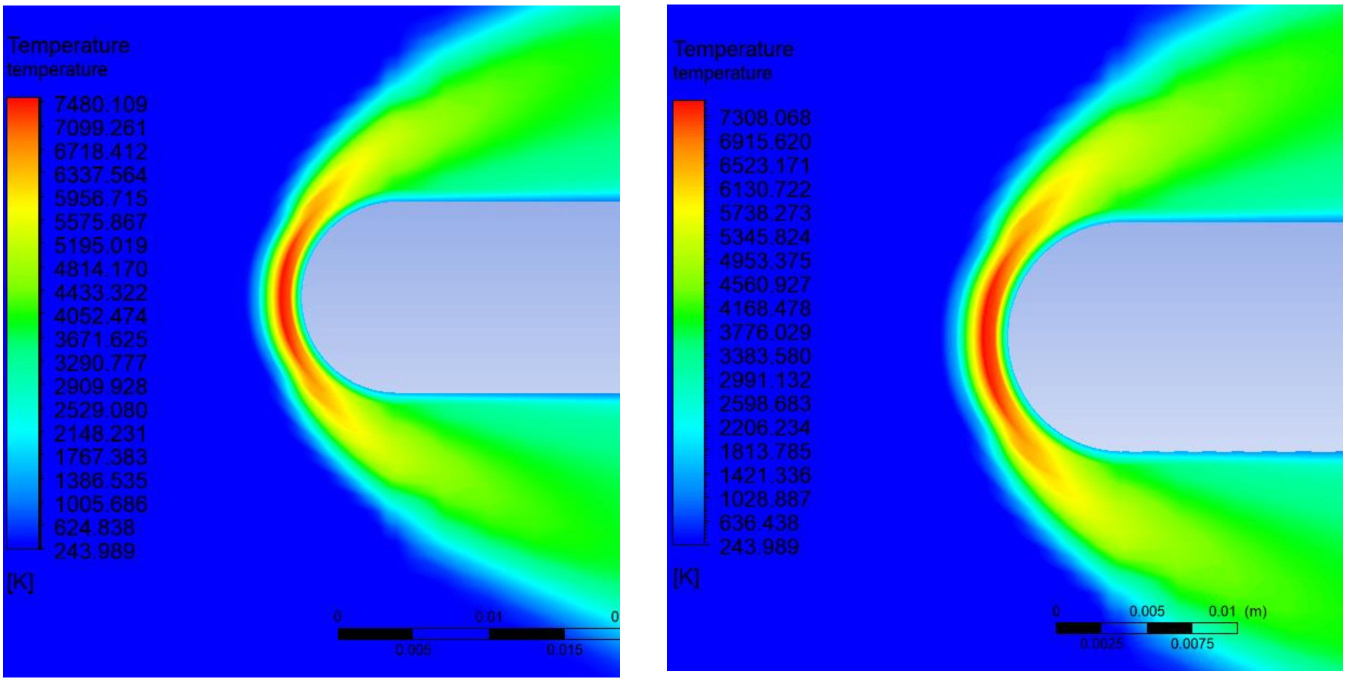

fig A) **Fig B)**

fig A) :Radiation effect Neglected	fig B) : With radiation effect
M=15.65, $H = 60.96\ Km$, $T = 244.4\ k$, $\rho = 2.745\ 10{-}4\ kg\ m3 / P = 19.26\ P$	

Figure 4.28 : Temperature field evolution variation in the presence and absence of radiation effect for M = 15.56

Highlights about The Effect of Radiation on Temperature in the Shock Layer for Hypersonic Flow

The effect of radiation in a hypersonic flow can either increase or decrease the temperature in the shock layer, depending on various factors such as gas composition, temperature and pressure conditions, and the optical properties of the medium. Here are the two main scenarios:

Increase in Temperature

- **Radiative Emission**: In many cases, thermal radiation emitted by particles and molecules in the shock layer can contribute to an increase in the local temperature. This radiation carries thermal energy that can be absorbed by the surrounding molecules, thus increasing their thermal energy.

Decrease in Temperature

- **Radiative Absorption**: If the surrounding medium or the vehicle itself absorbs a significant portion of the emitted radiation, this can lead to a relative cooling of the shock layer. The radiation carries thermal energy away from the shock layer, which can reduce the local temperature.

Complex Interactions

- **Radiative Balance**: The balance between radiative emission and absorption can be complex. Sometimes, radiation can initially increase the temperature, but upon reaching a certain threshold, phenomena such as molecular dissociation may start to absorb this energy, thus moderating the temperature increase.

Determining Factors

- **Initial Conditions**: The initial temperature and pressure of the incoming airflow play a crucial role in the impact of radiation.
- **Optical Properties**: The gas's ability to emit and absorb radiation depends on its optical properties, such as opacity and absorption coefficient.

Conclusion

In general, in hypersonic flows, the dominant effect tends to be an increase in temperature in the shock layer due to radiative emission. However, scenarios where radiation may have a cooling effect are not excluded, and the net effects depend on the specific flow conditions and gas properties. In our cas, and in figure 4.17, we observe that the temperature in the relaxation zone decrease with about 35k, that is to say, a decrease of approximately 0.3%, On the other hand, as seen in Figures 4.27 and 4.28, the phenomenon of radiation absorbs heat, leading to a reduction in temperature within the shock layer. This effect occurs because the energy from the shock wave is partially converted into radiation, which is then emitted away from the shock layer. Consequently, the temperature within the shock layer decreases, demonstrating the significant influence of radiative heat transfer on the thermal characteristics of hypersonic flows.

Conclusion

Conclusion

In this thesis, we have thoroughly examined the influence of chemical kinetic models on hypersonic thermochemical non-equilibrium and radiative flow around lifting bodies during atmospheric re-entry. Our analysis covers the impact of various chemical reaction models on important parameters such as wall temperature, heat flux, and aerodynamic forces experienced by re-entry vehicles.

By using advanced simulation techniques and detailed modeling of physico-chemical phenomena encountered during atmospheric reentry, such as molecular vibration, dissociation, and heat transfer, we can account for the behavior of air at high temperatures. The air is assumed to be in the shock layer of a reactive gas composed of five species (N2, O2, O, N, NO), which react with each other according to the Zeldovich Model with 5, 17 elementary reactions, creating an intense shock wave.

Using ANSYS 23, we were able to simulate and analyze the complex interactions between the gas particles and the surface of the re-entry vehicle. This allowed us to capture the effects of high temperatures, chemical reactions, and energy exchanges in the post-shock region. This detailed analysis helps us understand how these phenomena impact the vehicle's thermal protection system and overall performance during re-entry.

One significant finding is that increasing the number of chemical reactions has a positive effect on cooling the spacecraft's wall. For instance, when comparing a model with 17 chemical reactions to one with only 5, there is a noticeable temperature reduction of 1407K. This temperature decrease occurs because, during re-entry, molecules absorb energy to recombine or break their chemical bonds. These processes are endothermic, meaning they consume heat, which ultimately leads to a decrease in the wall temperature.

At high Mach numbers, endothermic phenomena become significant due to the intense kinetic energy and collisions of gas molecules. These reactions absorb energy, reducing the overall gas temperature. This cooling effect on the spacecraft's surface helps manage extreme heat during high-speed re-entry, as energy is used to break molecular bonds instead of heating the vehicle.4o

The shock wave's position is precisely localized near the obstacle, around 0.50 mm for the Lobb sphere, matching experimental findings. Using ANSYS 23 software, our simulations accurately replicated the flow dynamics in the relaxation zone. This allowed us to determine essential parameters, including Mach number, pressure, temperature distribution, and changes in mass fractions. The results validate the effectiveness of our simulation approach in capturing key aspects of hypersonic flow.

For blunt body vehicles, the intense heating from the strong bow shock wave is significantly reduced by radiative cooling. The large surface area and high-energy interactions of blunt bodies facilitate the emission of thermal energy as electromagnetic waves, lowering the surface temperature and enhancing thermal protection. Similarly, for delta profile vehicles, radiation aids in temperature management by dissipating heat generated by aerodynamic heating. Although the flow dynamics differ due to their sleek, aerodynamic shape, radiative cooling remains effective. This emission helps balance thermal loads, ensuring the vehicle maintains structural integrity and performance during re-entry.

Steep re-entries result in lower surface heating, while shallow re-entries lead to higher heating rates and increased aerodynamic forces. From our results (Fig. 4.24), it is noted that as the angle of attack (AOA) increases from 0° to 40°, the wall temperature rises by approximately 500K (Fig. 4.23). This temperature increase allows our delta-shaped vehicle to maneuver more effectively, directing aerodynamic forces to the intended landing area.

Finally, in hypersonic flows, radiative emission primarily increases the temperature in the shock layer, but under certain conditions, it can induce cooling. In our study (Figure 4.17), the relaxation zone temperature decreases by approximately 35K, about 0.3%. Figures 4.27 and 4.28 illustrate how radiation absorbs heat, lowering temperatures in the shock layer by converting shock wave energy into emitted radiation. This underscores the profound impact of radiative heat transfer on hypersonic flow dynamics, emphasizing its critical role in thermal management.

Outlooks

Here are three focused outlooks based on this study of hypersonic flows and re-entry dynamics:

1. Refinement of Chemical Kinetic Models: Future research should prioritize developing more sophisticated chemical kinetic models. This includes exploring complex reactions and species interactions to better predict heat flux, temperature distributions, and changes in gas composition during hypersonic re-entry.

2. Advancements in Thermal Protection Systems: There is a need to innovate thermal protection systems that optimize radiative cooling effects. Research could concentrate on developing new materials and configurations to enhance heat dissipation, thereby improving vehicle durability and performance during re-entry.

3. Integration of Computational Approaches: Integrating advanced computational fluid dynamics (CFD) with detailed chemical kinetics and radiative heat transfer models offers a holistic approach. This approach aims to better simulate the intricate interactions between gas dynamics, chemical reactions, and thermal management strategies in hypersonic flows, leading to more robust design guidelines for future aerospace applications.

References

[1] Convective and Radiative Heating for Vehicle Return from the Moon and Mars Robert B. Greendyke ViGYAN, Inc. Hampton, VA 23666 and Peter A. Gno o NASA Langley Research Center Hampton, VA 23681-0001

[2] Gno o, Peter A.; Weilmuenster, K. James; Braun, Robert D.; and Cruz, Christopher T.: \E ects of Sonic Line Transition on Aerothermodynamics of the Mars Pathnder Probe," AIAA Paper 95-1825, June 1995. 7

[3] Stewart, D. A.; Rakich, J. V.; and Lanfranco, M. J.: \Catalytic Surface E ects Experiment on Space Shuttle," AIAA Paper 81-1143, June 1981

[5] I.J. Keshtiban, F. Belblidia and M.F. Webster," COMPRESSIBLE FLOW SOLVERS FOR LOW MACHNUMBER FLOWS", Institute of Non-Newtonian Fluid Mechanics,University of Wales, Swansea SA2 8PP, UK,2004

[6] Sudharsan Thiruvenkadam, "A Computational model to characterize different flow regimes microscale re-entry satellites ",1st edition ,Master of science engineering, The University of Texas at Arlington in Partial Fulfilment, Arlington, December 2013

[7] J.J.Bertin, " Hypersonic Aerothermodynamics", AIAA Education Series, ISBN 1-56347 036-5, 1938.

[8] Anderson, "Normal Shock waves , Compressible Fluid Flow", Second Edition Chapter 3 pp. 88-125, Blacksburg, Virginia, 2019.

[9] "Stardust – Cool Facts"*stardust.jpl.nasa.gov*. Archived from the original on January 12, 2010. Retrieved January 9, 2010

[10] Sanjeev Kumar, M.Tech." Numerical Simulation of Chemically Reactive Hypersonic Flows", 1st edition A95-95357, European Computational Fluid Dynamics, Germany22. Dezember 2005.

[11] Ideen Sadrehaghighi, Ph.D. "Turbulence Modeling",1 edition PhD in Mechanical Engineering , CFD Open Series , Mason, Ohio, États-Unis 2006

[12] Ismail B. Celik ," Introductory Turbulence Modeling", 1 edition , P.O. Box 6106, University Mechanical & Aerospace Engineering Dept. West Virginia December 1999.

[13] Goodarz Ahmadi , "Introduction to turbulence modelling," , 13699-5725 Department of Mechanical and Aeronautical Engineering, Clarkson University Potsdam, 1994.

[14] Gerald Recktenwald,An ," Introduction to Turbulence Modeling ", edition 4 ,for CFD, Mechanical and Materials Engineering Department Portland State University, Portland, Oregon, February 19, 2020.

[15] L. Cutrone , F. Battista , "Assessment of Wall-functions k−ε Turbulence Models for the Prediction of the Wall Heat Flux in Rocket Combustion Chambers ",80125 Dipartimento di Ingegneria Aerospaziale, DIAS Universita degli Studi di Napoli "Federico II", Piazzale Tecchio, Naples, Italy January- 2018.

[16] Ahmed Al Makky, ”Coding Tutorials for Computational Fluid Dynamics”, First edition, University of the West of Scotland ,United Kingdom 2014

[17] R. ALLOUCHE «SIMULATION NUMERIQUE DES EFFETS DE LA RADIATION SUR LES PARAMETRES THERMOCHIMIQUES DERRIERE UNE ONDE DE CHOC» thèse de Doctorat, département Mécanique , Université Mentouri, Alger 2014, Université Houari Boumedien.

[18] Robert B. Greendyke, ViGYAN, Inc. Hampton, VA 23666 and Peter A. Gnoffo «Convective and Radiative Heating for Vehicle Return from the Moon and Mars» NASA Langley Research Center Hampton, VA 23681-0001

[19] Perrel, F. Simulation numérique d'écoulements hypersoniques visqueux en déséquilibre chimique. Thèse de l'Ecole Nationale Supérieure de l'Aéronautique et de l'Espace, N° 77, octobre 1991, Toulouse, France.

[20] G. Candler . «The Computation of Weakly Ionized hypersonic Flow in thermo-chemical Nonequilibrium » a Dissertation , Stanford university,June 1988

[21] Mesh-Intro 16.0 L07 Mesh Quality and Advanced Topic

[22] JOHAN STROHMEIER. "Etude numérique et analytique des propriétes des torchére d’hydrogéne dans un milieu venteux ", Novembre 2011.

[23] A BOULAHIA,”Couche Limite hypersonique dans des écoulements visqueux en déséquilibre chimique” 1er edition,thèse de Doctorat, département physique, Université Mentouri, Constantine 2010.

[24] Franke ,J,Hellsten,A,Schlunzen ans Carissimo,B,”best practice guide for the For the CFD simulation of fows in the urban environment” ,cost Action732:quality assurance and improvement of microscale meteorological models, Belgium 2007.

[25]Tominaga,Y,Mochida,A,Yoshie,R,Kataoke,H,Nozu,T,Yoshikawa,M,and Shirasawa ,T,”ALJGUIDELINES for pratical application of CFD to pedestrian wind envirement around buildings” , 96, Tohoku University, Aoba 06, Aramaki, Aoba-ku, Sendai-City, Miyagi, Urban on Conference International seventh ,yokohama japan, 2009 July 3 - June

[26] "ANSYS Help14.5"ANSYS Computing Platform Support Summary , Irvine October 2012.

[27] ANSYS 13.0 Tutorial, "Customer Training Material".: ANSYS ,Irvine 12/2010

[28] Patrick M.Knupp, ”Remarks on Mesh Quality” , NM87185 ,Aerospace Sciences Meeting and Exhibit,7- Sandia National Laboratories,Sandia 10January, 2007.

[29]] Tristan Soubrie, "Prise en compte de l’ionisation et du rayonnement dans la modélisation des écoulements de rentrée terrestre et martienne", PhD de l’université de Provence, 2006.

[30] Jun Hyeok Chae, , Tapan K. Mankodi, , Seong Man Choi ,, Rho Shin Myong ,”Combined Effects of Thermal Non-equilibrium and Chemical Reactions on HyperAeronautical and Space Sciences, Korean S ,2020.

[31] John A. ordi, Robert J. idal, and Charles B. Johnson “ Chemical Nonequilibrium effects on the inviscid flow in the windward plane of symmetry of two simplified shuttle configurations”, first edition , Cornell Aeronautical Lab., Inc. Hampton, VA, United States, NASA Langley Research Center ,Washington 1973.

[32] 47] ANSYS 13.0 Tutorial, "Customer Training Material".: ANSYS ,Irvine 12/2010

[33]Jun Hyeok Chae, , Tapan K. Mankodi, , Seong Man Choi ,, Rho Shin Myong ,”Combined Effects of Thermal Non-equilibrium and Chemical Reactions on Hypersonic Air Flows Around An Orbital Re-entry Vehicle”, edition 4,International Journal of Aeroautical and Space Sciences, Korean S ,2020.

[34] Ascher_H._Shapiro, The Dynamics and Thermodynamic.

[35] Loïc van Ghèle. “ Analyse aérothermodynamique de la rentrée atmosphérique d’un véhicule réutilisable depuis une orbite basse terrestre”. Sciences de l’ingénieur [physics]. Université de Toulouse, Français, 2020

[36] Gerald Recktenwald,An ,” Introduction to Turbulence Modeling “, edition 4 ,for CFD, Mechanical and Materials Engineering Department Portland State University, Portland, Oregon, February 19, 2020